The Dissertation Committee for Steven Andrew Mattis
certifies that this is the approved version of the following dissertation:

Mathematical Modeling of Flow Through Vegetated Regions

Committee:

Clint Dawson, Supervisor

Irene Gamba

Matthew Balhoff

Omar Ghattas

Leszek Demkowicz

Mathematical Modeling of Flow Through Vegetated Regions

by

Steven Andrew Mattis, B.S., M.S.C.A.M.

DISSERTATION

Presented to the Faculty of the Graduate School of

The University of Texas at Austin

in Partial Fulfillment

of the Requirements

for the Degree of

DOCTOR OF PHILOSOPHY

THE UNIVERSITY OF TEXAS AT AUSTIN

August 2013

Dedicated to my mother and father.

Acknowledgments

This work would not have been possible without the support and insight of my Ph.D. supervisor Dr. Clint Dawson. I began graduate school with a mostly pure mathematics background, and he helped shape me into a well-rounded scientist in the areas of applied mathematics, hydraulics, and computational science. I appreciate the amount of freedom that he gave me in pursuing the research that interested me the most, while always reminding me of practical concerns and broader impact. I look forward to more collaboration in the future.

I want to thank my collaborators Dr. Christopher Kees and Dr. Matthew Farthing from the U.S. Army Corps of Engineers Research and Development Center for the boundless support that they have given me through the years. Without the use of Proteus, their computational toolkit, implementing my numerical methods would have been incredibly challenging and far more time consuming. They also provided invaluable insight into mathematical models and numerical methods. They introduced me to a great number of useful tools for software development that will likely be useful for my entire career.

I have been incredibly lucky with regards to financial support while working on my Ph.D. Most of my funding has been provided by two fellowships that have given me immense freedom regarding research. One is the Na-

tional Defense Science and Engineering Graduate (NDSEG) Fellowship from the Department of Defense. The second is the CAM Fellowship from ICES. I am eternally indebted to these fellowship programs. They have provided me with opportunities for which most graduate students can only wish.

Other financial support for the work presented in this dissertation have come from USACE Contract W912HZ-08-C-0050, National Science Foundation grant DMS-0915223, and Army Research Office project 63598-MA. It is essential to acknowledge the NSF Teragrid and the Texas Advanced Computing Center (TACC) at The University of Texas at Austin for providing HPC resources that have contributed to the research results reported within this dissertation.

I would like to thank the faculty and staff of ICES for teaching me so much over the last several years. The model for interdisciplinary research at ICES is one that should be copied by every institution that wants to enter the field. I especially want to thank my dissertation committee for the time and support that they have given me. I also want to thank the fellow graduate students who have now become my colleagues and friends. I have gotten many great ideas from you. I want to thank the Computational Hydraulics Group. I cannot think of a better group of people with whom to work.

Lastly, I want to acknowledge my family for always being there for me. I remember when I was a child when people asked me what I was going to be when I grew up, I would usually say I wanted to be a scientist or an engineer. I suppose I am now both of those things. My family has always supported me

in these endeavors.

Mathematical Modeling of Flow Through Vegetated Regions

Steven Andrew Mattis, Ph.D.
The University of Texas at Austin, 2013

Supervisor: Clint Dawson

Understanding flow processes of sea and fresh water through complex coastal regions is of utmost importance for a number of applications of interest to the scientific and engineering community, including wetland health and restoration, inland flooding due to tropical storms and hurricanes, and navigation through coastal waters. In such regions, the existence of vegetation increases flow resistance, which is a major factor in determining velocity and water level distribution in wetlands and inland. Commonly, the momentum loss due to vegetation is included in a bottom friction term in the model equations; however, such models may oversimplify the complex resistance characteristics of such a system. With recent increases in computational capabilities, it is now feasible to develop and implement more intricate resistance models that more accurately capture these characteristics.

We present two methods for modeling flow through vegetated regions. With the first method, we employ mathematical and computational upscaling

techniques from the study of subsurface flow to parametrize drag in a complex heterogeneous region. These parameterizations vary greatly depending on Reynolds number. For the coastal flows in which we are interested the Reynolds number at different locations in the domain may vary from $\mathcal{O}(1)$ to $\mathcal{O}(1000)$, so we must consider laminar and fully turbulent flows. Large eddy simulation (LES) is used to model the effects of turbulence. The geometry of a periodic cell of vegetative obstacles is completely resolved in the fluid mesh with a standard no-slip boundary condition imposed on the fluid-vegetation boundaries. The corresponding drag coefficient is calculated and upscaling laws from the study of inertial flow through porous media are used to parametrize the drag coefficient over a large range of Reynolds numbers. Simulations are performed using a locally conservative, stabilized continuous Galerkin finite element method on highly-resolved, unstructured 2D and 3D meshes.

The second method we present is an immersed structure approach. In this method, separate meshes are used for the fluid domain and vegetative obstacles. Taking techniques from immersed boundary finite element methods, the effects of the fluid on the vegetative structures and vice versa are calculated using integral transforms. This method allows us to model flow over much larger scales and containing much more complicated obstacle geometry. Using a simple elastic structure model we can incorporate bending and moving obstacles which would be extremely computationally expensive for the first method. We model flexible vegetation as thin, elastic, inexten-

sible cantilever beams. We present two numerical methods for modeling the beam motion and analyze their computational expense, stability, and accuracy. Using the immersed structure approach, a fully coupled steady-state fluid-vegetation interaction model is developed as well as a dynamic interaction model assuming dynamic fluid flow and quasi-static beam bending. This method is verified using channel flow and wave tank test problems. We calculate the bulk drag coefficient in these flow scenarios and analyze their trends with changing model parameters including stem population density and flow Reynolds number. These results are compared to well-respected experimental results. We model real-life beds of *Spartina alterniflora* grass with representative beds of flexible beams and perform similar comparisons.

Table of Contents

List of Tables

List of Figures

Chapter 1

Introduction

1.1 Purpose of Study

Understanding flow processes of sea and fresh water through complex coastal regions is important for a number of applications of interest to the scientific and engineering community; e.g., wetland protection and restoration projects, navigation through coastal waters, and projects aimed at reducing the effects of storm surge on low-lying coastal areas. Coastal flow processes and navigation are complicated by the presence of smaller-scale features, including stationary and moving man-made structures, vegetated marshlands, barrier islands, etc., and the interaction of these features with the larger flow domain which may include the continental shelf and ocean basins.

In the applications mentioned above, particularly coastal inundation due to storm surge, the ability of these smaller-scale features to provide resistance to flow is of utmost concern. Current mathematical models and parametrizations of flow resistance characteristics due to flow over and around porous structures or through heavily vegetated regions are inadequate to accurately capture these physical processes, and as a result, numerical models based on these mathematical representations may be inaccurate. Furthermore,

while the use of highly resolved, three-dimensional Navier-Stokes models may avoid some of the parametrization issues, the implementation of such models over large coastal regions is prohibitive, and in many cases, unnecessary to adequately describe the flow physics. An alternative is to appropriately couple mathematical/numerical models that accurately and efficiently capture the primary flow characteristics of a given region within the larger flow domain.

In this thesis we focus on the flow of water through a vegetated region. The existence of vegetation affects the flow resistance, which is a major factor in determining velocity and pressure distribution. The main impact of vegetation on flow is form drag, which results in momentum losses as discussed by Batist et al. [4]. Since modeling the effects on flow from each individual plant is impractical in a large-scale simulation, where computational resolution is on the order of tens of meters, we focus on methods for describing and capturing this sub-grid scale phenomena through the computation of drag coefficients which may be used in a macro-scale model.

1.2 Background

A great deal of experimental and computational effort has been focused on characterizing drag effects of flow through vegetated regions. Much experimental work has focused on calculating Manning's n for flow over different types of plants. The Manning formula is a highly-simplified empirical model for fully turbulent open channel and free-surface flow. Manning's n incorporates bottom friction, bottom shape, vegetative drag, and other resistance

characteristics into one value. According to experimental work done by Ree and Palmer [87] and Petryk and Bosmajian [79], it varies greatly depending on properties of vegetation and is highly dependent on water depth; although, this factor is commonly ignored. Thus many, including Kandlec [43] and Turner and Chanmeesri [105] have demonstrated that Manning's equation is inadequate for describing shallow water flow through vegetation over a large range of velocities and for a variety of water depths. They suggest that the appropriate drag models would best be site-specific functions of water depth and plant shape, distribution, and flexibility.

In this report, we use methods from the study of subsurface flow in porous media and high-resolution modeling of flow through vegetated regions to calculate upscaled drag coefficients, which vary greatly with Reynolds number and water depth, that may be used in large-scale resistance modeling of flow through vegetated areas. Upscaling is the process of analyzing micro-scale dynamics to describe larger scale phenomena. Vegetated domains have similar geometry to subsurface porous media domains. We use simple domains of arrays of cones and cylinders to model vegetation structures. Especially at lower Reynolds numbers, much experimental and theoretical research has been performed for upscaling subsurface flows. Specifically, there are several mathematical homogenization methods for upscaling viscous flow in porous media. Homogenization is the method of mathematically deriving effective equations to describe dynamics at larger scales by satisfying to some degree the dynamics at the smaller scales. For higher Reynolds numbers, inertial effects and

turbulence are important factors in flow characteristics. Reynolds Averaged Navier-Stokes (RANS) models and modern high-resolution techniques such as large eddy simulation (LES) and direct numerical simulation (DNS) are useful in resolving these factors.

The most basic model of flow through porous media is Darcy's law, determined experimentally by Henry Darcy in 1856. Darcy's law is only valid for slow, viscous flow, which is sufficient for most subsurface modeling scenarios. Darcy's law contains a hydraulic conductivity tensor, which measures the ability of the media to permit flow, which must be known before the law can be used for predictive simulations. There are both experimental and theoretical approaches to calculating the hydraulic conductivity of a porous medium. One method is to measure velocity and hydraulic gradient directly and use Darcy's law to calculate the hydraulic conductivity. It is also common for hydraulic conductivity to be estimated using empirically derived formulas. Descriptions and analyses of these methods are done by Bear [5]. Darcy's law is theoretically derived by mathematical homogenization of Stokes flow. The process of homogenization explained by Hornung [37] describes a theoretical method of determining hydraulic conductivities. A more recent in-depth mathematical treatment of homogenization theory has been done by Mikelić [70].

For flow through vegetated domains we generally cannot assume slow, viscous flow, so Darcy's law is an inadequate model. For higher velocity flows where inertial forces matter, there exist "non-Darcy" models which include higher order terms. These laws suggest a nonlinear relationship between fluid

velocity and hydraulic gradient at higher Reynolds numbers. Forchheimer [26] was likely the first to propose a non-Darcy relationship. The Darcy-Forchheimer Equation is Darcy's law with an additional quadratic velocity term. The Darcy-Forchheimer Equation has been observed experimentally for moderate Reynolds numbers by many researchers. There have been many attempts at deriving the non-Darcy laws using mathematical homogenization; however, these studies such as those by Lions [58], Sanchez-Palencia [91], Mei and Auriault [67], Balhoff et al. [2], and Rasoloarijaona and Auriault [83] show the quadratic terms canceling, giving a cubic law. This cubic law has been verified numerically for very small Reynolds numbers by solving the Navier-Stokes equations by Colaud et al.[14], Rojas and Koplik [89], Balhoff et al. [2], and Koch and Ladd [50]. However, this has only been verified where Darcy's law is approximately valid, and the quadratic law seems to be more appropriate for higher Reynolds number flows. Some methods provide a result with quadratic and cubic terms. Some, including Scheidegger [93] have also used power laws to fit empirical data. Garibotti and Peszyńska [30] provides computational analysis of non-Darcy flow through porous media using a finite difference method. There are also "computational upscaling" techniques. These homogenization methods are not based on mathematical derivation, but are performed by analyzing results from solving the full Navier-Stokes equations on fine grids as seen in work by Peszyńska et al. [78], Balhoff et al. [2], and Balhoff and Wheeler [3].

Higher Reynolds number flow characteristics through vegetated do-

mains has been studied a great deal with regard to atmospheric flow through plant canopies and flow through vegetated open channels. Dawson and Charlton [19] give an extensive bibliography of earlier work in this field, and Nepf et al. [73] [57] [75] provide excellent in-depth experimental analysis of drag, turbulence, and diffusion for flow through arrays of cylinders and dense beds of grasses at high Reynolds numbers. Much of the numerical modeling effort has focused on developing turbulence closure schemes to the governing equations. There are two main approaches to providing turbulence closure. One method uses the Reynolds Averaged Navier-Stokes (RANS) equations which requires a model for Reynolds stresses to provide turbulence closure. The other method uses Large Eddy Simulation (LES) turbulence models to solve the filtered Navier-Stokes equations.

RANS methods have been used with varying degrees of success. Christensen [13] found that simple mixing length closure methods can be successful models for flow through simple domains. However, Wilson and Shaw [111] acknowledge that first order RANS closure schemes, while simple, do not provide results that adequately match empirical data through more complex domains. They propose a higher order closure scheme for a spatially as well as temporally averaged version of the governing equations, resulting in a one-dimensional representation of the problem. Raupach and Shaw [86] extend this work, proposing a method of obtaining momentum and energy equations in multi-connected flows. These equations capture different momentum and dissipation terms resulting from the three-dimensional nature of this flow.

Raupach et al. [85] validate this model experimentally, using aluminum strips to model vegetation.

The most commonly used and most useful RANS closure schemes are two equation methods. These schemes involve solving two transport equations for turbulent kinetic energy and dissipation whose solutions define an eddy viscosity. These equations contain empirically calculated constants. Burke and Stolzenbach [11] introduce drag-related source terms to model the effect of vegetation. The most commonly used two equation closure models are the $k-\epsilon$ and $k-\omega$ models. López and Garcia [60], [61] give a full analysis of these schemes and show their ability to predict 3D flow patterns. Defina and Bixio [21] shows that a $k-\epsilon$ model may accurately predict flow patterns and eddy viscosities, but may poorly predict more complex turbulence characteristics.

As an alternative to RANS models, LES can be used to solve the filtered Navier-Stokes equations and can provide an almost complete description of the flow, while not requiring empirically derived transport equations to be solved. Early simulations of flow and turbulent structures above forests by Moeng [71], Shaw and Schumann [95], Kanda and Hino [44], and Dwyer et al. [24] show that important turbulence structures cannot be captured using a RANS model, but can be captured by an LES model. LES of channel flow through vegetated channels is presented by Cui and Neary [15], Stoesser et al. [98],[99] and Palau and Stoesser [76]. In-depth analyses of turbulence statistics and temporally-averaged characteristics of these flows demonstrate the superiority of LES to RANS in capturing fine-scale flow qualities. However, LES may

require significantly higher resolution than RANS.

Plant flexibility can be an important factor in resistance characteristics. Kouwen and Unny [51] performed experiments that simulate vegetation with plastic strips. They propose that there exist three basic types of flow through vegetation: when the vegetation remains erect and stationary, when the vegetation undergoes a waving motion, and when the vegetation is completely bent over. Similar results were found by Gourlay [32] using real grass instead of plastic strips. Huai et al. [38] show that waving vegetation influences stream-wise velocity and Reynolds stresses. There have been numerical studies incorporating plant flexibility. The approach in these studies, proposed by Kutija and Hong [53], is to assume a flexible 1D stem and a velocity profile and apply classical cantilever beam theory to simulate bending. In the region below the "effective vegetation height" a standard drag force is applied and a RANS or LES technique is used to model the flow. 2D LES simulation of this type of model was performed by Ikeda et al. [40]. Erduran and Kutija [25] use a 3D RANS technique with a combination of mixing length and eddy viscosity turbulence closure schemes. They also propose a quasi-3D coupling with the shallow water equations. Li and Xie [54], building on work involving stiff vegetation by Li and Zeng [55], add to the flexible vegetation model by assuming a thin plate of "foliage" and use a 3D LES scheme with Smagorinksy turbulence closure. While these models have been successful for meso-scale modeling of fully turbulent free surface flow over submerged and non-submerged vegetation, they do not consider a valid drag model for laminar or transitional flow

or micro-scale flow and do not capture the drag effects due to the complex geometries of vegetation at the micro-scale.

In this work, we approach vegetative resistance in terms of drag and a variable drag coefficient, and numerically simulate flow through vegetation for a wide range of Reynolds numbers with two main approaches. The first approach involves fully resolving the geometry of the porous domain containing vegetative obstacles. For low Reynolds number flows, drag can be modeled with techniques from the study of flow through porous media such as Darcy's law and non-Darcy models. We look at the theory behind Darcy's law and simple mathematical homogenization theory, including a computational method of calculating hydraulic conductivities. We present the Darcy-Forchheimer equation and other non-Darcy laws and discuss their derivations and experimental bases. In higher Reynolds number flows, eddies form and turbulence becomes important. The drag coefficients behave much differently in this flow than in the low Reynolds number region. We incorporate LES using the stabilized dynamic Smagorinsky eddy viscosity model, allowing us to realistically consider the effects of turbulence. Using a stabilized finite element method that we explain in depth in the next chapter, we solve the equations of motion on complex, vegetated 2D and 3D domains with highly-resolved meshes with periodic boundary conditions. This allows us to perform a qualitative analysis of drag over a large range of Reynolds numbers. We also analyze the accuracy of Darcy's law and non-Darcy equations, including the ranges of Reynolds numbers over which they are valid. An analysis of drag coefficients at high

Reynolds numbers is also performed. We analyze the drag coefficient and drag effects of vegetative resistance over a range of Reynolds numbers from slow, viscous flow to fully turbulent flow.

Our second approach is an immersed structure method. With this method, we use separate meshes for the fluid and vegetative obstacles and use ideas from fluid-structure interaction modeling to map the effects of the two on each other. With this method, we can model rigid and flexible vegetation. Plant flexibility is another important factor in vegetative drag. We model flexible vegetation as elastic inextensible cantilever beams. We present the theory behind such beam models and some numerical techniques for solving them. We develop a method for coupling the fluid-vegetation systems and test its accuracy. We use this method to calculate bulk drag coefficients for channel flows and wave tanks containing vegetative obstacles. Replicating the geometry of experimental setups as closely as possible, we verify the presented methods by comparing to experimental results.

Chapter 2

Flow Model

In this chapter, we develop the model that is used in almost all of the flow simulations in this dissertation. Beginning with the fundamental Navier-Stokes equations, we explain the formulation of a continuous Galerkin finite element method using variational multiscale stabilization. We explain the importance of using a proper turbulence model and present the dynamic Smagorinksy that we prefer to use. Finally, we verify our flow model with a difficult benchmark problem.

2.1 Introduction

The standard model for incompressible Newtonian flow is the Navier-Stokes equations. This is a system of conservation laws for conservation of mass and momentum. In conservative form they are

$$\nabla \cdot \mathbf{v} = 0 \tag{2.1}$$

$$\frac{\partial \mathbf{v}}{\partial t} + \nabla \cdot \left(\mathbf{v} \otimes \mathbf{v} - \nu(\nabla \mathbf{v} + \nabla \mathbf{v}^T) \right) + \frac{\nabla p}{\rho} - \mathbf{g} = 0 \tag{2.2}$$

where $\mathbf{v}$ is the velocity, p is the pressure, ρ is the fluid density, ν is the kinematic viscosity, and $\mathbf{g}$ is a body force including gravity.

2.2 Variational Formulation

Let Ω be the domain of the fluid region. Suppose that the boundary, $\partial\Omega$ has two partitionings $\{\Gamma_D^p, \Gamma_N^p\}$ and $\{\Gamma_D^v, \Gamma_N^v\}$. Suppose that we have the boundary conditions

$$p = p_D \text{ on } \Gamma_D^p \tag{2.3}$$

$$\mathbf{v} \cdot \mathbf{n} = h_N^p \text{ on } \Gamma_N^p \tag{2.4}$$

$$\mathbf{v} = \mathbf{v}_D \text{ on } \Gamma_D^v \tag{2.5}$$

$$\left[\mathbf{v} \otimes \mathbf{v} - \nu(\mathbf{x})(\nabla \mathbf{v} + \nabla \mathbf{v}^T)\right] \cdot \mathbf{n} = \mathbf{h}_N^v \text{ on } \Gamma_N^v. \tag{2.6}$$

Assume that we have initial conditions

$$p(\mathbf{x}, 0) = p_0 \tag{2.7}$$

$$\mathbf{v}(\mathbf{x}, 0) = \mathbf{v}_0. \tag{2.8}$$

Define the trial function spaces

$$V^p = \{w | w \in H^1(\Omega) \ and \ w = p_D \ on \ \Gamma_D^p\} \tag{2.9}$$

$$\mathbf{V}^v = \{\mathbf{w} | \mathbf{w} \in H^1(\Omega) \ and \ \mathbf{w} = \mathbf{v}_D \ on \ \Gamma_D^v\}. \tag{2.10}$$

Now, where $t \in [0, T]$ is time, we define the time-dependent trial function spaces: $V_t^p = \{w | w(t) = V^p\}$ and $\mathbf{V}_t^v = \{\mathbf{w} | \mathbf{w}(t) \in \mathbf{V}^v\}$. Define the test function spaces $W^p = \{w | w \in H^1(\Omega) \ and \ w = 0 \ on \ \Gamma_D^p\}$ and $\mathbf{V}^v = \{\mathbf{w} | \mathbf{w} \in H^1(\Omega) \ and \ \mathbf{w} = \mathbf{v}_D \ on \ 0\}$. We multiply the equations in (2.1) by the respective test functions.

$$\int_\Omega (\nabla \cdot \mathbf{v}) w^p d\Omega = 0 \tag{2.11}$$

$$\int_\Omega \left(\frac{\partial \mathbf{v}}{\partial t} + \nabla \cdot \left(\mathbf{v} \otimes \mathbf{v} - \nu(\nabla \mathbf{v} + \nabla \mathbf{v}^T) \right) + \frac{\nabla p}{\rho} - \mathbf{g} \right) \mathbf{w}^v d\Omega = 0. \quad (2.12)$$

Integrating by parts, we have the variational formulation: find $p \in V_t^p$ and $\mathbf{v} \in \mathbf{V}_t^v$ such that

$$-\int_\Omega \mathbf{v} \cdot \nabla w^p d\Omega = -\int_{\Gamma_N^p} h^p d\Gamma \ \forall w^p \in W^p, \quad (2.13)$$

$$\begin{aligned} \int_\Omega \frac{\partial \mathbf{v}}{\partial t} \mathbf{w}^v - \mathbf{v} \otimes \mathbf{v} \cdot \nabla \mathbf{w}^v d\Omega &= \int_\Omega \nu(\mathbf{x})(\nabla \mathbf{v} + \nabla \mathbf{v}^T) \cdot \nabla \mathbf{w}^v d\Omega \\ &+ \int_\Omega \left(\mathbf{g} - \frac{1}{\rho} \nabla p \right) \mathbf{w}^v d\Omega \\ &- \int_{\Gamma_N^v} \mathbf{h}_N^v d\Gamma \ \forall \mathbf{w}^v \in \mathbf{W}^v \end{aligned} \quad (2.14)$$

2.3 Continuous Galerkin Formulation

Let $\mathbf{M}^h$ be a simplicial mesh in $\mathbf{R}^n$ with $n = 2, 3$ containing N_e elements, $\{\Omega_e\}$ for $e = 1, 2, .., N_e$. Let h_e be the diameter of Ω_e. Let $P^k(\Omega_e)$ be the set of polynomials of order k on Ω_e. Define the discrete spaces:

$$V_h^p = \{p_h \in V^p \cap C^0(\overline{\Omega}) | p_h \in P_{\Omega_e}^k(\Omega_e)\} \quad (2.15)$$

$$W_h^p = \{w_h^p \in W^p \cap C^0(\overline{\Omega}) | w_h^p \in P_{\Omega_e}^k(\Omega_e)\} \quad (2.16)$$

$$\mathbf{V}_h^v = \{\mathbf{v}_h \in \mathbf{V}^v \cap \mathbf{C}^0(\overline{\Omega}) | \mathbf{v}_h \in \mathbf{P}_{\Omega_e}^k(\Omega_e)\} \quad (2.17)$$

$$\mathbf{W}_h^v = \{\mathbf{v}_h \in \mathbf{W}^v \cap \mathbf{C}^0(\overline{\Omega}) | \mathbf{v}_h \in \mathbf{P}_{\Omega_e}^k(\Omega_e)\}. \quad (2.18)$$

The classical continuous Galerkin formulation is: find $p_h \in V_h^p$ and $\mathbf{v}_h \in \mathbf{V}_h^v$ such that

$$-\int_\Omega \mathbf{v}_h \cdot \nabla w_h^p d\Omega = -\int_{\Gamma_N^p} h^p d\Gamma, \quad \forall w_h^p \in W_h^p \quad (2.19)$$

$$\begin{aligned}\int_\Omega \frac{\partial \mathbf{v}_h}{\partial t}\mathbf{w}_h^v - \mathbf{v}_h \otimes \mathbf{v}_h \cdot \nabla \mathbf{w}_h^v d\Omega &= \int_\Omega \nu(\mathbf{x})(\nabla \mathbf{v}_h + \nabla \mathbf{v}_h^T) \cdot \nabla \mathbf{w}_h^v d\Omega \\ &+ \int_\Omega \left(\mathbf{g} - \frac{1}{\rho}\nabla p_h\right)\mathbf{w}_h^v d\Omega \\ &- \int_{\Gamma_N^v} \mathbf{h}_N^v d\Gamma, \quad \forall \mathbf{w}_h^v \in \mathbf{W}_h^v. \end{aligned} \tag{2.20}$$

2.4 Variational Multiscale Formulation

When the diffusive effects are much smaller than advective effects, the classical continuous Galerkin method tends to be oscillatory. It becomes essential to add stabilization to the formulation. The dominant technique in computational fluid dynamics is to perform a multiscale decomposition of the solution to derive a stabilized method. Stabilized methods tend to reduce the oscillations in the solution without dramatically adding computational cost. Common multiscale decomposition approaches include the multiscale finite element method, the subgrid upscaling technique, and the mortar method. These methods incorporate small-scale heterogeneity into the formulation.

The variational multiscale (VMS) method, developed by Hughes [39], is a method that decomposes the problem into a grid-scale problem and a subgrid-scale problem. We derive the VMS method for a system of nonlinear conservation laws

$$\frac{\partial \mathbf{u}}{\partial t} + \nabla \cdot (\mathbf{f}(\mathbf{u}) - \mathbf{D}(\mathbf{u})\nabla \mathbf{u}) = 0 \tag{2.21}$$

where $\mathbf{u}(\mathbf{x})$ is the solution vector, $\mathbf{x} \in \Omega$, and $t \in (0, T]$. We call $\mathbf{f}$ the advective flux and $\mathbf{D}$ the diffusive flux. Let the boundary of the domain $\partial\Omega$

be decomposed into Γ_D and Γ_N where the essential and natural boundary conditions respectively are imposed, i.e.

$$\mathbf{u} = \overline{\mathbf{u}} \text{ on } \Gamma_D \text{ and} \tag{2.22}$$

$$(\mathbf{f} - \mathbf{D}\nabla\mathbf{u}) \cdot \mathbf{n} = \overline{\mathbf{F}}. \tag{2.23}$$

We assume the initial condition

$$\mathbf{u}(\mathbf{x}, t = 0) = \mathbf{u}_0(\mathbf{x}), \ \mathbf{x} \in \overline{\Omega}. \tag{2.24}$$

This VMS formulation for nonlinear conservation laws using an algebraic subgrid scale model (ASGS) is shown by Juanes and Patzek in [42].

2.4.1 Weak Form

Define the variational spaces

$$\mathbf{V} := \{\mathbf{v} \in \mathbf{W} | \mathbf{v} = \overline{\mathbf{u}} \text{ on } \Gamma_D\} \text{and}$$

$$\mathbf{V}_0 := \{\mathbf{v} \in \mathbf{W} | \mathbf{v} = 0 \text{ on } \Gamma_D\}$$

where $\mathbf{W}$ is the appropriate Sobolev space depending on $\mathbf{D}$. Define

$$(\partial_t \mathbf{u}, \mathbf{v}) = \int_\Omega \frac{\partial \mathbf{u}}{\partial t} \cdot \mathbf{v} d\Omega, \tag{2.25}$$

$$a(\mathbf{u}, \mathbf{v}; \mathbf{w}) = -\int_\Omega \mathbf{f}(\mathbf{w}) \cdot \nabla \mathbf{v} d\Omega + \int_\Omega \mathbf{D}(\mathbf{w}) \nabla \mathbf{u} \cdot \nabla \mathbf{v} d\Omega, \tag{2.26}$$

$$l(\mathbf{v}) = -\int_{\Gamma_N} \overline{\mathbf{F}} \cdot \mathbf{n} d\Gamma. \tag{2.27}$$

The weak form of the problem for each $t \in (0, T]$ is to find $\mathbf{u} \in \mathbf{V}$ such that

$$(\partial_t \mathbf{u}, \mathbf{v}) + a(\mathbf{u}, \mathbf{v}; \mathbf{u}) = l(\mathbf{v}), \quad \forall \mathbf{v} \in \mathbf{V}_0. \tag{2.28}$$

2.4.2 Galerkin Method

Let $\mathbf{V}_h \subset \mathbf{V}$ and $\mathbf{V}_{h,0} \subset \mathbf{V}_0$ be conforming finite-dimensional spaces of piecewise polynomials on a finite element mesh. Galerkin's method is to find $\mathbf{u}_h \in \mathbf{V}_h$ such that for each t

$$(\partial_t \mathbf{u}_h, \mathbf{v}_h) + a(\mathbf{u}_h, \mathbf{v}_h; \mathbf{u}_h) = l(\mathbf{v}_h), \quad \forall \mathbf{v}_h \in \mathbf{V}_{h,0}. \tag{2.29}$$

2.4.3 Multiscale Split

Suppose that $\mathbf{V}$ can be expressed as the direct sum of two spaces

$$\mathbf{V} = \mathbf{V}_h \oplus \tilde{\mathbf{V}}. \tag{2.30}$$

We call $\mathbf{V}_h$ the space of resolved scales and $\tilde{\mathbf{V}}$ the space of subgrid-scales. Note that $\tilde{\mathbf{V}}$ is an infinite dimensional space. There is a unique multiscale split

$$\mathbf{u} = \mathbf{u}_h + \tilde{\mathbf{u}}. \tag{2.31}$$

For nonlinear problems, Picard or Newton iterative methods are generally used. For these methods for each iterative step (k) it is natural to represent the solution as

$$\mathbf{u}^{(k)} = \mathbf{u}^{(k-1)} + \delta\mathbf{u}^{(k-1)}. \tag{2.32}$$

Using the multiscale split, we have

$$\mathbf{u}^{(k-1)} = \mathbf{u}_h^{(k-1)} + \tilde{\mathbf{u}}^{(k-1)} \tag{2.33}$$

$$\delta\mathbf{u}^{(k-1)} = \delta\mathbf{u}_h^{(k-1)} + \delta\tilde{\mathbf{u}}^{(k-1)} \tag{2.34}$$

Assuming $\mathbf{u}^{(k-1)} \approx \mathbf{u}_h^{(k-1)}$, we have

$$\mathbf{u}^{(k)} \approx \mathbf{u}_h^{(k)} + \delta\tilde{\mathbf{u}}^{(k-1)}. \tag{2.35}$$

For simplicity, we drop the superscripts $\mathbf{u} \approx \mathbf{u}_h + \delta\tilde{\mathbf{u}}$.

We split the solution and the test function into the multiscale elements:

$$\mathbf{u} = \mathbf{u}_h + \delta\tilde{\mathbf{u}} \in \mathbf{V} = \mathbf{V}_h \oplus \tilde{\mathbf{V}} \tag{2.36}$$

$$\mathbf{v} = \mathbf{v}_h + \tilde{\mathbf{v}} \in \mathbf{V}_0 = \mathbf{V}_{h,0} \oplus \tilde{\mathbf{V}}. \tag{2.37}$$

(2.29) can now be split into a grid scale problem

$$(\partial_t(\mathbf{u}_h + \delta\tilde{\mathbf{u}}), \mathbf{v}_h) = a(\mathbf{u}_h + \delta\tilde{\mathbf{u}}, \mathbf{v}_h; \mathbf{u} + \delta\tilde{\mathbf{u}}) = l(\mathbf{v}_h), \quad \forall \mathbf{v}_h \in \mathbf{V}_{h,0} \tag{2.38}$$

and a subgrid scale problem

$$(\partial_t(\mathbf{u}_h + \delta\tilde{\mathbf{u}}), \tilde{\mathbf{v}}) = a(\mathbf{u}_h + \delta\tilde{\mathbf{u}}, \tilde{\mathbf{v}}; \mathbf{u} + \delta\tilde{\mathbf{u}}) = l(\tilde{\mathbf{v}}), \quad \forall \tilde{\mathbf{v}} \in \mathbf{V}_{h,0}. \tag{2.39}$$

2.4.4 Subgrid Scale Problem

Consider the flux term in (2.39) as a sum of integrals over each element. Integrate by parts on each element :

$$a(\mathbf{u}_h + \delta\tilde{\mathbf{u}}, \tilde{\mathbf{v}}; \mathbf{u} + \delta\tilde{\mathbf{u}})$$

$$\begin{aligned}
&= -\sum_e \int_{\Omega_e} (\mathbf{f}(\mathbf{u} + \delta\tilde{\mathbf{u}}) - \mathbf{D}(\mathbf{u} + \delta\tilde{\mathbf{u}})\nabla(\mathbf{u}_h + (\delta\tilde{\mathbf{u}}))) \cdot \nabla\tilde{\mathbf{v}} d\Omega \\
&= -\sum_e \int_{\Omega_e} \nabla \cdot (\mathbf{f}(\mathbf{u} + \delta\tilde{\mathbf{u}}) - \mathbf{D}(\mathbf{u} + \delta\tilde{\mathbf{u}})\nabla(\mathbf{u}_h + (\delta\tilde{\mathbf{u}}))) \cdot \tilde{\mathbf{v}} d\Omega \\
&- \sum_e \int_{\Gamma_e} ((\mathbf{f}(\mathbf{u} + \delta\tilde{\mathbf{u}}) - \mathbf{D}(\mathbf{u} + \delta\tilde{\mathbf{u}})\nabla(\mathbf{u}_h + (\delta\tilde{\mathbf{u}}))) \cdot \mathbf{n}) \cdot \tilde{\mathbf{v}} d\Gamma
\end{aligned}$$

Assuming continuity of flux over interior element boundaries

$$-\sum_e \int_{\Gamma_e} \left(\left(\mathbf{f}(\mathbf{u}+\delta\tilde{\mathbf{u}}) - \mathbf{D}(\mathbf{u}+\delta\tilde{\mathbf{u}})\nabla\left(\mathbf{u}_h + (\delta\tilde{\mathbf{u}})\right)\right)\cdot\mathbf{n}\right)\cdot\tilde{\mathbf{v}}\, d\Gamma$$

$$\approx -\int_{\Gamma_n} \tilde{\mathbf{F}}\cdot\tilde{\mathbf{v}}\, d\Gamma \equiv l(\tilde{\mathbf{v}}) \tag{2.40}$$

Approximate the total flux with a Taylor expansion about $\mathbf{u}_h$:

$$\begin{aligned}
\mathbf{f}(\mathbf{u}+\delta\tilde{\mathbf{u}}) - \mathbf{D}(\mathbf{u}+\delta\tilde{\mathbf{u}})\nabla\left(\mathbf{u}_h + (\delta\tilde{\mathbf{u}})\right) &= \mathbf{f}(\mathbf{u}_h) - \mathbf{D}(\mathbf{u}_h)\nabla\mathbf{u}_h \\
&+ \mathbf{f}'(\mathbf{u}_h)\delta\tilde{\mathbf{u}} - (\mathbf{D}'(\mathbf{u}_h)\delta\tilde{\mathbf{u}})\nabla\mathbf{u}_h \\
&- \mathbf{D}(\mathbf{u}_h)\nabla(\delta\tilde{\mathbf{u}}) + \mathcal{O}(|\delta\tilde{\mathbf{u}}|^2). \qquad (2.41)
\end{aligned}$$

We define the linearized advection-diffusion operator

$$\mathscr{L}_{u_h}\mathbf{v} := \nabla\cdot\left[\mathbf{f}'(\mathbf{u}_h)\mathbf{v} - (\mathbf{D}'(\mathbf{u}_h)\mathbf{v})\nabla\mathbf{u}_h - \mathbf{D}(\mathbf{u}_h)\nabla\mathbf{v}\right]. \tag{2.42}$$

We can also write this as

$$\mathscr{L}_{u_h}\mathbf{v} := \nabla\cdot\left[\mathbf{A}(\mathbf{u}_h)\mathbf{v} - \mathbf{D}(\mathbf{u}_h)\nabla\mathbf{v}\right] \tag{2.43}$$

where

$$A_{ij}(\mathbf{u}_h) := \frac{\partial f_i(\mathbf{u}_h)}{\partial u_{h,j}} - \sum_k \frac{\partial D_{ik}(\mathbf{u}_h)}{\partial u_{h,j}}\nabla\mathbf{u}_{h,k} \tag{2.44}$$

Now, the flux term in the subgrid scale problem can be written as

$$a(\mathbf{u}_h+\delta\tilde{\mathbf{u}}, \tilde{\mathbf{v}}; \mathbf{u}+\delta\tilde{\mathbf{u}})$$

$$\begin{aligned}
&\approx -\sum_e \int_{\Omega_e} \nabla\cdot\left(\mathbf{f}(\mathbf{u}+\delta\tilde{\mathbf{u}}) - \mathbf{D}(\mathbf{u}+\delta\tilde{\mathbf{u}})\nabla\left(\mathbf{u}_h + (\delta\tilde{\mathbf{u}})\right)\right)\cdot\tilde{\mathbf{v}}\, d\Omega \\
&+ \sum_e \int_{\Omega_e} \mathscr{L}_{u_h}\delta\tilde{\mathbf{u}}\cdot\tilde{\mathbf{v}}\, d\Omega - \int_{\Gamma_n} \tilde{\mathbf{F}}\cdot\tilde{\mathbf{v}}\, d\Gamma \qquad (2.45)
\end{aligned}$$

Assume quasi-static subscales:

$$\partial_t \delta\tilde{\mathbf{u}} \approx 0. \tag{2.46}$$

Define the grid-scale residual

$$\mathscr{R}(\mathbf{u}_h) := -\partial_t \mathbf{u}_h - \nabla \cdot (\mathbf{f}(\mathbf{u}_h) - \mathbf{D}(\mathbf{u}_h)\nabla \mathbf{u}_h. \tag{2.47}$$

The subgrid-scale problem is now

$$\sum_e \int_{\Omega_e} \mathscr{L}_{u_h} \delta\tilde{\mathbf{u}} \cdot \tilde{\mathbf{v}} d\Omega = \sum_e \int_{\Omega_e} \mathscr{R}(\mathbf{u}_h) \cdot \tilde{\mathbf{v}} d\Omega \ \forall \tilde{\mathbf{v}} \in \tilde{V}. \tag{2.48}$$

We cannot expect to find an analytic solution to this infinite dimensional problem. We use an algebraic subgrid scale model (ASGS) for an algebraic approximation for the subscales:

$$\delta\tilde{\mathbf{u}} \approx \boldsymbol{\tau}_{u_h} \mathscr{R}(\mathbf{u}_h). \tag{2.49}$$

For a one-dimensional system, using linear elements and an element diameter of h

$$\boldsymbol{\tau}_{u_h} = \left(\frac{4}{h^2} \mathbf{D}(\mathbf{u}_h) + \frac{2}{h} \mathbf{A}(\mathbf{u}_h) \right)^{-1} \tag{2.50}$$

is an appropriate ASGS model.

2.4.5 Grid Scale Model

Define the adjoint of $\mathscr{L}_{u_h}$

$$\mathscr{L}^*_{u_h} \mathbf{v} := -\mathbf{A}^T(\mathbf{u}_h)\nabla \mathbf{v} - \nabla \cdot (\mathbf{D}^T(\mathbf{u}_h)\nabla \mathbf{v}) \tag{2.51}$$

and the associated boundary operator

$$\mathbf{b}^*_{u_h}\mathbf{v} := (\mathbf{D}^T(\mathbf{u}_h)\nabla\mathbf{v})\cdot\mathbf{n}. \tag{2.52}$$

Now (2.38) becomes

$$(\partial_t\mathbf{u}_h,\mathbf{v}_h)+a(\mathbf{u}_h,\mathbf{v}_h;\mathbf{u}_h)+\sum_e\int_{\Omega_e}\mathscr{L}^*_{u_h}\mathbf{v}_h\cdot\delta\tilde{\mathbf{u}}d\Omega+\sum_e\int_{\Gamma_e}\mathbf{b}^*_{u_h}\mathbf{v}_h\cdot\delta\tilde{\mathbf{u}}d\Gamma=l(\mathbf{v}_h) \tag{2.53}$$

$\forall\mathbf{v}_h\in\mathbf{V}_{h,0}$. Notice that this is (2.29) with two stabilization terms. We see that this VMS formulation is a type of Petrov-Galerkin method.

2.5 VMS Formulation for Navier-Stokes

We apply the VMS method derived above to the Navier-Stokes equations. This follows a formulation by Kees et al. [47]. We assume that all of the test and trial spaces can be written as a direct sum of the discrete finite element spaces introduced above and an infinite dimensional space of functions describing the subgrid scale behavior. So, $\mathbf{V}^v=\mathbf{V}^v_h\oplus\tilde{\mathbf{V}}^v$, $\mathbf{W}^v=\mathbf{W}^v_h\oplus\tilde{\mathbf{W}}^v$, $V^p=V^p_h\oplus\tilde{V}^p$, and $W^p=W^p_h\oplus\tilde{W}^p$, and all of the functions can be written as a unique sum of functions in the grid scale and subgrid scale spaces $\mathbf{v}_h+\tilde{\mathbf{v}}^v=\mathbf{v}^v\in\mathbf{V}^v$, $\mathbf{w}^v_h+\tilde{\mathbf{w}}^v=\mathbf{w}^v\in\mathbf{W}^v$, $p_h+\tilde{p}=p\in V^p$, and $w^p_h+\tilde{w}^p=w^p\in W^p$.

The adjoint operators required for the VMS formulation are

$$L^*_{v,p}w^p_h=-\nabla w^p_h \tag{2.54}$$

$$L^*_{v,v}\mathbf{w}^v_h=-\nabla\mathbf{w}^v\mathbf{v}^v_h-\nu\Delta\mathbf{w}^v_h \tag{2.55}$$

$$L^*_{p,v}\mathbf{w}^v_h = \left(\frac{\partial w^v_{h,x}}{\partial x}, \frac{\partial w^v_{h,y}}{\partial y}, \frac{\partial w^v_{h,z}}{\partial z}\right)^T, \tag{2.56}$$

where $L^*_{v,p}$ and $L^*_{p,v}$ are the adjoint operators corresponding to the divergence and pressure gradient operators. $L^*_{v,v}$ is obtained by linearizing the fluxes of the momentum equation.

Let $\mathbf{v}_{h,n}$ denote $\mathbf{v}_h$ at time step n. The ASGS approximations at time step n are given by

$$\tilde{p} = \tau_p R_p \tag{2.57}$$

$$\tilde{\mathbf{v}} = \boldsymbol{\tau}_v \mathbf{R}_v \tag{2.58}$$

where

$$\tau_p = 4\nu + 2\rho\|\mathbf{v}_{h,n-1}\|\hat{h} + |D'_t|\hat{h}^2 \tag{2.59}$$

$$\boldsymbol{\tau}_v = \frac{1}{4\rho/\hat{h}^2 + \frac{2\rho\|\mathbf{v}_{h,n-1}\|}{\hat{h}} + |\mathbf{D}'_t|} \tag{2.60}$$

and

$$R_p = \nabla \cdot \mathbf{v}_h \tag{2.61}$$

$$\mathbf{R}_v = \mathbf{D}_t\mathbf{v}_h + \mathbf{v}_{h,n-1}\cdot\nabla\mathbf{v}_h - \nu\Delta\mathbf{v}_h - \mathbf{g} + \frac{1}{\rho}\nabla p, \tag{2.62}$$

and $\hat{h} = h_e$ for $k = 1$ and $\hat{h} = h_e/2$ for $k = 2$. Notice that we lag the stabilization parameters in time.

The VMS finite element formulation is: find $p_h \in V^p_h$ and $\mathbf{v}_h \in \mathbf{V}^v_h$ such that

$$-\int_\Omega \mathbf{v}_h \cdot \nabla w^p_h d\Omega + \int_\Omega \tilde{\mathbf{v}} L^*_{v,p} w^p_h d\Omega = -\int_{\Gamma^p_N} h^p d\Gamma, \quad \forall w^p_h \in W^p_h \tag{2.63}$$

$$\begin{aligned}\int_\Omega \frac{\partial \mathbf{v}_h}{\partial t}\mathbf{w}_h^v - \mathbf{v}_h \otimes \mathbf{v}_h \cdot \nabla \mathbf{w}_h^v d\Omega &= \int_\Omega \nu(\mathbf{x})\nabla(\mathbf{v}_h + \mathbf{v}_h^T)\cdot\nabla \mathbf{w}_h^v d\Omega \\ &+ \int_\Omega \tilde{\mathbf{v}} L_{v,v}^* \mathbf{w}_h^v d\Omega + \int_\Omega \left(\mathbf{g} - \frac{1}{\rho}\nabla p_h\right)\mathbf{w}_h^v d\Omega \\ &+ \int_\Omega \tilde{p} L_{p,v}^* \mathbf{w}_h^v d\Omega \\ &- \int_{\Gamma_N^v} \mathbf{h}_N^v d\Gamma \;\; \forall \mathbf{w}_h^v \in \mathbf{W}_h^v \end{aligned} \tag{2.64}$$

2.6 Turbulence Modeling

Assuming a porous domain with the mean grain size as the length scale, the effects of turbulence in incompressible flow begin to be noticeable at Reynolds numbers near 70. When Re nears 100 there is turbulent flow in about half of the domain. Near 200 there is turbulence everywhere in the flow, and above 1000 the flow has fully developed turbulence. A great deal of energy from the mean flow is transformed into turbulent kinetic energy which cascades through eddies of decreasing size until it dissipates from the system. In most cases it is unreasonable to resolve a computational domain down to the smallest length scales of turbulent eddies, so it becomes essential to incorporate a turbulence model to capture the effects of the subgrid scale turbulent eddies. There are two main types of turbulence models: Reynolds Averaged Navier-Stokes (RANS) and Large Eddy Simulation (LES). We focus on LES methods.

2.6.1 Large Eddy Simulation

The LES equations are a filtered version of the Navier-Stokes equations

$$\frac{\partial \bar{u_i}}{\partial x_i} = 0 \tag{2.65}$$

$$\frac{\partial \bar{u_i}}{\partial t} + \frac{\partial \bar{u_i}\bar{u_j}}{\partial x_j} = -\frac{1}{\rho}\frac{\partial \bar{p}}{\partial x_i} + \nu\frac{\partial^2 \bar{u_i}}{\partial x_j \partial x_j} - \frac{\partial \tau_{ij}}{\partial x_j}. \tag{2.66}$$

The bar signifies a filtered term. An LES filtering operation is defined by

$$\overline{\phi(\boldsymbol{x}, t)} = \int_{-\infty}^{\infty}\int_{-\infty}^{\infty} \phi(\boldsymbol{r}, t')G(\boldsymbol{x} - \boldsymbol{r}, t - t')dt'd\boldsymbol{r} \tag{2.67}$$

where G is the filter convolution kernel. The choice of G defines the type of LES. ϕ can be separated into a filtered component $\overline{\phi}$ and sub-filtered component ϕ', so $\phi = \overline{\phi} + \phi'$. In order to close this system (2.66), we must model the term τ_{ij}. The most common model for this term, is the Smagorinsky model:

$$\tau_{ij} = -2\nu_T \bar{S_{ij}} \tag{2.68}$$

where

$$\bar{S_{ij}} = \frac{1}{2}\left(\frac{\partial \bar{u_i}}{\partial x_j} + \frac{\partial \bar{u_j}}{\partial x_i}\right) \tag{2.69}$$

is an entry of the strain rate tensor. The Smagorinksy model is in a class of LES models called eddy viscosity models. We can incorporate the above into an eddy viscosity ν_T with

$$\nu_T = (C_s\Delta_g)^2\sqrt{2\bar{S_{ij}}\bar{S_{ij}}}, \tag{2.70}$$

where Δ_g is the grid size and C_s is the Smagorinksy Constant taken as

$$C_s = 0.17.$$

The relationship between the Smagorinsky model for τ_{ij} and the corresponding Smagorinsky LES filter is based on the energy spectrum of homogenous, isotropic turbulence.

Use of the Smagorinksy LES model can be problematic if the flow is not fully turbulent everywhere in the flow. In this case, it tends to be overly diffusive and can cause unphysical results. The Germano dynamic model [31] is an LES model that does not assume that C_s is constant. C_s varies spatially and temporally depending on local flow characteristics. This allows it to be used accurately for flows with varying amounts of turbulence throughout the flow. It involves using a second larger filter $\hat{\cdot}$ called the test filter. The resolved stress tensor $\mathcal{L}$ is defined as

$$\mathcal{L} = T_{ij}^r - \hat{\tau}_{ij}^r \tag{2.71}$$

where $T_{ij}^r = \widehat{\overline{u_i}\overline{u_j}} - \hat{\overline{u}}_i\hat{\overline{u}}_j$ is the residual stress tensor for the test filter scale and $\hat{\tau}_{ij}^r = \widehat{\overline{u_i}\overline{u_j}} - \widehat{\overline{u_i}\overline{u_j}}$ is the residual stress tensor for the grid filter. $\mathcal{L}$ can be considered the contribution to the subgrid scale stresses at the length scales between the two filter sizes. The resulting equation for C_s is

$$C_s^2 = \frac{\mathcal{L}_{ij}\mathcal{M}_{ij}}{\mathcal{M}_{ij}\mathcal{M}_{ij}} \tag{2.72}$$

where $\mathcal{M}_{ij} = 2\overline{\Delta}^2\left(\overline{\left|\hat{S}\right|\hat{S}_{ij}} - \alpha^2\left|\overline{\hat{S}}\right|\overline{\hat{S}}_{ij}\right)$ and $\alpha = \frac{\hat{\Delta}}{\overline{\Delta}}$. Averaging over small regions gives

$$C_s^2 = \frac{\langle\mathcal{L}_{ij}\mathcal{M}_{ij}\rangle}{\langle\mathcal{M}_{ij}\mathcal{M}_{ij}\rangle}. \tag{2.73}$$

A full analysis of LES models is found in [80]. Now our system is the Navier-Stokes equations with an added eddy viscosity

$$\frac{\partial \mathbf{v}}{\partial t} + \nabla \cdot (\mathbf{v} \otimes \mathbf{v} - (\nu + \nu_T)\nabla \mathbf{v}) + \frac{\nabla p}{\rho} - \mathbf{g} = 0. \tag{2.74}$$

The rate of strain should be small for low Reynolds number flows, so ν_T will only have a significant effect for higher Reynolds number flows.

Voke [107] and Meneveau and Lund [69] developed more practical methods for calculating C_s. By assuming a Pao turbulent energy spectrum, for fully laminar flows we take $C_s = 0$, and for transitional and turbulent flows, we take

$$C_s^2(Re_\Delta) = 0.027 \times 10^{-3.23 Re_\Delta^{-0.92}} \tag{2.75}$$

where $Re_\Delta = \frac{\Delta_g^2 \sqrt{2\overline{\overline{S_{ij}}}\,\overline{\overline{S_{ij}}}}}{\nu}$ is the mesh-Reynolds number at a given point in the flow. This approximation to the full dynamic Smagorinsky method is the one that we utilize.

2.6.2 LES Verification

In order to establish that the LES model presented above is a realistic one we evaluate it against experimental data. Liu et al. [59] performed an experimental study of flow through rigid vegetation. They simulated a vegetated field with several different periodic arrangements of rigid dowels. They experimented with both emergent and submerged vegetation and smooth and rough beds. We validated the LES method by comparing to their Experiment 1.2. In this setup, rigid, smooth dowels 0.076 m tall and 0.00635 m in diameter

are arranged in a grid with their centers 0.1016 m apart. Their flume was 4.3 m long and 0.3 m wide with a constant slope of 0.003 and the dowels started 1.3 m downstream. The flow rate was 0.0057 m^3/s and the flow depth was 0.071 m. Therefore the dowel is emergent. The flow is fully developed by the time it is 2.25 m downstream of the inflow boundary. They made instantaneous longitudinal velocity measurements with one-dimensional laser Doppler velocimeters at specific locations in the flow and throughout the vertical profile at these points. We focus on 3 of these locations. Measurement 1 is taken 4 dowel diameters directly downstream from the center of a dowel. Measurement 2 is taken 8 dowel diameters directly downstream from the center of the dowel. Measurement 4 is taken 8 dowel diameter directly downstream and 8 dowel diameters to the right (with respect to flow direction) of the center of the dowel.

It would be unrealistic for us to fully simulate their complete setup. We simulate on a 0.0762 m x 0.0762 m x 0.071 m rectangular prism with a cylinder of diameter 0.00635 mm at (0.0254 m, 0.0254 m). Our mesh has 223,930 unstructured tetrahedral elements. We use standard parameters $\rho = 998.0$ kg/m^3 and $\nu = 1.0 \times 10^{-6}$ m^2/s for water. We impose no slip boundary conditions on the bottom and on the cylinder, a free surface condition on the top, periodic conditions on the transverse sides, outflow conditions on the back, and a Dirichlet condition on the front face. Starting with zero initial conditions we ramp up the velocity over time up to 0.2676 m/s, which is the mean velocity of the flow in the experiment. We then let the flow develop

over 10 s and take instantaneous snapshots of the velocities profiles at the 3 measurement locations shown in Figure 2.1. These qualitatively match quite well with Figure 2 in the paper of Liu et al. [59]. As with their results, the general trend is that the lowest velocities occur at locations behind the cylinder. We also see that the velocity at location 4, in the free stream, is always the highest. As with the experiments, we see that the dowel has a large effect on the profile, with the velocity profiles being nearly vertical in the intermediate depths. As with their results, we see spikes in velocity just above the bed. This is due to a horseshoe vortex at the base of the cylinder. Capturing this spike validates our method. The magnitude of the velocities is very close to the experimental results at all 3 locations. This shows that the LES method can realistically model the complex flow dynamics for high-velocity flow around these types of structures.

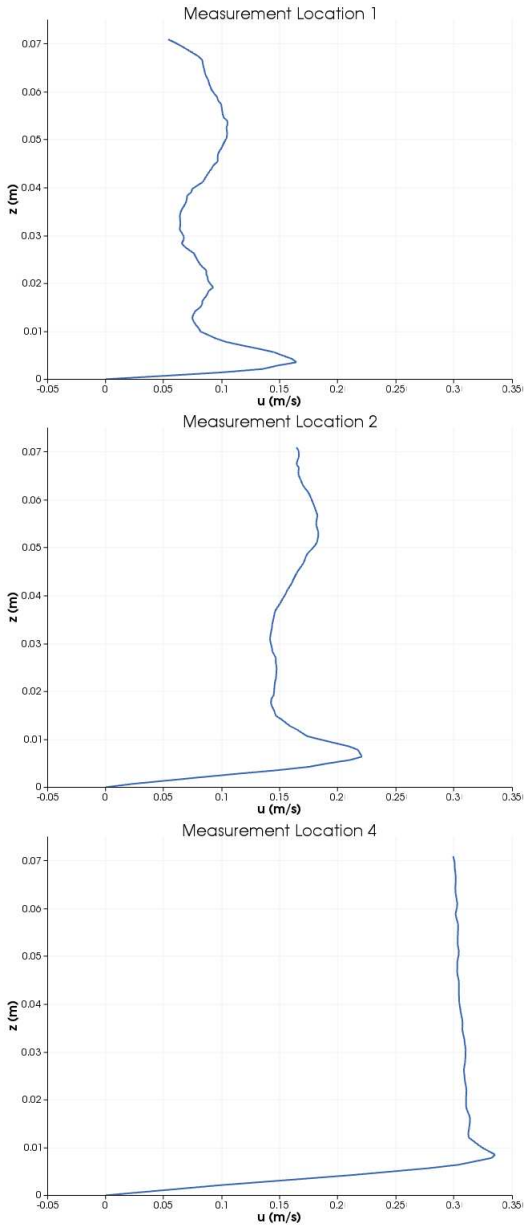

Figure 2.1: Longitudinal velocity profiles with respect to depeth (z) at locations 1, 2 and 4 respectively for LES verification study.

Chapter 3

Computational Upscaling of Flow Through Domains Containing Rigid Vegetation

3.1 Introduction

For many types of physical processes there are different characteristics at different length scales. It is often computationally unreasonable to resolve the smallest length scales of interest for a large-scale problem. Upscaling is the process of analyzing small-scale dynamics to describe larger scale phenomena. Flow through vegetated regions is an example of one of these processes where the dynamics are at many length scales. For a large vegetated region, it would be nearly impossible to resolve all of the complex geometry and flow characteristics, so we must use upscaling.

Mathematical homogenization is a common upscaling technique. It involves mathematically deriving effective equations to describe large-scale dynamics by satisfying to some degree the dynamics of the smaller scales. Most homogenization theory exists for linear problems. The topic of homogenization for nonlinear problems is mostly open, and most work in the field involves problems that are only slightly nonlinear. We use techniques from mathematical homogenization for highly viscous flows; however, for inertial flows, which

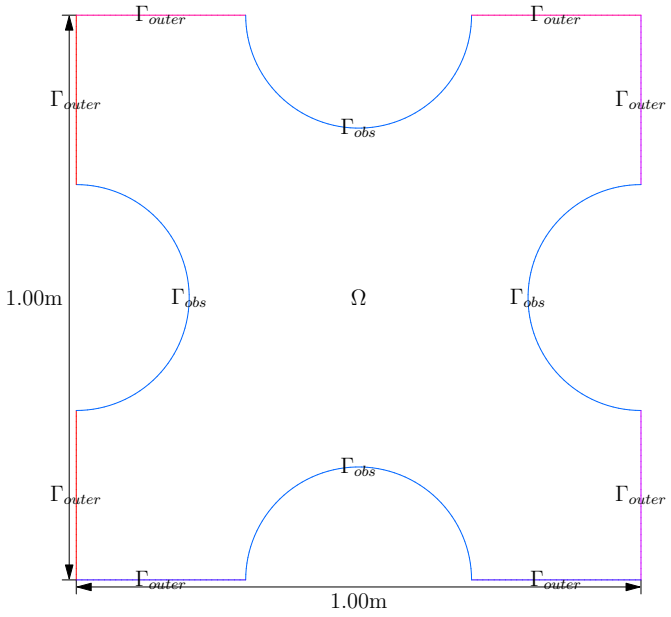

Figure 3.1: The periodic cell Y.

we are more likely to see in nature in vegetated domains, we must perform computational upscaling. This chapter explains a method of computational upscaling that we have published in [65].

3.2 The Concept of Drag

Fluid viscosity causes resistance in the flow around immersed bodies. Viscous effects can produce three different types of resistance as described by Rouse [90]. At low Reynolds numbers, inertial effects of flow are negligible compared to those caused by viscous stress. We see that these viscous effects extend a great distance into the surrounding flow, causing a widespread distortion of the flow pattern. This is known as "deformation drag." At higher

Reynolds numbers, the deformed region of the flow is much smaller, limited to a thin layer surrounding the body. Therefore the resulting shear is along the boundary surface. We call this "surface drag." If the form of the body is such that there is separation in the flow, it produces "form drag." In this scenario, there is a lower intensity of pressure in the wake of the object which causes a resultant force which opposes the motion. Under certain conditions form drag can reduce viscous stresses to insignificant values.

We write the relationship for the force of drag opposing motion as

$$F = C_d A \frac{\rho V^2}{2} \tag{3.1}$$

where F is the drag force, A is the cross sectional area of the body, V is the magnitude of the velocity of the flow, and C_d is a drag coefficient. We note that

$$C_d = \frac{F}{A\rho V^2/2} \tag{3.2}$$

is dependent on Reynolds number. This coefficient is similar to the Darcy friction factor for the Darcy-Weisbach equation used in modeling flow in rough pipes. In multiple dimensions, we can write the drag equation as

$$\mathbf{F} = \mathbf{C_d} A \frac{\rho \left|\mathbf{V}\right| \mathbf{V}}{2} \tag{3.3}$$

where now $\mathbf{C_d}$ is a tensor and $\mathbf{V}$ is the mean velocity vector. For calculating $\mathbf{C_d}$, we take $\mathbf{F}$ as the hydraulic gradient

$$\mathbf{F} = -LA(\nabla p - \rho \mathbf{f}) \tag{3.4}$$

where L is the domain length and $\mathbf{f}$ is a forcing term which includes the gravitational constant. In this paper, we study how $\mathbf{C_d}$ changes over a large range of Reynolds numbers for various vegetated domains.

3.3 Upscaling Laws

We will use some techniques from the study of flow through porous media for our analysis of flow through vegetated regions. Tightly packed vegetation can be analogous to a porous medium. We define Reynolds number as

$$Re = \frac{Vd}{\nu} \tag{3.5}$$

where V is the mean flow rate over the total volume including the obstructions (specific discharge), d is the mean diameter of the individual plants, and ν is the kinematic viscosity of the fluid. Reynolds number is a non-dimensional value representing the ratio of inertial effects to viscous effects. In most studies of subsurface flow, it is assumed that viscous effects dominate, so inertial effects can be ignored.

3.3.1 Darcy's Law

For very low Reynolds number flows ($Re < 1$) Darcy's law is the basic constitutive equation for flow in porous media. It was originally determined experimentally by Henry Darcy in 1856. As defined by Bear [5], Darcy's law says that for a homogeneous incompressible fluid, the three-dimensional

constitutive equation is

$$\mathbf{v} = -\frac{\mathbf{K}}{\mu}(\nabla p - \rho \mathbf{f}), \tag{3.6}$$

where $\mathbf{v}$ is the mean velocity vector, ∇p is the pressure gradient, $\mathbf{K}$ is the "hydraulic permeability" tensor with units L^2, μ is the dynamic viscosity of the fluid, ρ is the fluid density, and $\mathbf{f}$ is the forcing vector containing the gravitational constant. The hydraulic permeability tensor depends solely on the properties of the porous medium. Since we are dealing with an incompressible fluid, we also assume that the flow is divergence free:

$$\nabla \cdot \mathbf{v} = 0. \tag{3.7}$$

For Reynolds numbers small enough for Darcy's law to be valid, we only need to know the hydraulic permeability tensor to be able to accurately describe the mean flow. $\mathbf{K}$ is calculated by mathematical homogenization.

Assume the domain is periodic and perforated. This can be seen in Figure 3.1. Let Y be a standard periodic cell with standard obstacles, $G \subset\subset Y$, with piecewise smooth boundaries Γ_{obs}. The remainder is $\Omega = Y \setminus G$. This is the "fluid region". We call the outer fluid boundary of the cell that does not touch an obstacle Γ_{outer}. We assume the standard geometry of Y is repeated all throughout $\mathbf{R^N}$.

A fixed domain A is given by intersecting the ϵ multiple of this periodic geometry. This is denoted by

$$\Omega^\epsilon = A \cap (\epsilon \Omega)$$

and

$$\Gamma_{obs}^{\epsilon} = A \cap (\epsilon \Gamma_{obs}).$$

For the simple theory, we assume that

$$\partial A \cap \epsilon \Gamma_{obs} = \emptyset;$$

however, in practice this condition is not necessary.

Now, we perform homogenization on the standard Stokes problem to formally derive Darcy's Law as shown by Hornung [37]. We start with the following problem on the pore scale

$$\begin{aligned} \epsilon^2 \mu \Delta \mathbf{v}^{\epsilon}(x) = \nabla p^{\epsilon}(x), \quad & x \in \Omega^{\epsilon}, \\ \nabla \cdot \mathbf{v}^{\epsilon}(x) = 0 \quad & x \in \Omega^{\epsilon} \\ \mathbf{v}^{\epsilon}(x) = 0, \quad & x \in \Gamma_{obs}^{\epsilon} \end{aligned} \tag{3.8}$$

where μ is the dynamic viscosity, $\mathbf{v}$ is velocity and p is pressure. We assume that the unknowns p^{ϵ} and $\mathbf{v}^{\epsilon}$ can be written as asymptotic expansions with respect to ϵ. That is

$$\mathbf{v}^{\epsilon}(x) = \mathbf{v}_0(x, y) + \epsilon \mathbf{v}_1(x, y) + \epsilon^2 \mathbf{v}_2(x, y)... \tag{3.9}$$

and

$$p^{\epsilon}(x) = p_0(x, y) + \epsilon p_1(x, y) + \epsilon^2 p_2(x, y)... \tag{3.10}$$

where the coefficient functions v_i and p_i are Y-periodic with respect to y. This results in the equations

$$\begin{aligned} \epsilon^0 \mu \Delta_y \mathbf{v}_0(x, y) + \epsilon^1(...) + ... \quad &= \quad \epsilon^{-1} \nabla_y p_0(x, y) \\ &+ \quad \epsilon^0 (\nabla_y p_1(x, y) + \nabla_x p_0(x, y)) + \epsilon^1(...) + ..., \end{aligned}$$

$$\epsilon^{-1}\nabla_y \cdot \mathbf{v}_0(x,y) + \epsilon^0(\nabla_y \cdot \mathbf{v}_1(x,y) + \nabla_x \cdot \mathbf{v}_0(x,y) + \epsilon^1(...) + ... = 0, \quad (3.11)$$

for all $y \in \Omega$, and

$$\epsilon^0 \mathbf{v}_0(x,y) + \epsilon^1 \mathbf{v}_1(x,y) + ... = 0, \quad (3.12)$$

for all $y \in \Gamma$. Now we compare coefficients. The ϵ^{-1} term in the first equation gives

$$\nabla_y p_0(x,y) = 0, \quad (3.13)$$

for all $y \in \Omega$, hence, $p_0(x,y) = p_0(x)$ independently of y. The ϵ^0 term yields

$$\mu \Delta_y \mathbf{v}_0(x,y) = \nabla_y p_1(x,y) + \nabla_x p_0(x), \quad (3.14)$$

for all $y \in \Omega$ and the ϵ^{-1} term in the second equation gives

$$\nabla \cdot \mathbf{v}_0(x,y) = 0, \quad (3.15)$$

for all $y \in \Omega$. As usual

$$\nabla_x p_0(x) = \sum_j e_j \partial_j p_0(x) \quad (3.16)$$

where e_j is the unit vector in the j direction.

Now the cell problem is to find the Y-periodic vector fields $\mathbf{w}_j(y)$ with components $w_{ji}(y)$ that solve the Stokes problems,

$$\begin{aligned} \Delta_y \mathbf{w}_j(y) &= \nabla_y \pi_j(y) - \mathbf{e}_j \quad y \in \Omega \\ \nabla \cdot \mathbf{w}_j(y) &= 0 \quad y \in \Omega \\ \mathbf{w}_j(y) &= 0 \quad y \in \Gamma_{obs} \end{aligned} \quad (3.17)$$

where $\pi_j(y)$ are the corresponding Y-periodic pressure fields, $\mathbf{e}_j$ is the unit vector in the j direction, ν is the kinematic viscosity and ρ is the fluid density.

Notice that the third equation is our standard no-slip condition on the walls of the vegetation. Using these cell functions, we easily obtain

$$\mathbf{v}_0(x,y) = -\frac{1}{\rho}\sum_j \mathbf{v}_j(y)\partial_j p_0(x). \tag{3.18}$$

The average vector field is defined by

$$\overline{\mathbf{u}}(\mathbf{x}) = \int_\beta \mathbf{v}_0(x,y)dy,$$

and its ith component is expressed by

$$\overline{u}_i(x) = -\frac{1}{\mu}\sum_j k_{ij}\partial_{x_j} p_0(x),$$

with

$$k_{ij} = \int_\Omega w_{ji}(y)dy. \tag{3.19}$$

By introducing the tensor $\mathbf{K} = k_{ij}$ we get the short expression

$$\overline{\mathbf{u}}(x) = -\frac{1}{\mu}\mathbf{K}\nabla p_0(x)$$

which is Darcy's Law.

We must still show that $\overline{\mathbf{u}}$ is divergence free. From the ϵ^0 term of (3.11).

$$\nabla_y \cdot \mathbf{v}_1(x,y) + \nabla_x \cdot v_0(x,y) = 0,$$

for al $y \in \Omega$. By integrating over Ω,

$$\begin{aligned}
\nabla_x \cdot \overline{\mathbf{u}}(x) &= \int_\Omega \nabla \cdot \mathbf{v}_0(x,y)dy \\
&= -\int_\Omega \nabla_y \cdot \mathbf{v}_1(x,y)dy \\
&= -\int_{\Gamma_{outer}} \mathbf{n} \cdot \mathbf{v}_1(x,y)d\Gamma_{outer}(y) \\
&= -\int_{\Gamma_{outer}} \mathbf{n} \cdot \mathbf{v}_1(x,y)d\Gamma_{outer}(y) - \int_{\partial Y} \mathbf{n} \cdot \mathbf{v}_1(x,y)d\Gamma_{outer}(y).
\end{aligned}$$

The boundary integral over Γ_{outer} is zero due to the term with ϵ^1 in (3.12) and the boundary integral over ∂Y is zero due to the Y-periodicity of $\mathbf{v}_1(x,y)$. Therefore $\overline{\mathbf{u}}$ is divergence free.

We can also write Darcy's Law in terms of the multi-dimensional drag coefficient. Using Darcy's Law and (3.4) we have

$$\mathbf{F} = LA\mu\mathbf{K^{-1}V}.$$

Comparing with the drag equation we obtain

$$\mathbf{C_d} = \frac{2L\mu}{\rho|\mathbf{V}|}\mathbf{K^{-1}}. \tag{3.20}$$

3.3.2 Darcy-Forchheimer Flow

It is observed experimentally that for flows with Reynolds numbers greater than 1 the ratio between hydraulic gradient and velocity gradually increases with increasing flow rate. It is generally thought that this increase is because inertial forces, with increasing Reynolds number, become much larger than the viscous forces. In this range, nonlinear behavior is seen. The

inertial terms in Navier-Stokes are no longer negligible, so the homogenization of Stokes equation is no longer the correct upscaling. Forchheimer noticed from empirical results that for higher Reynolds numbers, the relationship resembles Darcy's Law plus a quadratic term. This is called the Darcy-Forchheimer equation

$$-(\nabla p - \rho \mathbf{f}) = \mu \mathbf{K^{-1}} \mathbf{V} + \beta \rho |\mathbf{V}| \mathbf{V}. \tag{3.21}$$

The non-Darcy coefficient β is usually taken as a constant, but it is likely a tensor for anisotropic media. It is generally calculated experimentally by fitting to data. While the Darcy-Forchheimer equation has matched data from a large number of experiments quite well, it is often unacceptable, especially over a large range of Reynolds numbers as explained in Bear[5].

3.3.3 Other non-Darcy models

There have been many attempts at deriving the Darcy-Forchheimer Law using mathematical homogenization. One of the first was by Lions [58]. Similar techniques were done by Sanchez [91]. These types of techniques found that the obtained homogenization problems lead to polynomial filtration laws. This has been studied by Mei and Auriault [67], Wodie and Levy [112], and Rasoloarijaona and Ariault [83]. The results of these studies sees quadratic terms canceling, giving a cubic law

$$-(\nabla p - \rho \mathbf{f}) = \mu \mathbf{K^{-1}} \mathbf{V} + \beta \rho |\mathbf{V}|^2 \mathbf{V}. \tag{3.22}$$

This has been verified numerically for very small Reynolds numbers by solving the Navier-Stokes equations by Coulaud et al. [14], Rojas and Koplik [89], and Koch and Ladd [50]. However, this has only been verified where Darcy's Law is approximately valid, and the quadratic law seems to be more appropriate for higher Reynolds number flows. Some methods provide a result with quadratic and cubic terms

$$-(\nabla p - \rho \mathbf{f}) = \mu \mathbf{K^{-1}} \mathbf{V} + \beta \rho |\mathbf{V}| \mathbf{V} + \gamma \rho |\mathbf{V}|^2 \mathbf{V}. \tag{3.23}$$

Some, like Scheidegger [93], have also used power laws of the form,

$$-(\nabla p - \rho \mathbf{f}) = \mu \mathbf{K^{-1}} \mathbf{V} + \alpha_1 \mathbf{V}^{\alpha_2} \tag{3.24}$$

to fit empirical data. For (3.24) and (3.23), β, γ, α_1, and α_2 are model parameters that must be found empirically.

3.3.4 Higher Reynolds Number Flows

From experimental data we know that as Reynolds number increases above the region where Darcy's Law is valid, the nature of the flow changes. At low Reynolds numbers we see deformation drag; streamlines are greatly affected by the obstacles. As Reynolds number increases, we see separation occur and form drag occurs with less deformation. Eventually, streamlines shift and fixed eddies form in the wake of obstacles. The size of the eddies increases as Re increases. Around $Re = 70$ turbulence begins to occur. When Re reaches 75 the flow is turbulent in approximately half of the domain, and when Re nears 200 there is turbulence everywhere in the flow. This analysis

is discussed at length by Bear [5]. At high Reynolds numbers we see the drag force begin to balance with the driving force. Therefore, we see C_d become constant. Chaudhary et al. [12] explain that the change in drag from low Reynolds numbers to moderate Reynolds numbers is due to the increasing size of eddies within the pores. For high Reynolds numbers, the eddies fill up almost all of the pore space and can no longer grow, so hydraulic conductivity and drag coefficient become nearly constant.

Darcy's Law and the derivation of hydraulic conductivity above do not accurately model the nonlinear behavior in this range. As we see in the previous sections, the Darcy-Forchheimer Law and the related polynomial formulas do have some theoretical arguments and seem to match experimental data for the initial nonlinear region. However, there is not a theoretical basis to extrapolate these results to higher Reynolds numbers. In subsurface modeling, it is uncommon to deal with Reynolds numbers this large. Our main goal is to analyze the drag in this transitional region between Stokes and turbulent flow so that it can be applied to flow through vegetated regions where we do see Reynolds numbers in this range.

3.4 Method

3.4.1 Calculation of Hydraulic Conductivities

In order to describe C_d for low Reynolds number flows we can use the above method of mathematical homogenization to find hydraulic conductivities for various 2D and 3D domains. We computationally solve the Stokes

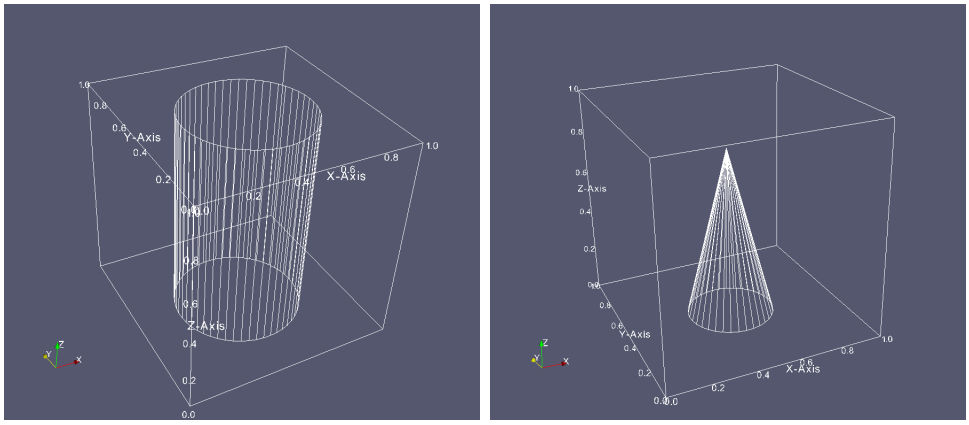

Figure 3.2: 3D domains containing cylinders and cones.

problems, (3.17). Since we are solving on a periodic cell, we use periodic boundary conditions. The weak formulation of these problems is a simpler version of what is done in Chapter 2. Once the periodic w and π fields are found, we use (3.19) to calculate $\mathbf{K}$, integrating with numerical quadrature. Then using (3.20), we are able to calculate the drag coefficients for these viscosity dominated flows.

For higher Reynolds number flows, we must perform "computational upscaling." Instead of solving the linear Stokes problems (3.17), we solve the cell LES problem:

$$\begin{aligned} \frac{\partial \mathbf{w}_j}{\partial t} + \nabla \cdot (\mathbf{w_j} \otimes \mathbf{w}_j - (\nu + \nu_T)\nabla \mathbf{w}_j) + \frac{\nabla p}{\rho} - \mathbf{f}_j = 0 \quad & y \in \Omega \\ \nabla \cdot \mathbf{w}_j(y) = 0 \quad & y \in \Omega \\ \mathbf{w}_j(y) = 0 \quad & y \in \Gamma_{obs} \end{aligned} \tag{3.25}$$

for a large range of $\mathbf{f}_j$ on the periodic cell to "steady-state". For moderate Reynolds numbers ($Re < 100$), there is a true steady-state solution that can be found using the steady Navier-Stokes equations which ignore the acceleration

term. For higher Reynolds numbers, the full cell LES problem (3.25) must be solved out in time until the solution becomes essentially steady. When the change of the volume averaged velocity is within a small tolerance between multiple time steps, we consider the mean flow to be essentially steady. For very high Reynolds numbers, the flow never becomes steady, so we must time-average the solution.

After solving the cell LES problem, we calculate corresponding drag forces and volume-averaged velocities. As for extremely low Reynolds number flows, we solve the Stokes cell problems from mathematical homogenization to calculate $\mathbf{K}$. We perform least-squares fits to calculate the non-Darcy parameters that best fit the data over the whole range of Reynolds numbers. Then, we can parametrize C_d using Darcy and non-Darcy laws.

3.4.2 Domains and Boundary Conditions

For simplicity, for 2D computations we use a 1 m $\times$ 1 m box for the porous periodic cell as seen in Figure 3.1. For 3D, we utilize 2 types of domains that are both 1 m $\times$ 1 m $\times$ 1 m cubes as seen in Figure 3.2. For our 3D simulations we assume periodicity in the 2 horizontal directions. The first 3D domain contains a cylindrical obstacle penetrating the entire domain. This will be used to simulate "emergent vegetation": vegetation that rises above the water level. The second 3D domain seen in Figure 3.2 contains a conical obstacle which does not reach the top of the domain. This models "submerged vegetation," that which lies completely below the water level. We call the re-

Simulation type	Obstacle Diameter(m)	Number of Elements
2D Porous Media	0.5	4014
2D Porous Media	0.55	4092
2D Porous Media	0.6	3934
2D Porous Media	0.65	3918
3D Emergent Cylinder	0.6	259,151
3D Emergent Cylinder	0.7	219,923
3D Submerged Cone	0.35	339,432

Table 3.1: Number of elements for all simulations.

gion of the cell containing the fluid Ω. The boundary of Ω, Γ, can be separated as $\Gamma = \Gamma_{periodic} \cup \Gamma_{top} \cup \Gamma_{bottom} \cup \Gamma_{obs}$ where $\Gamma_{periodic}$ contains the front, back, left, and right faces of the cubic domain. No-slip boundary conditions are imposed on $\Gamma_{obs} \cup \Gamma_{bottom}$, periodic boundary conditions are imposed on $\Gamma_{periodic}$ and a free surface boundary condition is imposed on Γ_{top}.

3.4.3 Numerical Method

We use a locally conservative, stabilized finite element method, outlined in [47] and Chapter 2, to find weak solutions to (3.17) and (3.25) with zero initial conditions for pressure and velocity. For higher Re cases we use implicit time stepping until the mean velocities reach a stationary state. We utilize linear Lagrangian basis functions on unstructured triangular and tetrahedral meshes. Table 3.1 gives the number of elements for each simulation. When we include the time derivative, we convert the initial-boundary value problem into a sequence of boundary value problems. All simulations were run in parallel on Texas Advanced Computing Center (TACC) machines.

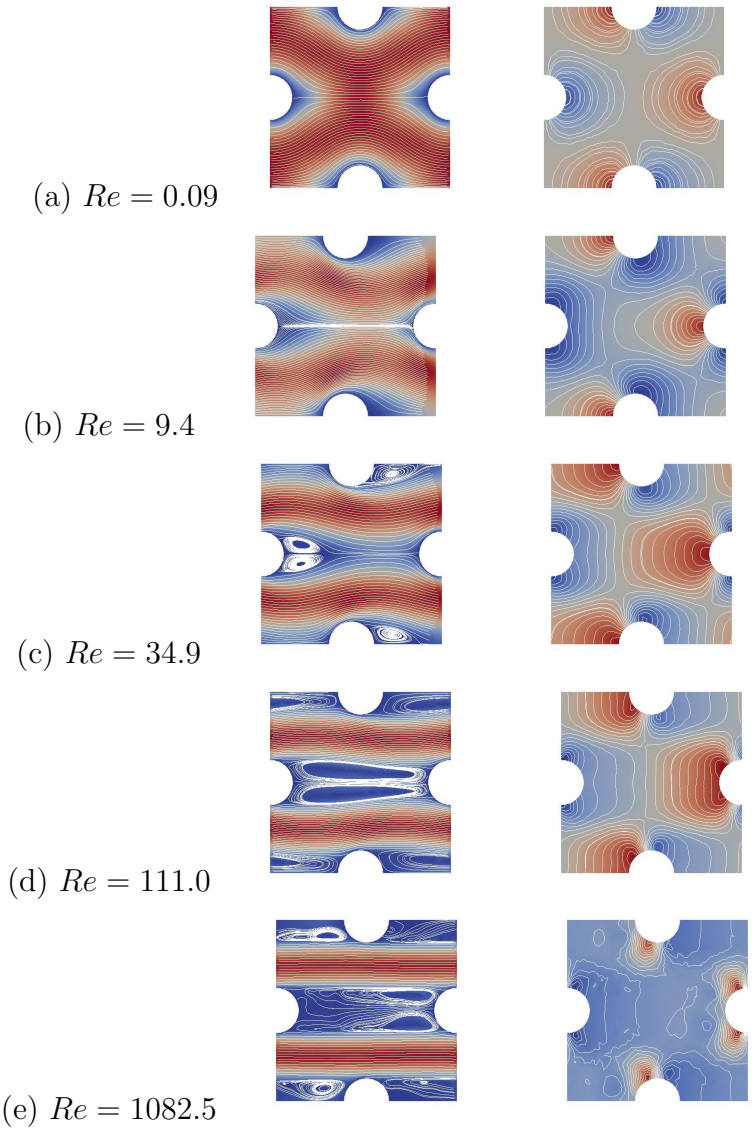

Figure 3.3: Streamlines (left) and pressure contours (right) for instantaneous snapshots of flows of various Reynolds numbers in 2D porous media domain with circle diameter 0.25 m. Streamline plots have background coloring showing velocity magnitude and pressure contour plots have background coloring showing pressure. Red coloring means higher values and blue means smaller.

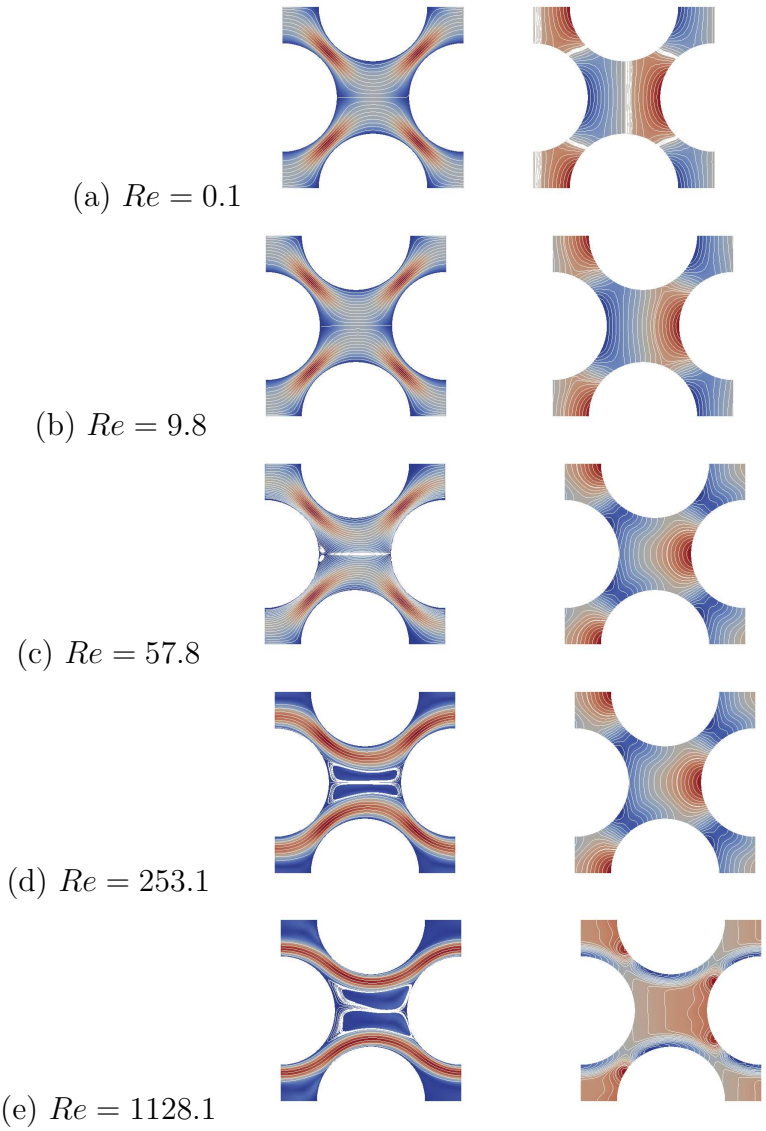

(a) $Re = 0.1$

(b) $Re = 9.8$

(c) $Re = 57.8$

(d) $Re = 253.1$

(e) $Re = 1128.1$

Figure 3.4: Streamlines (left) and pressure contours (right) for instantaneous snapshots of flows of various Reynolds numbers in 2D porous media domain with circle diameter 0.6 m. Streamline plots have background coloring showing velocity magnitude and pressure contour plots have background coloring showing pressure. Red coloring means higher values and blue means smaller.

3.5 Results

Our analyses involve the change in behavior of flow over a range of Reynolds numbers. We take as our "true" values the results of solving (3.25). For simplicity, we assume $\rho = 1$ kg/m^3 and $\nu = 1$ m^2/s. This is acceptable because we use the non-dimensional Reynolds number as our main variable representing flow speed. The filter size Δ_g is taken as the diameter of the cell. The flows are driven by the forcing term $\mathbf{f}$ in (3.25). We then recover velocity fields and pressure values.

3.5.1 Qualitative Analysis of Drag

The nature of the flow and drag change as Reynolds number increases. We solve (3.25) driven by a range of forcing values $\mathbf{f}$. In Figure 3.3 and Figure 3.4 we show streamlines and pressure contours for 2D flows with obstacles of diameter 0.25 m and 0.6 m respectively. These domains are our standard porous media domains of arrays of circles.

In Figure 3.3 (a) with $Re = 0.09$ we see Stokes flow. The flow is almost completely dominated by viscous forces. We see the viscous effects extending far into the surrounding fluid. Notice that the streamlines are deformed throughout the entire flow. This is the "deformation drag" discussed in Section 2.1. The pressure field is completely symmetric. The increase in pressure on the front of the obstacles is equal and in the same pattern as the decrease in pressure on the back side. We expect this for Stokes flow. In (b) with $Re = 9.4$, we see that while there is still a fair amount of deformation to the

flow, there is much less than in (a). This signifies that the flow is no longer dominated by viscous forces. There are now nonlinear inertial effects. Since flow separation is not occurring here this is considered to be "surface drag." The pressure contour patterns are no longer symmetric. In (c) with $Re = 34.9$, we see that laminar recirculation has started behind the obstacles. Note that they are not turbulent eddies, as turbulence does not occur at this Reynolds number. There is very little deformation to the drag in the region between the obstacles. The drag that we see here is "form drag." In (d), with $Re = 110.0$ we see that the recirculation regions have grown greatly in size, as we expect. There is even less flow deformation due to the obstacles. This flow has some turbulence, but not enough to have significant effects on the flow pattern. In (e) with $Re = 1082.5$, we see fully turbulent flow. There is no steady-state flow pattern. The obstacles cause almost no deformation in the flow pattern.

In Figure 3.4 we see results for a domain with circles of diameter 0.6 m. Qualitatively, these results are quite similar to those for the previous domain. Because of the much smaller porosity; however, we see that the deformation in the flow remains for higher Re. Also notice the difference in the pattern of the pressure contours as compared to the previous example. In the more densely packed domain, the pressure contours go between separate obstacles, and they do not in the less tightly packed domain. This result is similar to the results from Koch and Ladd [50] and demonstrates that the tightness of particle packing has a substantial effect on important flow characteristics.

Circle Diameter(m)	Separation(m)	$\mathbf{K}(m^2)$
0.65	0.35	0.00008548
0.6	0.4	0.0004262
0.55	0.45	0.001148
0.5	0.5	0.002362
0.45	0.55	0.004175
0.4	0.6	0.006701
0.35	0.65	0.01007
0.3	0.7	0.01449
0.25	0.75	0.02024

Table 3.2: Values for hydraulic conductivity **K** for Porous Media Cells of Various Diameters

3.5.2 Homogenization and Darcy's Law

We calculated hydraulic conductivities **K** by solving (3.17) on various domains. We use a highly refined mesh with $h = 1/120$ m where h is the maximum element edge length. For our standard porous media domain(as seen in Figures 3.3 and 3.4) with varying diameters of circles we show the values of **K** in Table 3.2. Graphically, we show this in Figure 3.5.

In Figure 3.6 we see, as we expect, that Darcy's Law using the **K** calculated from homogenization is valid for small Reynolds numbers (< 0.25). Above this range, we see inertial effects having a major effect on the flow. Obviously, Darcy's Law is an unreasonable assumption for higher velocity flow, the type we might observe in flow through vegetation. We therefore investigate the non-Darcy models mentioned above.

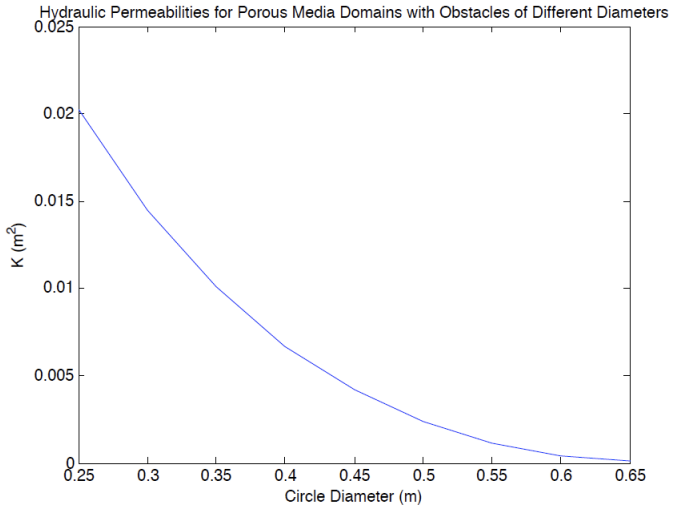

Figure 3.5: Values for hydraulic conductivity **K** for porous media cells of various diameters.

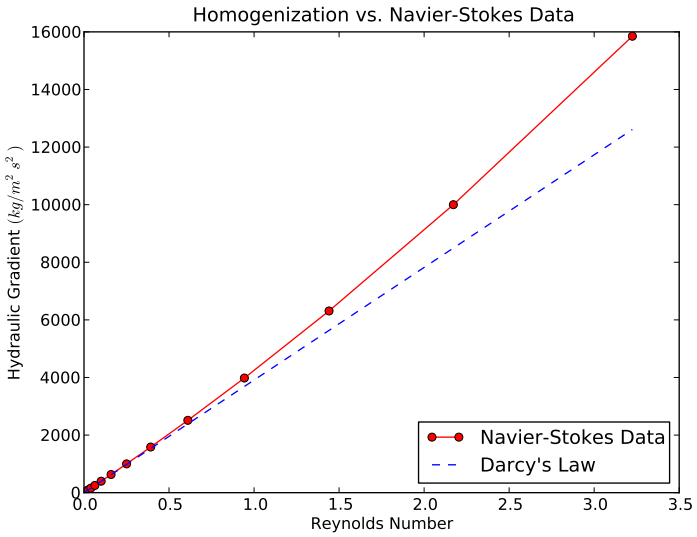

Figure 3.6: A comparison of Darcy's law with computationally calculated **K** and Navier-Stokes data.

3.5.3 Analysis of Non-Darcy Laws

We compare our Navier-Stokes data with the Darcy and non-Darcy laws introduced earlier. After performing Navier-Stokes simulations over a range of forcing terms $\mathbf{f}$, we have a collection of data from which to fit parameters for the non-Darcy models mentioned previously. These fitted parameters change drastically depending on the range of Reynolds numbers over which the fit is performed. The following calculations were performed on our standard porous media 2D domain with circles of diameter 0.6 m.

Figure 3.7 (a) shows how β from the Darcy-Forchheimer equation calculated from least squares fitting changes depending on the range over which the fit is done. Ideally, we could perform this fit for low Reynolds number flow and it would remain valid for higher Reynolds number flow; however, these results show that β changes as the range of Reynolds numbers for fitting is increased. Figure 3.7(b) shows the Forchheimer parameter β over a range of values from $Re = 1$, $Re = 10$, and $Re = 100$ compared to the Navier-Stokes data. The two fits over the low ranges diverge significantly from the Navier-Stokes data at high Re.

The results from fitting the cubic non-Darcy equation are in Figure 3.8. The coefficient of the cubic term varies greatly depending on the range of Reynolds numbers over which the fitting is performed. Notice that these plots vary so greatly over the given range of Reynolds numbers that the y-axis must be shown on a logarithmic scale. This shows that for higher Re the cubic law is not valid. For low Reynolds numbers, it does fit the data rather well,

validating some of the homogenization theory by Mei and Auriault [67] and Rasoloarijaona and Auriault [83].

The power law non-Darcy equation fit results are shown in Figure 3.9; (a) shows how the coefficient β_α changes depending on the range of Re over which the fit is performed; (b) similarly shows this for the power α. Both of these plots flatten out at higher Re, with $\beta_\alpha \approx 145$ and $\alpha \approx 1.87$. The results from the lower Re fits do a reasonable job at matching Navier-Stokes data. Figure 3.9 (c) shows that the parameter fits up to $Re = 10$ and $Re = 100$ match extremely well with the Navier-Stokes data.

These non-Darcy models historically are based on empirical results with data from relatively low Reynolds number flows ($Re < 10$). Our results show that they all do a reasonable job at matching the Navier-Stokes data in this low Re range; however, parameters estimated on low Re data do not sufficiently model higher Re behavior. From our fits we see that if the parameters are calculated using a larger range of Reynolds number, that they adequately fit for higher Re behavior as well as lower.

3.5.4 C_d and Higher Reynolds Number Flows

The Navier-Stokes data can also be used to analyze the drag coefficient C_d. Figure 3.10 shows C_d calculated using (3.2) on the standard 2D porous media domain for a variety of diameters. This result resembles a Moody diagram in pipe flow. It shows linear behavior (as previously shown) in the low Re ranges and approaches a constant at high Re as theory suggests should

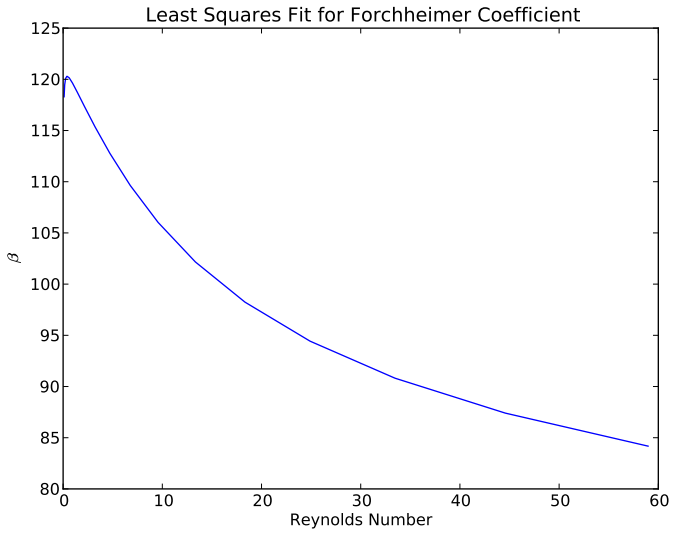

(a) Changes in Forchheimer coefficient for Darcy-Forchheimer equation from least squares fit.

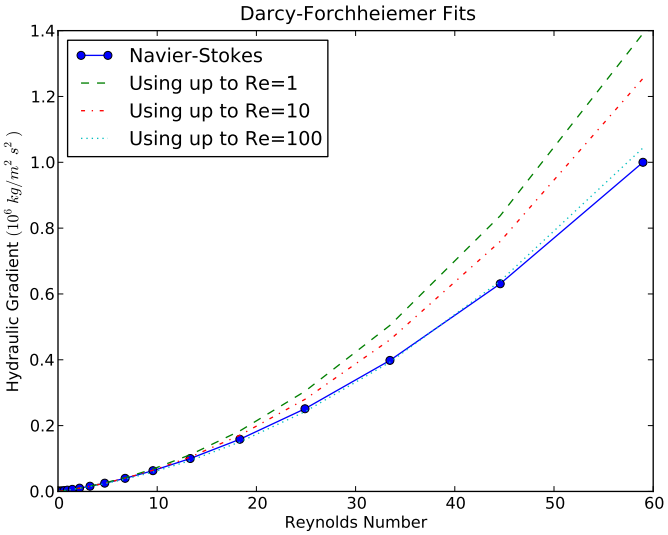

(b) Darcy-Forchheimer plot using parameter fit over different ranges of Re.

Figure 3.7: Darcy-Forchheimer fit results.

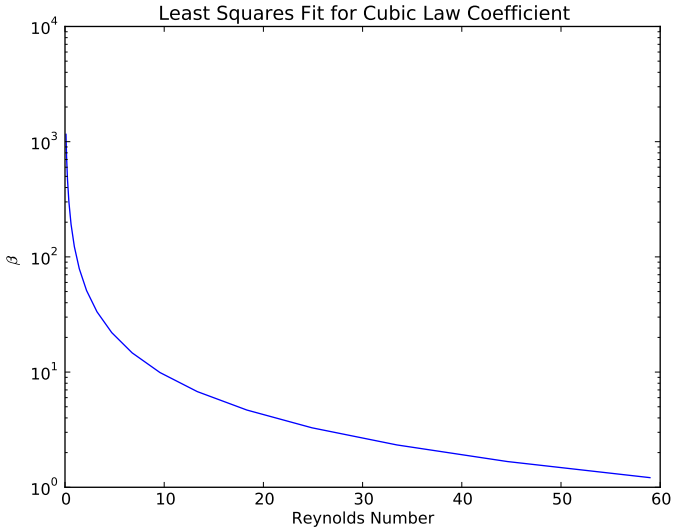

(a) Changes in cubic coefficient for cubic equation from least squares fit.

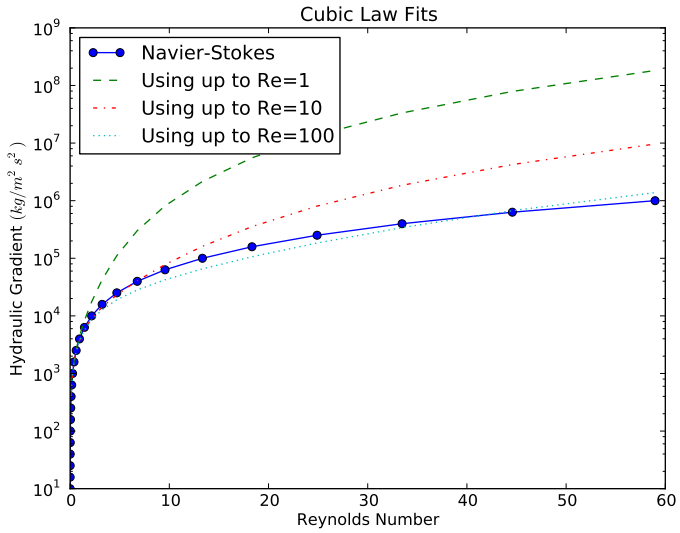

(b) Cubic law plot using parameter fit over different ranges of Re.

Figure 3.8: Cubic law fit results.

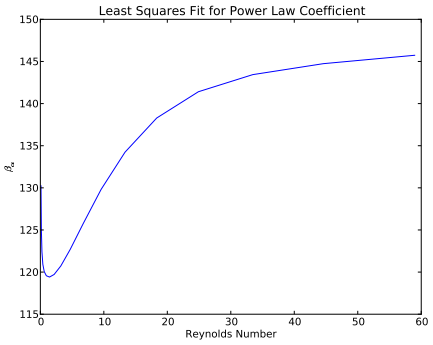

(a) Changes in power term coefficient for power equation from least squares fit.

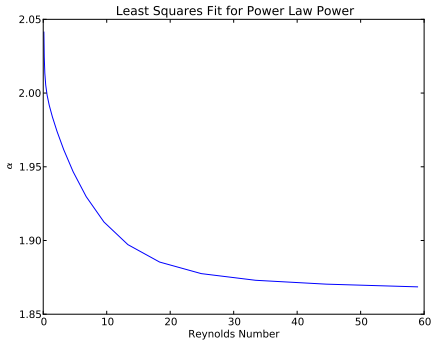

(b) Changes in power for power equation from least squares fit.

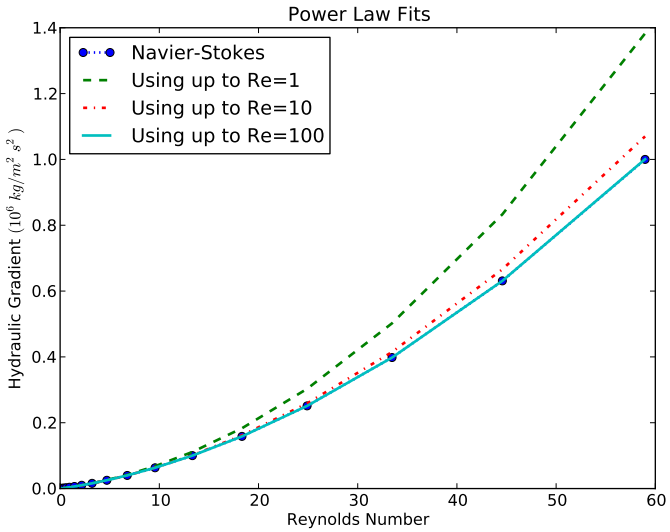

(c) Power law plot using parameter fit over different ranges of Re.

Figure 3.9: Power law fit results.

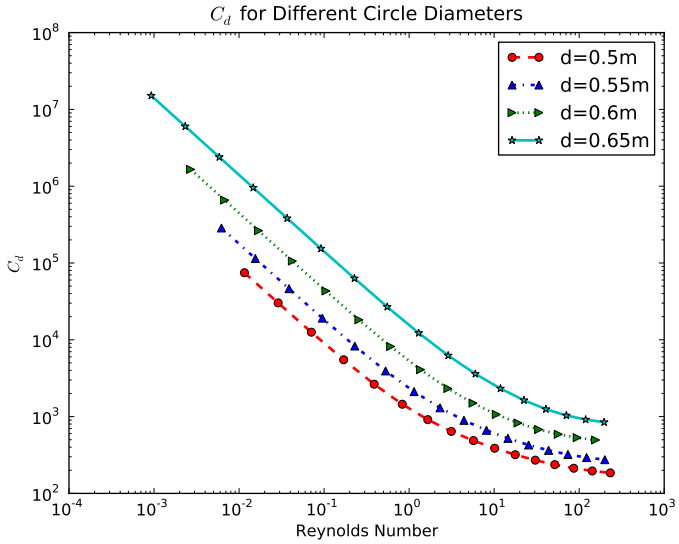

Figure 3.10: Drag coefficients for 2D porous media domains with circles of varying diameter.

happen. The behavior between these regions is interesting and requires more study.

It is important to show that our numerical method converges with spatial refinement. Figure 3.11 shows C_d calculated for $d = 0.6$ m at high Re for 3 mesh sizes. This plot qualitatively shows that our calculated values of C_d for high Re do converge with refinement.

3.5.5 3D Emergent Cylinder Problem

The three-dimensionality of vegetation has a major effect on flow behavior. Flow behaves differently depending on whether or not the vegetation is completely submerged or whether it rises above the fluid level. If it is com-

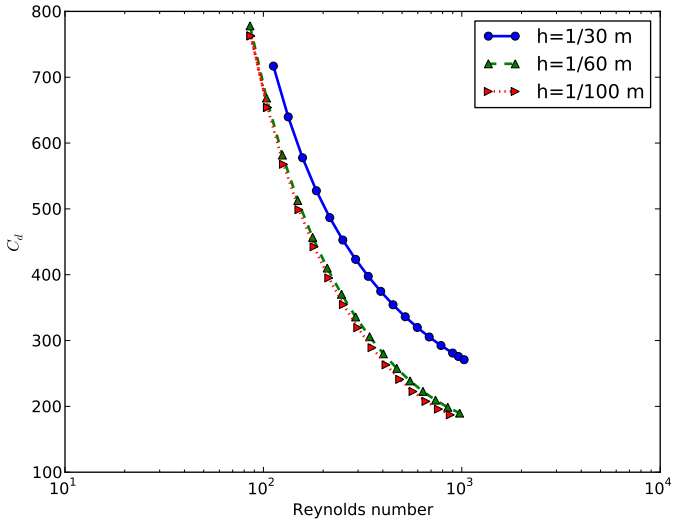

Figure 3.11: Convergence of high Reynolds number drag coefficients with different mesh sizes h for 2D domain with $d = 0.6$ m.

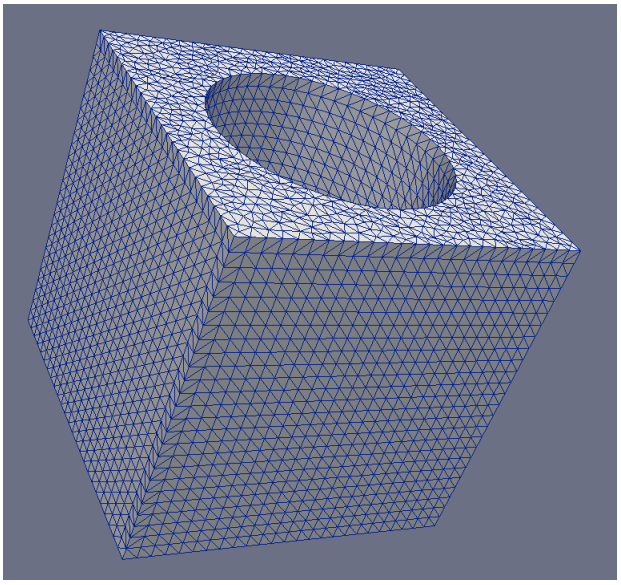

Figure 3.12: Surface of mesh used for 3D calculations.

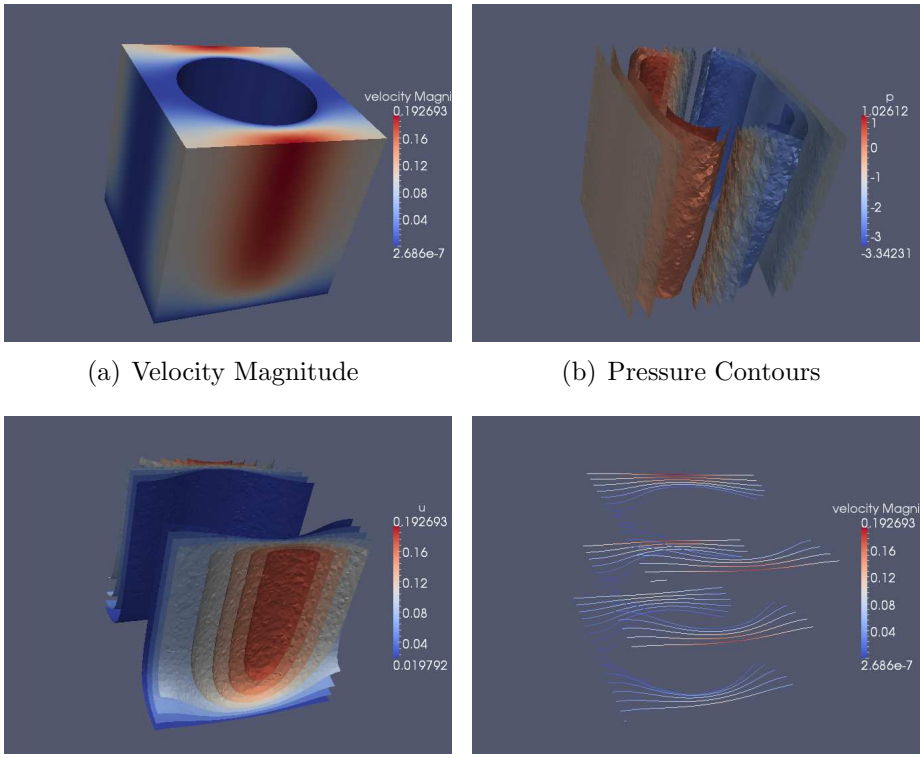

(a) Velocity Magnitude

(b) Pressure Contours

(c) u Velocity Contours

(d) Streamlines

Figure 3.13: Emergent Cylinder $Re = 0.025$.

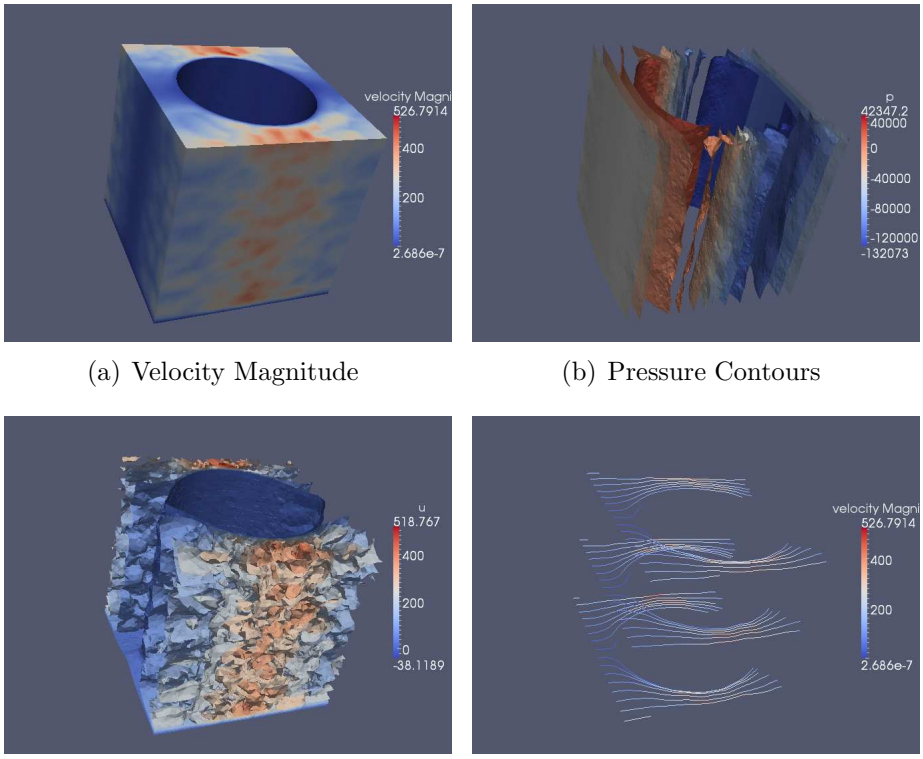

(a) Velocity Magnitude

(b) Pressure Contours

(c) u Velocity Contours

(d) Streamlines

Figure 3.14: Emergent Cylinder at $Re = 60.15$.

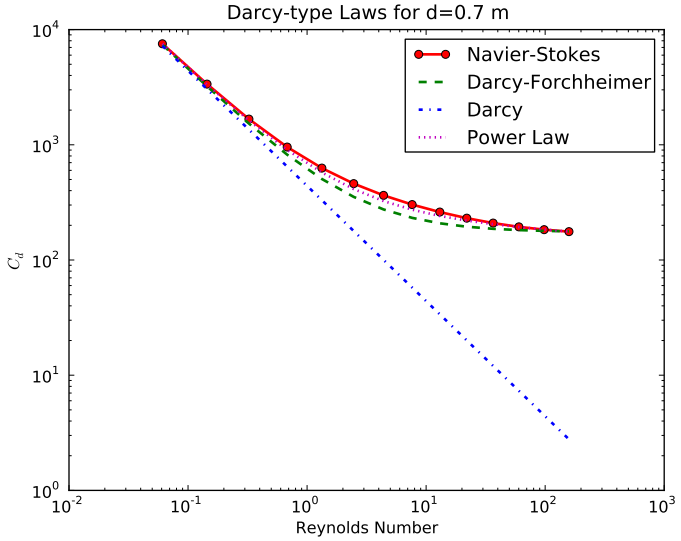

Figure 3.15: Darcy and non-Darcy upscaling results for 3D flow around a cylinder of diameter 0.7 m.

pletely submerged, then the flow height is important. The bed also has a major effect on the flow.

We consider a cubic domain with a cylindrical obstacle as seen in Figure 3.2. Figure 3.12 shows an example of a tetrahedral mesh on this domain. We incorporate the horizontal periodic boundary conditions as described in Section 3.3. Figures 3.13 and 3.14 show velocity, pressure contours, u velocity contours, and streamlines for flows with $Re = 0.025$ and $Re = 60.15$ respectively. In Figure 3.13 we see deformation drag, just as we had seen in 2D. In Figure 3.14, we qualitatively see surface drag.

We also consider Darcy and non-Darcy models for our 3D results. In the

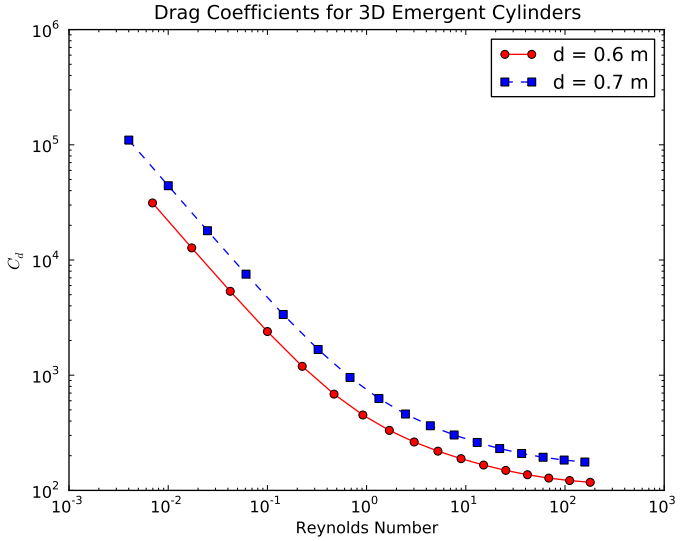

Figure 3.16: C_d over a range of Re for flow around 3D cylinders of different diameters.

same way that we did for the 2D results, we calculate $\mathbf{K}$ using mathematical homogenization and perform parameter fitting to estimate parameters for non-Darcy laws. We use data from the full range of Reynolds numbers to fit for the parameters necessary for the non-Darcy laws. The resulting drag coefficients C_d for flow around a cylinder of diameter 0.7 m using these upscaling models over a range of Re are shown in Figure 3.15. C_d over a large range of Re for different diameter cylinders is shown in Figure 3.16. These results are qualitatively similar to the results of our 2D analyses. We should note that at these drag coefficients are substantially different in magnitude, but not in dynamics, from the 2D results at low Re; however, those domains are much less porous due to their tight packing, causing a lower theoretical hydraulic

conductivity. Darcy's Law is valid for very small Re (< 1), as we saw in 2D. The Darcy-Forchheimer equation and the power law (3.9) match the Navier-Stokes data quite well over the whole range of Re.

These 3D simulations are much more computationally expensive than their 2D counterparts. That they provide similar results to the 2D simulations gives credence to their accuracy.

3.5.6 3D Submerged Cone Problem

This simulation is most like a real world flow over submerged vegetation. The problem uses the submerged cone domain in Figure 3.2. It models the behavior of flow through a periodic bed of completely submerged plants. The 3D behavior of this flow is much more complex than that in the previous example. There are nontrivial vertical velocities in sections of the domain. By driving flow with range of hydraulic gradients $\mathbf{F}$ to steady-state we see the flow structure and upscaled results for a variety of Reynolds numbers. The cones in these simulations have a height of 0.8 m and base radius of 0.25 m and are located in the center of the cell. For our scaling parameter d we use 0.35 m, the diameter at the center of mass.

Figure 3.17 shows results from a low Reynolds number flow with $Re = 0.014$. The length scale used to calculate Re is the diameter of the base of the cone which is 0.4 m in this case. Notice the 3D behavior in the streamlines. There is vast flow deformation in the horizontal and vertical directions around and over the cone. In the vertical slice, we see a thick boundary layer around

the bottom and the cone with a gradual increase in velocity. As we have seen in other 2D and 3D examples, there is high pressure upstream of the obstacle and low pressure downstream. Figure 3.18 shows the same results for a flow with $Re = 6.3$. In this instance the deformation is less prominent farther away from the cone but very drastic near the cone. We see a much smaller boundary layer near the bottom and near the cone. Above this, we see a standard logarithmic velocity profile. This displays the effects of form drag in the vertical direction.

As with other 2D and 3D problems done here, we look at Darcy and non-Darcy upscaling results. In Figure 3.19 we see similar results to the 2D problems and the 3D cylinder problem. At low Re Darcy's Law and Darcy-Forchheimer match very well with Navier-Stokes data. At higher Re, Darcy's Law become completely invalid and Darcy-Forchheimer and a power law provide reasonable approximations for C_d. The full range of simulations were used to fit for the various non-Darcy model parameters.

3.6 Conclusions

Flow through porous structures and vegetated domains can be quite complex. For very low Re flows Darcy's Law accurately and effectively models the mean flow. Using mathematical homogenization, the resulting hydraulic conductivities can be relatively easily calculated. However, for higher Re flow, it is not as simple. Non-Darcy models such as Darcy-Forchheimer provide more accurate results than Darcy's Law; however, they require important parame-

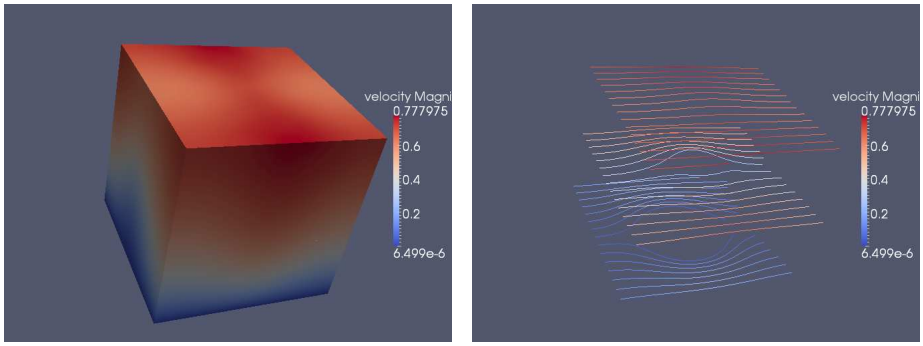

(a) Velocity Magnitude (b) Streamlines

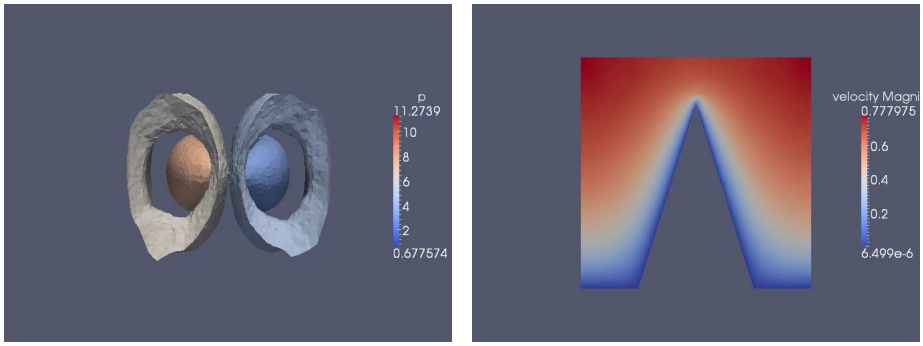

(c) Pressure Contours(bottom view) (d) Velocity in Vertical Slice

Figure 3.17: Flow characteristics for flow around a submerged cone of base diameter of 0.5 m and a height of 0.8 m at $Re = 0.014$.

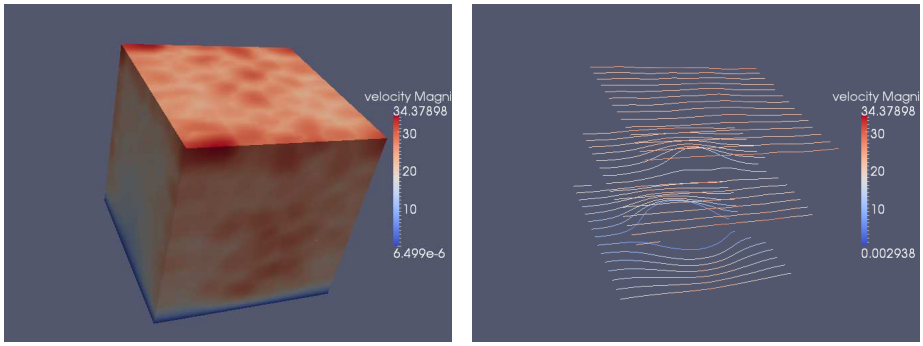

(a) Velocity Magnitude (b) Streamlines

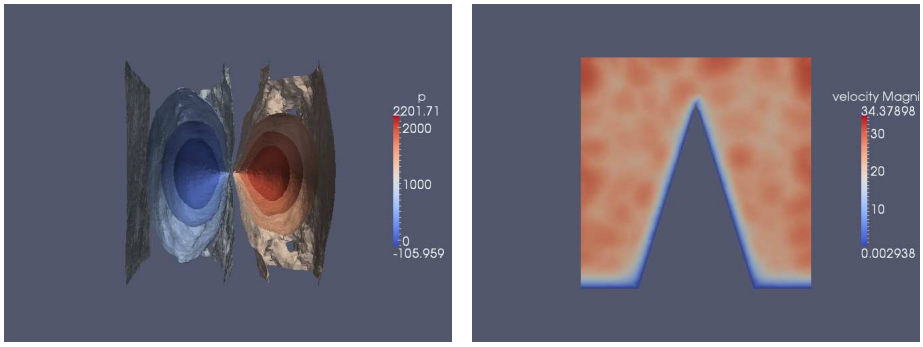

(c) Pressure Contours(bottom view) (d) Velocity in Vertical Slice

Figure 3.18: Flow characteristics for flow around a submerged cone of base diameter of 0.5 m and a height of 0.8 m at $Re = 6.3$.

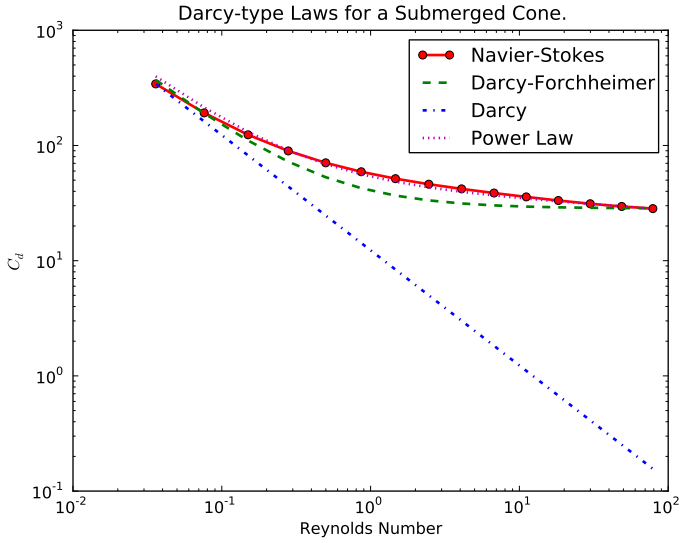

Figure 3.19: Darcy and non-Darcy upscaling results for 3D flow around a submerged cone with base diameter 0.5 m and a height of 0.8 m.

ters to be estimated and are not effective over large ranges of Re. The most descriptive way of displaying the drag effects on these types of domains over a large range of Re is a chart similar to a Moody diagram. Creating this would require performing extensive computational simulations over many different packings of vegetation and many Reynolds numbers. This approach might allow for a semi-automated system for taking remotely sensed geometry information (i.e. using LiDAR) and calculating parametrized resistance factors. Further work remains for issues such as depth dependance with submerged vegetation, flexible stems, foliage, and potential issues like wave/current/vegetation interaction. Once adequate drag analyses are performed, the upscaled results could be used to model flow through large, complex vegetated domains without having to capture the fine details of the domain, providing acceptable estimations of flow characteristics while being computationally viable.

Chapter 4

Immersed Structure Approach

4.1 Introduction

The work presented in the previous chapter describes a novel method for parameterizing drag for flow through a relatively simple domain containing relatively few rigid obstacles. For larger scale problems, it becomes computationally unreasonable to resolve all of the complex geometry of a bed of vegetation. The level of mesh refinement necessary to accurately resolve on a single mesh thousands or even hundreds of pieces of vegetation would push the limits of current computational capabilities. Also, as mentioned previously, plant flexibility is often an important factor in the amount of resistance to flow due to vegetation. To incorporate plant flexibility into the single-mesh method introduced in the previous chapter would require moving meshes and 3D structure models to model the elastic motion of the vegetation. This would require a 3D single-mesh fluid-structure interaction (FSI) method that would be prohibitively computationally expensive and possibly impossible to implement at the scale that we require. Instead, in this chapter we present an immersed structure approach to modeling flow over larger-scale, more complex, rigid and flexible beds of vegetation.

4.1.1 Bulk Drag

In Section 3.2, we gave a general overview of the concept of drag and important concepts like the drag equation, the drag coefficient, and how it changes as Reynolds number changes. The drag formulation described there is for ideal flow conditions. For a larger-scale vegetated channel, the drag depends on free-surface effects, turbulence, and complex velocity profiles. These effects are described in detail by Petryk [79]. Also, the effect of nearby vegetative obstacles affects the drag pieces of vegetation. As described by Nepf [73], for a vegetated channel, drag force per unit fluid volume is defined by the bulk drag equation

$$F_{drag} = \frac{1}{2}\rho \tilde{C}_d a U^2 \tag{4.1}$$

where $\tilde{C}_d$ is a non-dimensional bulk drag coefficient, ρ is the fluid density, U is the mean velocity, and a is the projected plant area per unit volume, the so-called vegetation population density. Modeling the plants as cylinders, a is defined as

$$a = N_v b = \frac{bH}{(\Delta S)^2 H} = \frac{b}{(\Delta S)^2} \tag{4.2}$$

where N_v is the number of plants per unit horizontal area, b is the mean cylinder diameter, and ΔS is the mean spacing between plants, and H is the channel depth.

Whereas for a single obstacle element, the drag coefficient C_d is only a function of obstacle shape and Reynolds number, the bulk drag drag coefficient is also a function of population density. The effect of population density

can even be observed among a pair of cylinders with one situated downstream from the other. Early reviews of interference between two cylinders in different arrangements were done by Zdravkovich [116] and Zdravkovich and Pridden [118] using wind tunnel experiments. It has been observed that the wake caused by the upstream cylinder decreases the drag coefficient for the downstream cylinder. This has been shown for semi-infinite cylinders by Bokaian and Geoola [8] and Blevins [7] and for finite-length cylinders by Luo et al. [64]. This decrease in drag coefficient is caused by two factors of the wake. The first factor is that the downstream cylinder experiences lower fluid velocity due to the drag of the upstream cylinder. The second factor is that the wake of the upstream cylinder results in lower pressure differential around the downstream cylinder according to Zukausras [119] and Luo et al. [64]. The decrease in downstream drag is called the "sheltering effect" by Raupach [84].

There is a long history of attempts at calculating the bulk drag coefficient for vegetated channels. Li and Shen [56] analyzed the experimental results from rigid cylinders due to Petryk [79] using a wake superposition model. They found that further downstream in the array of cylinders that the bulk drag coefficient asymptotically approached a value between 1.1 and 1.2 at a Reynolds number of 9×10^3 and that it generally slightly decreased with greater spacing between the cylinders. Klaassen and Van Der Zwaard [48] calculated the bulk drag coefficient using a Chezy formula to analyze data for air flow though canopies of fruit trees. Their estimates for $\tilde{C}_d$ are higher than 1.2, perhaps due to more turbulence in tree canopies than cylinders sub-

merged in water. They also saw the bulk drag coefficient decrease with greater spacing between obstacles. Seginer et al. [94] performed wind tunnel experiments using rigid aluminum cylinders and utilized the horizontal momentum balance equation to estimate the bulk drag coefficient. They concluded that increased obstacle population density increased the turbulence intensity and thus a decrease in drag. These results are in opposition to experimental results by Graf and Ko [33] and the earlier discussed results. The applicability of these findings have been questioned by Dunn et al. [23]. Reid and Whitaker [88] performed experiments with rigid cylindrical obstructions submerged in channels of variable depth. They used Manning's equation to estimate the bulk drag coefficient for different depths, estimating $\tilde{C}_d$ to be 1.77. Burke and Stolzenbach [11], using a RANS-type computational model with a $k-\epsilon$ turbulence model estimated that $\tilde{C}_d = 2.5$ would be appropriate for all velocities for *Spartina* grass in a marsh. They mention the limitations of such a simple model and suggest more research be done in the area. From experiments using flexible plastic cylinders Saowapon and Kouwen [92] estimated the bulk drag coefficient as

$$\tilde{C}_d = 2\sin^3\phi \tag{4.3}$$

where ϕ the the bent angle of the vegetation. This equation which is given by Hoerner [36] obviously returns values between 0 and 2. Den Hartog and Shaw [22] performed experiments over a flexible corn canopy and estimated mean bulk drag coefficients between 0.2 and 0.043. They provide an equation for the vertical profile of $\tilde{C}_d$. These early studies show a wide variation in

calculated values of $\tilde{C}_d$. This is due to the different methods of calculating $\tilde{C}_d$, experimental setups, and measuring devices. While they do not provide concrete values or even ranges of $\tilde{C}_d$ for specific flows, the important consensus that can be drawn from these studies is that $\tilde{C}_d$ generally decreases with greater vegetation spacing.

4.1.2 Experimental Methods for Calculating the Bulk Drag Coefficient

For verifying our methods, we focus on three more recent very well-respected experimental studies. The first is by Dunn et al. [23] in which rigid and flexible cylinders were placed in a flume with a variety of spacings and for a large range of Reynolds numbers. They used acoustic Doppler velocimeters that measure velocity and turbulence characteristics which they used to calculate the bulk drag coefficient. The second study is by Nepf [73] in which wooden cylinders were placed in a variety of arrangements in a flume and acoustic Doppler and laser Doppler velocimeters were used to measure velocities. The horizontal momentum balance is used to calculate $\tilde{C}_d$. The third study is by Wu et al. [115] and uses a laboratory wave tank to measure the wave attenuation by vegetation. They perform experiments with rigid dowels, flexible rubber hoses, and actual marsh grasses.

Using Reynolds averaging, for fully developed uniform shear flow through cylindrical obstructions, Dunn et al. [23] take the horizontal momentum equa-

tion to be

$$\begin{aligned} 0 &= \rho g_x + \frac{\partial}{\partial x}\left(\mu\frac{\partial \overline{u}}{\partial x} - \rho\overline{u'^2}\right) + \frac{\partial}{\partial y}\left(\mu\frac{\partial \overline{u}}{\partial y} - \rho\overline{u'v'}\right) \\ &+ \frac{\partial}{\partial z}\left(\mu\frac{\partial \overline{u}}{\partial z} - \rho\overline{u'w'}\right), \end{aligned} \tag{4.4}$$

where $\bar{\cdot}$ denotes the time-averaged value and $'$ denotes the fluctuating component. The terms $\rho\overline{u'^2}$, $\rho\overline{u'v'}$, and $\rho\overline{u'w'}$ are called the Reynolds stresses. Using the horizontal averaging technique from Raupach and Shaw [86], from the rate of change of the shear stress, we get

$$\frac{d(\overline{u'w'_h})}{dz} = gS - \frac{1}{2}aC'_d\overline{u_h^2} \tag{4.5}$$

where S is the bed slope, u_h and w_h are the velocities averaged in the horizontal plane, and C'_d is the horizontally averaged drag coefficient. Now, solving (4.4) for C'_d, we have

$$C'_d = \frac{gS - \frac{d}{dz}(\overline{u'w'_h})}{a/2\overline{u_h}^2}. \tag{4.6}$$

They calculate two versions of the bulk drag coefficient. One uses the channel depth H as the vertical length scale and one uses the mean vegetation height h_v as the vertical length scale. These bulk drag coefficients are calculated by

$$\tilde{C}_{dH} = \frac{\int_0^H C'_d u_h'^2 dz}{\int_0^H u_h^2 dz} \tag{4.7}$$

and

$$\tilde{C}_{dh_v} = \frac{\int_0^{h_v} C'_d u_h'^2 dz}{\int_0^{h_v} u_h^2 dz}. \tag{4.8}$$

Nepf [73] uses a different horizontal force balance relationship to calculate $\tilde{C}_d$. The equation is

$$(1 - ad)C_B U^2 + \frac{1}{2}\tilde{C}_d ad(\frac{H}{d})U^2 = gh\frac{\partial H}{\partial x} \tag{4.9}$$

where $C_B = 0.001$ is the bed drag coefficient and $\frac{\partial H}{\partial x}$ is the surface slope. The first term on the left hand side is the is bed drag and the second term is the drag contributed by the stems.

Wu et al. [115] calculate the bulk drag coefficient by analyzing the wave attenuation due to vegetative resistance. The theory of dissipation of wave energy due to resistance effects has been developed in detail by Putnam and Johnson [81], Bretschneider and Reid [10], and Sleath [96]. According to Dalrymple et al. [17], assuming linear wave theory, the conservation of wave energy is

$$\frac{\partial(Ec_g)}{\partial x} = -\epsilon_v \tag{4.10}$$

where $E = \frac{1}{2}\rho g A^2$ is the wave energy per unit area, where A is the wave amplitude, c_g is the wave group velocity, and ϵ_v is the dissipation due to the vegetation. Let L be the wavelength, $k = 2\pi/L$ be the wave number, and H be the mean water depth. Dalrymple et al. [17] and Kobayashi et al. [49] express ϵ_v in terms of the drag force from the vegetation:

$$\epsilon_v = \overline{\int_0^{h_v} N_v(F_x u + F_y v + F_z w)dz}, \tag{4.11}$$

where F_x, F_y, F_z are the drag forces in the corresponding directions and the overline denotes time-averaging. Therefore, we have

$$\epsilon_v = \overline{\int_0^{h_v} \frac{1}{2}\tilde{C}_d \rho N_v b \mathbf{v}|\mathbf{v}|dz}. \tag{4.12}$$

Mendez and Losada [68] assume that the wave heights have an invariant Rayleigh distribution and assuming analytical formulas from linear wave theory obtained the formula for wave energy dissipation per unit horizontal area

due to vegetation

$$\epsilon_v = \frac{1}{\sqrt{\pi}}\rho\tilde{C}_d N_v b \left(\frac{gk}{2\omega}\right)^3 \frac{\sinh^3 kh_v + 3\sinh kh_v}{3k\cosh^3 kh} A_{rms}, \tag{4.13}$$

where ω is the wave angular frequency and A_{rms} is the root-mean-squared wave amplitude. For a single wave according to Dalrymple et al. [17] the solution to the wave energy equation (4.10) gives the relationship

$$\frac{A(x)}{A_i} = \frac{1}{1+\alpha x} \tag{4.14}$$

where x is the horizontal coordinate originating at the beginning of the vegetated area, A_i is the incident wave height, $A(x)$ is the wave height at x, and α is a damping factor defined by

$$\alpha = \frac{8}{9\pi}\tilde{C}_d A_i b N_v k \frac{\sinh^3 kh_v + 3\sinh kh_v}{(\sinh 2kh + 2kh)\sinh kh} \tag{4.15}$$

where $a = h_v/H$ for submerged vegetation and $a = 1$ for emergent vegetation. Similarly, due to Mendez and Losada [68], for irregular waves

$$\frac{A_{rms}(x)}{A_{rmsi}} = \frac{1}{1+\tilde{\alpha}x} \tag{4.16}$$

where

$$\tilde{\alpha} = \frac{2}{3\sqrt{\pi}}\tilde{C}_d A_{rmsi} b N_v k \frac{\sinh^3 kh_v + 3\sinh kh_v}{(\sinh 2kh + 2kh)\sinh kh}. \tag{4.17}$$

Hence, by measuring the incident wave heights and wave heights at various locations within a vegetated area, the bulk drag coefficient may be calculated since all other values are known in the previous equations.

4.1.3 Previous Computational Models For Flexible Vegetation

The common approach for computationally modeling flexible vegetation is by treating a piece of vegetation as a flexible cantilever beam. Kutija and Hong [53] first proposed this method using standard Timoshenko [102] beam theory. Saowapon and Kouwen [92] developed a similar model. Darby [18] describes a one-dimensional model that may be used for both flexible and rigid vegetation. Erduran and Kutija [25] extend the work of Kutija and Hong [53] by using a 3D RANS technique with a combination of mixing length and eddy viscosity closure schemes. They propose quasi-3D coupling with the shallow water equations. Ikeda et al. [40] use cantilever beam theory and 2D LES to model "monami," the waving of flexible plants due to large eddies caused by instabilities in the flow field. They utilize a separate vegetation grid to track the movement of each piece of vegetation. Monami is explained and modeled in depth by Nepf and Ghialberti [72]. Velasco et al. [106] use classical beam theory to compute the displacement of flexible beams under small to moderate deflection. Kubrak et al. [52] extend the method developed by Kutija and Hong [53] for large deflections. Li an Xie [54] build off work involving stiff vegetation by Li and Zeng [55], add a thin plate of "foliage" to the stems and use a 3D LES scheme with a Smagorinsky closure model. They do not completely couple these models. Instead, they used a finite difference method developed by Al-Sadder and Al-Rawi [1] to solve the beam equation for a large variety of inflow velocities and performed a parameterization for the bent stem height based on flow velocity.

All of the above methods only consider planar bending; however in a flow with large velocity or a great deal of directional change or turbulence, we would not expect planar bending. Also, most of these models do not appropriately handle large deflections and are only valid for small deflections. They also tend to not be tightly coupled with the flow solver. We want to develop a method using cantilever beam theory to model flexible vegetation that is as robust and accurate as possible but is not overly computationally expensive.

4.2 Elastic Cantilever Beam Theory

4.2.1 Description of Problem

We model flexible vegetation as inextensible cantilever beams, beams that are anchored on exactly one end. Most theory for elastic cantilever beams is only valid for small deflections; however, the deflection of vegetation due to the force of a fluid flow is usually relatively large. Therefore, we must rely on more general beam theory which is valid for large deflections. The classical theory of the elastica is described by Love [62]. Early analytical and numerical work involving the large deflection of cantilever beams was done by Bisshopp [6]. Deriving from this classical theory Steigmann and Faulkner [97] outline the variational theory for inextensible cantilever beams. This is general theory that is valid for small and large deflections.

We describe the 3D cantilever beam in terms of an arclength parameter $s \in [0, L]$, where L is the length of the beam. We define an orthonormal basis

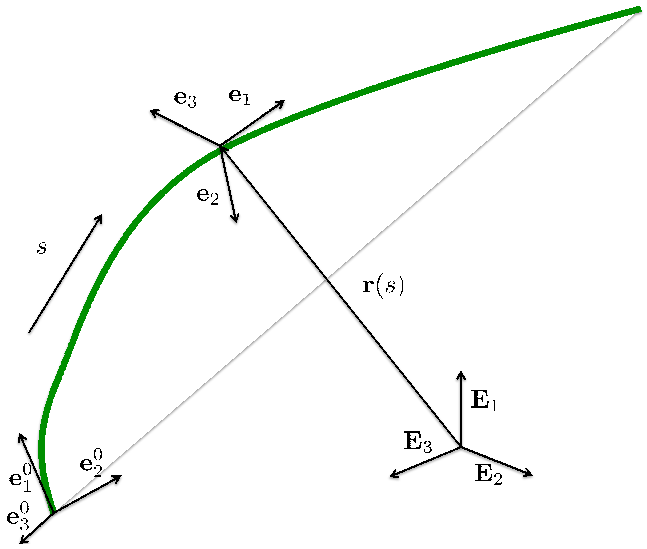

Figure 4.1: An inextensible cantilever beam.

$\{\mathbf{e}_1(s), \mathbf{e}_2(s), \mathbf{e}_3(s)\}$ which describes the orientation of the beam's center-line at s and a vector $\mathbf{r}(s)$ which gives the position of the center-line at s in physical space. $\mathbf{e}_1(s)$ is the unit vector in the direction tangent to the center-line increasing in arclength. $\mathbf{e}_2(s)$ and $\mathbf{e}_3(s)$ span the cross section of the cylinder at s. We refer to $\{\mathbf{e}_i(s)\}$ as the material basis and to $\mathbf{r}(s)$ as the material location. We define a local basis

$$\{\mathbf{e}_i^0\} = \{\mathbf{e}_i\}_{s=0} \tag{4.18}$$

that will serve as a fixed basis along the length of rod. In the undeformed state, $\mathbf{r}(s) = \mathbf{X}(s)$ and $\{\mathbf{e}_i(s)\} = \{\mathbf{E}_i(s)\}$. Let $'$ denote differentiation by s. Since the beam is inextensible, we have

$$\mathbf{r}'(s) \;\; = \;\; \mathbf{e}_1(s), \, \forall s \in [0, L]. \tag{4.19}$$

The given constitutive conditions assure that deformations from the undeformed state to the material state are inextensible and orientation-preserving. We assume that the cross section of the beam at s remains planar, suffers no strain, and is orthogonal to $\mathbf{e}_1(s)$. Since $\{\mathbf{e}_i(s)\}$ and $\{\mathbf{E}_i(s)\}$ are right-handed orthonormal bases, then we can define a rotation transformation

$$\mathbf{R}(s) = \mathbf{e}_j(s) \otimes \mathbf{E}_j(s), \tag{4.20}$$

such that

$$\mathbf{e}_i(s) = \mathbf{R}(s)\mathbf{E}_i(s). \tag{4.21}$$

Let $\kappa_1(s)$ be the twist per unit length, and let $\kappa_2(s)$ and $\kappa_3(s)$ be the curvature about the $\mathbf{e}_1(s)$ and $\mathbf{e}_2(s)$ axes respectively. Let $\boldsymbol{\kappa}(s) = \kappa_1(s)\mathbf{e}_1(s) + \kappa_2(s)\mathbf{e}_2(s) + \kappa_3(s)\mathbf{e}_3(s)$. Then

$$\mathbf{e}_i' = \boldsymbol{\kappa} \times \mathbf{e}_i.$$

Suppose the undeformed configuration has twist and curvatures $\kappa_1^0(s), \kappa_2^0(s)$, and $\kappa_3^0(s)$. Note that these are not necessarily zero. Similarly, we have the relationship

$$\kappa_i = \frac{1}{2}\epsilon_{ijk}\mathbf{e}_k \cdot \mathbf{e}_j', \tag{4.22}$$

where ϵ is the permutation symbol.

Let $W(\boldsymbol{\kappa}, \boldsymbol{\kappa}^0, s)$ be the strain energy per unit arclength as a function of curvatures. Similarly let $U(\mathbf{e}_i, \mathbf{e}_j', s)$ be the strain energy per unit arclength as a function of $\mathbf{e}_i$ and $\mathbf{e}_i'$. It is obvious that we must have $W(\boldsymbol{\kappa}, \boldsymbol{\kappa}^0, s) = U(\mathbf{e}_i, \mathbf{e}_j', s)$.

The strain energy of the system is then

$$S(\mathbf{e}_i) = \int_0^L U ds = \int_0^L W ds. \tag{4.23}$$

Suppose that $\mathbf{f}$ is an end load at $s = L$ and $\mathbf{q}$ is the piecewise continuous distributed load along the arclength of the beam. The potential energy functional of the system is

$$E(\mathbf{r}, \mathbf{e}_i) = S(\mathbf{e}_i) - \int_0^L \mathbf{q} \cdot \mathbf{r} ds - \mathbf{f} \cdot \mathbf{r}(L). \tag{4.24}$$

States $\{\mathbf{r}, \mathbf{e}_i\}$ that minimize E are static states for the cantilever beam under the given loads.

It can be shown using the calculus of variations that the problem of finding stable minima for E is equivalent to solving the Euler-Lagrange equations

$$\mathbf{F}'(s) + \mathbf{q}(s) = 0 \tag{4.25}$$

$$\mathbf{M}'(s) = \mathbf{F}(s) \times \mathbf{e}_1(s) \tag{4.26}$$

with the boundary conditions $\mathbf{F}(L) = \mathbf{f}$ and $\mathbf{M}(L) = 0$, where $\mathbf{M} = \frac{\partial W}{\partial \kappa_i}\mathbf{e}_i$ and $\mathbf{F}$ is a vector of Lagrange multipliers. We notice that these equations are exactly the equations of equilibrium of forces and equilibrium of moments respectively, where $\mathbf{F}$ is the force vector and $\mathbf{M}$ is the vector of moments.

The most important theory for the bending of beams is the Euler-Bernoulli Law, which linearly relates the curvature and twist of the beam to the bending and twisting moments respectively. The Euler-Bernoulli Law is

$$\mathbf{M} = GJ(\kappa_1 - \kappa_1^0)\mathbf{e}_1 + EI_1(\kappa_2 - \kappa_2^0)\mathbf{e}_2 + EI_2(\kappa_3 - \kappa_3^0)\mathbf{e}_3, \tag{4.27}$$

where GJ is called the torsional rigidity and EI_2 and EI_3 are called the flexural rigidities about $\mathbf{e}_2$ and $\mathbf{e}_3$. E is Young's modulus and I_2 and I_2 are the area moments of inertia about $\mathbf{e}_2$ and $\mathbf{e}_1$ respectively. G is the shear modulus and J is the polar second moment of inertia about $\mathbf{e}_1$. Assuming the Euler-Bernoulli Law, we now have the strain energy per arclength as

$$W = \frac{1}{2}\left[GJ(\kappa_1 - \kappa_1^0)^2 + EI_1(\kappa_2 - \kappa_2^0)^2 + EI_2(\kappa_3 - \kappa_3^0)^2\right]. \tag{4.28}$$

We desire to find the material basis and location under a given distributed load. For our purposes, assume that $\mathbf{q}$ is a known function of x, y and z and that $\mathbf{f} = 0$. We describe and analyze a variety of numerical methods for this problem. Some methods involve numerically solving the equilibrium equations (4.25) and (4.26) using the Euler-Bernoulli Law (4.27) as a constitutive equation. Others involve finding a solution that minimizes the potential energy functional (4.24).

4.3 Numerical Techniques

We propose a variety of acceptable techniques for solving the system described in the previous section. All of the previous work discussed in Section 4.1 uses models that are not nearly as general as this. Hence, they tend to be unable to handle large deflections. They also only allow planar bending. We want to allow full 3D bending. Allowing very large deflections and 3D bending will give us as robust a method as is possible.

4.3.1 Nonlinear Finite Element Method

In this method, we use a nonlinear finite element method to find local extrema of the potential energy functional (4.24). A version of this technique for planar bending is presented by Fried [27]. Assume that the distributed load $\mathbf{q} = [q_1, q_2, q_3]^T$ is a known function of spatial coordinates x, y, and z. Assume that there are no end loads. We define three Euler angles θ, ϕ, and ψ such that

$$\frac{r_1'}{L} = \sin\theta\cos\psi, \tag{4.29}$$

$$\frac{r_2'}{L} = \sin\theta\sin\psi, \tag{4.30}$$

$$\frac{r_3'}{L} = \cos\theta \tag{4.31}$$

where $\theta = 0$ corresponds to when the center-line is along the z-axis.

We can write the twist and curvatures in terms of θ, ϕ, and ψ as

$$\kappa_1 = \phi' + \psi'\cos\theta, \tag{4.32}$$

$$\kappa_2 = \theta'\sin\phi - \psi'\sin\theta\cos\phi, \text{ and} \tag{4.33}$$

$$\kappa_3 = \theta'\cos\phi + \psi'\sin\theta\sin\phi. \tag{4.34}$$

Let us assume that the undeformed state has zero curvatures and twist for all s. The potential energy of the system (4.24) becomes

$$\begin{aligned} E(\theta,\phi,\psi) &= \int_0^1 [\frac{1}{2}(GJ(\phi' + \psi'\cos\theta)^2 + EI_1(\theta'\sin\phi - \psi'\sin\theta\cos\phi)^2 \\ &+ EI_2(\theta'\cos\phi + \psi'\sin\theta\sin\phi)^2) - q_1r_1 - q_2r_2 - q_3r_3]ds. \end{aligned} \tag{4.35}$$

Suppose $q_1 = Q_1'$, $q_2 = Q_2'$, $q_3 = Q_3'$, $Q_1(1) = Q_2(1) = Q_3(1) = 0$, and $r_1(0) = r_2(0) = r_3(0) = 0$. Then (4.35) becomes

$$\begin{aligned} E(\theta,\phi,\psi) &= \int_0^1 [\frac{1}{2}(GJ(\phi' + \psi'\cos\theta)^2 + EI_1(\theta'\sin\phi - \psi'\sin\theta\cos\phi)^2 \\ &+ EI_2(\theta'\cos\phi + \psi'\sin\theta\sin\phi)^2) + Q_1\sin\theta\cos\psi \\ &+ Q_2\sin\theta\sin\psi + Q_3\cos\theta]ds. \end{aligned} \tag{4.36}$$

For simplicity, assume that $EI_1 = EI_2 = EI$, which would be the case for a homogeneous, isotropic material with a circular cross section. This gives

$$\begin{aligned} E(\theta,\phi,\psi) &= \int_0^1 [\frac{1}{2}(GJ(\psi'^2(1+\cos^2\theta) + 2\psi'\phi'\cos\theta) + EI(\theta'^2 + \psi'^2\sin^2\theta) \\ &+ Q_1\sin\theta\cos\psi + Q_2\sin\theta\sin\psi + Q_3\cos\theta]ds. \end{aligned} \tag{4.37}$$

Using C^0 quadratic finite elements we calculate the element potential energy E_e. The element has 3 nodes with two on the element boundary and one at the element's midpoint. The reference element is the range $[-1, 1]$, and the shape functions on the reference element are

$$\mathbf{w}^t(\xi) = [\frac{1}{2}\xi(\xi-1), 1-\xi^2, \frac{1}{2}\xi(\xi+1)], \tag{4.38}$$

Interpolation of the Euler angle functions on the element is expressed by

$$\theta = \boldsymbol{\theta_e}^T\mathbf{w},\ \psi = \boldsymbol{\psi_e}^T\mathbf{w}, \text{ and } \phi = \boldsymbol{\phi_e}^T\mathbf{w}, \tag{4.39}$$

where $\boldsymbol{\theta_e}^T = (\theta_1, \theta_2, \theta_3)$ where $\theta_1 = \theta(-1)$, $\theta_2 = \theta(0)$, and $\theta_3 = \theta(1)$, is the element nodal values vector and likewise for ψ and ϕ. Let

$$\boldsymbol{\Phi_e} = [\theta_1, \phi_1, \psi_1, \theta_2, \phi_2, \psi_2, \theta_3, \phi_3, \psi_3]^T \tag{4.40}$$

be the element Euler angle vector.

Let the element size be h, so $ds = \frac{1}{2}hd\xi$, $(\ )' = 2h^{-1}(\dot{\ })$, and $(\dot{\ }) = \frac{d}{d\xi}$. We integrate using 2 point Gauss quadrature with Gauss points, $\zeta_1 = -1/\sqrt{3}$, $\zeta_2 = 1/\sqrt{3}$. Let the index $j = 1, 2$ be such that θ_j is the value of θ at ζ_j, so

$$\theta_j = \boldsymbol{\theta}_e^T \mathbf{w}(\zeta_j),\ \dot{\theta}_j = \boldsymbol{\theta}_e^T \dot{\mathbf{w}}(\zeta_j). \tag{4.41}$$

For brevity define $\mathbf{w}_j = \mathbf{w}(\zeta_j)$ and $\dot{\mathbf{w}}_j = \dot{\mathbf{w}}(\zeta_j)$. The approximate element potential energy functional is now

$$E_e = \frac{1}{h}\sum_{j=1}^{2}[EI(\dot{\theta}_j^2 + \dot{\psi}_j^2 \sin^2\theta_j) + GJ(\dot{\psi}_j^2(1+\cos^2\theta_j) + 2\dot{\psi}_j\dot{\phi}_j\cos\theta_j)]. \tag{4.42}$$

We define the element gradient

$$\mathbf{g}_e = \frac{\partial E_e}{\partial \boldsymbol{\Phi}_e} \tag{4.43}$$

and the element stiffness matrix

$$\mathbf{k}_e = \frac{\partial \mathbf{g}_e}{\partial \boldsymbol{\Phi}_e} = \frac{\partial^2 E_e}{\partial \boldsymbol{\Phi}_e^2}. \tag{4.44}$$

We want to solve the problem $\mathbf{g} = 0$. Our global initial angle vector is $\boldsymbol{\Phi_0}$. Use (4.43) to assemble the initial gradient vector $\mathbf{g}_0$. Delete the entries that correspond to fixed points. Assemble the initial stiffness matrix $\mathbf{K}_0$. Use the Newton-Raphson method

$$\boldsymbol{\Phi_{n+1}} = \boldsymbol{\Phi_n} - \mathbf{K}_n^{-1}\mathbf{g}_n \tag{4.45}$$

until the residual is within a given tolerance. Since this is an optimization problem, we must verify that we are indeed at a minimum. If all of the

eigenvalues for $\mathbf{K}_N$ where N is the terminal Newton iteration are positive, then we are at a local minimum. We can also verify that (4.25) and (4.26) are satisfied.

Since this problem is highly nonlinear, it is possible for the Newton-Raphson method to diverge or never converge if the initial guess is greatly different than the solution. Thus, it is best to use incremental loading if the load is going to cause a large deflection. Results using incremental loading for a variety of uniform distributed loads are shown in Figure 4.2. Notice the 3D behavior of the bending. The loads are greater in the y direction so we see a greater deflection. This is the type of behavior that cannot be captured with planar bending methods.

4.3.2 Linearized Method

Rather than solving the above minimization problem, we have shown above that it is equivalent to solving (4.25) and (4.26), the equilibrium of forces and moments respectively with boundary values $\mathbf{M}(0) = 0$ and $\mathbf{F}(L) = \mathbf{F}$. (4.25) can be solved for $\mathbf{F}$ by simple numerical integration techniques if $\mathbf{q}$ is known.

Assume that the beam's unloaded state is straight, i.e. $\kappa_i^0(s) = 0 \; \forall \; x \in [0, L]$ and that $\mathbf{e}_1^0 = [1, 0, 0]^T$, $\mathbf{e}_2^0 = [0, 1, 0]^T$, and $\mathbf{e}_3^0 = [0, 0, 1]^T$. Let the curvatures be defined as in (4.32,4.33,4.34). Let $\mathbf{\Phi}(s) = [\psi(s), \theta(s), \phi(s)]^T$ and $\mathbf{\Phi}'(s) = [\psi'(s), \theta'(s), \phi'(s)]^T$. The definitions above imply that $\mathbf{\Phi}(0) = 0$.

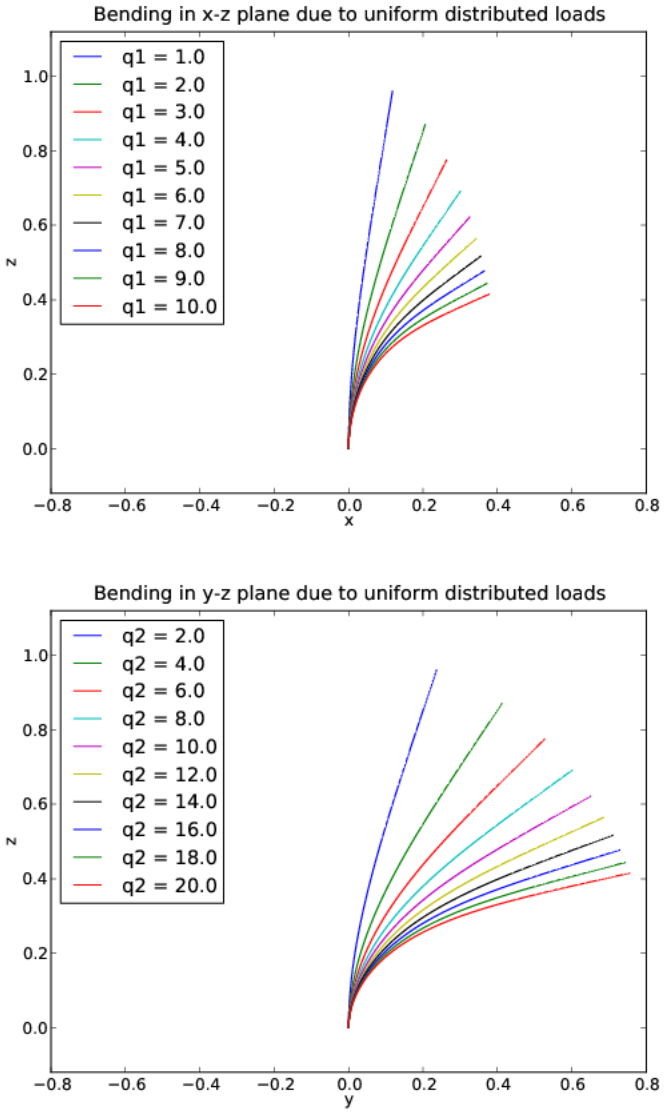

Figure 4.2: Deflections in the x-z and y-z planes due to uniform distributed loads. This has been solved using the nonlinear finite element energy minimization method.

Using (4.27), (4.26) becomes

$$GJ\kappa_1\mathbf{e}_1'+EI_1\kappa_2\mathbf{e}_2'+EI_2\kappa_3\mathbf{e}_3'+GJ\kappa_1\mathbf{e}_1'+EI_1\kappa_2\mathbf{e}_2'+EI_2\kappa_3\mathbf{e}_3' = \mathbf{R}(\mathbf{F}\times\mathbf{e}_1) \quad (4.46)$$

where

$$\mathbf{R} = \begin{bmatrix} \cos\theta\cos\phi & \cos\theta\sin\phi & -\sin\theta \\ \sin\psi\sin\theta\cos\phi - \cos\psi\sin\phi & \sin\psi\sin\ \theta\sin\phi + \cos\psi\cos\phi & \cos\theta\sin\psi \\ \cos\psi\sin\theta\cos\phi + \sin\psi\sin\phi & \cos\psi\sin\theta\sin\phi - \sin\psi\cos\phi & \cos\theta\cos\psi \end{bmatrix} \quad (4.47)$$

is the rotation matrix. $\mathbf{R}$ is orthonormal, so $\mathbf{R}^{-1} = \mathbf{R}^T$. Let

$$\mathbf{E} = \begin{bmatrix} GJ & 0 & 0 \\ 0 & EI_1 & 0 \\ 0 & 0 & EI_2 \end{bmatrix} \quad (4.48)$$

be a diagonal matrix with the stiffness values on the diagonal. Let

$$[H_1, H_2, H_3]^T = \mathbf{R}(\mathbf{F}\times\mathbf{e}_1).$$

(4.46) becomes

$$\mathbf{E}\kappa' = \begin{bmatrix} (EI_1 - EI_2)\,\kappa_2\,\kappa_3 \\ (EI_2 - GJ)\,\kappa_1\,\kappa_3 + H_3 \\ (GJ - EI_1)\,\kappa_1\,\kappa_2 - H_2 \end{bmatrix}. \quad (4.49)$$

Let the right-hand side be known as $\hat{\mathbf{H}}$. Let

$$\mathbf{G} = \begin{bmatrix} 1 & 0 & \sin\theta \\ 0 & \cos\psi & \cos\theta\sin\psi \\ 0 & -\sin\psi & \cos\theta\cos\psi \end{bmatrix}. \quad (4.50)$$

$\det(\mathbf{G}) = \cos\theta$, so $\mathbf{G}$ is invertible if $\theta \neq n\frac{\pi}{2}$ for $n = \pm1, \pm3, \ldots$. Now (4.49) becomes

$$\frac{d}{ds}\mathbf{G}\mathbf{\Phi}' = \mathbf{E}^{-1}\hat{\mathbf{H}}. \quad (4.51)$$

Using the product rule, we have

$$\mathbf{G}\mathbf{\Phi}'' + \mathbf{G}'\mathbf{\Phi}' = \mathbf{E}^{-1}\hat{\mathbf{H}} \tag{4.52}$$

Assuming $\det(\mathbf{G}) \neq 0$, this can be written as

$$\mathbf{\Phi}'' = -\mathbf{G}^{-1}\mathbf{G}'\mathbf{\Phi}' + \mathbf{G}^{-1}\mathbf{E}^{-1}\hat{\mathbf{H}}. \tag{4.53}$$

The condition $\mathbf{M}(L) = 0$ implies $\mathbf{\Phi}'(L) = 0$, so this is a system of second order initial value problems that is solvable with standard techniques such as Runge-Kutta methods. This is discussed by Raboud et al. [82]. This method is fast and accurate for small deformations; however, we are unable to perform incremental loading for the system of ODEs, since it is not an iterative procedure. Since the system is so nonlinear, for good accuracy for problems with large loads, it requires a great deal of segmental steps for an ODE solver. By adding another boundary condition $\mathbf{\Phi}(0) = 0$, which implies that the beam is straight at the base, we get a boundary value problem.

When there are large deflections and we need to use incremental loading to get an accurate result, we can use the finite element method. Define $B = (0, L)$. Let $(\cdot, \cdot)_B$ be the L_2 inner product on B. Let

$$S = \{\mathbf{v} | v_i \in C^1(B) \text{ for } i = 1, 2, 3 \text{ and } \mathbf{v}(0) = 0 \text{ and } \mathbf{v}'(L) = 0\}.$$

Let $W = s$. We call $\mathbf{\Phi} \in S$ a weak solution to (4.53) if

$$(\mathbf{\Phi}'', \mathbf{w})_B = \left(-\mathbf{G}^{-1}\mathbf{G}'\mathbf{\Phi}' + \mathbf{G}^{-1}\mathbf{E}^{-1}\hat{\mathbf{H}}, \mathbf{w}\right)_B \tag{4.54}$$

$\forall \mathbf{w} \in W$. Integrating by parts, we have

$$-\left(\mathbf{\Phi}', \mathbf{w}'\right)_B = \left(-\mathbf{G}^{-1}\mathbf{G}'\mathbf{\Phi}' + \mathbf{G}^{-1}\mathbf{E}^{-1}\hat{\mathbf{H}}, \mathbf{w}\right)_B \tag{4.55}$$

We now linearize this problem so that Picard iteration may be used. Lag the values in the right hand side to solve for the new $\mathbf{\Phi}$.

$$-\left(\mathbf{\Phi}'_{n+1}, \mathbf{w}'\right)_B = \left(-\mathbf{G}_n^{-1}\mathbf{G}'_n\mathbf{\Phi}'_n + \mathbf{G}_n^{-1}\mathbf{E}^{-1}\hat{\mathbf{H}}_n, \mathbf{w}\right)_B \tag{4.56}$$

If the sequence $\{\mathbf{\Phi}_n\} \to \mathbf{\Phi}$ as $n \to \infty$ then $\mathbf{\Phi}$ is a weak solution to the original problem. Suppose that $EI_2 = EI_3 = EI$.

Lemma 4.3.1. *If* $\mathbf{u} \in C^1(B)$, *then*

$$\|\mathbf{u}\|_{L^2(B)} \leq L|\mathbf{u}|_{H^1(B)}. \tag{4.57}$$

Proof. $\mathbf{u}(x) = \int_0^x \mathbf{u}'(s)ds$, so,

$$|\mathbf{u}(s)| = |\int_0^x \mathbf{u}'(s)ds| \leq \int_0^L |\mathbf{u}'(s)|ds.$$

By Cauchy-Schwarz,

$$\int_0^L |\mathbf{u}'(s)|ds \leq \|1\|_{L^2(B)}\|\|\mathbf{u}'\|_{L^2(B)} = L^{1/2}|\mathbf{u}|_{H^1(B)}.$$

Squaring both sides, integrating over B, and taking a square root gives,

$$\|\mathbf{u}\|_{L^2(B)} \leq L|\mathbf{u}|_{H^1(B)}.$$

□

Theorem 4.3.2. *If* $\frac{L^2|\mathbf{F}|}{EI\cos^2\theta}$ *is sufficiently small, the sequence* $\{\mathbf{\Phi}_n\}$ *converges.*

Proof. Define the smooth nonlinear map $\mathbf{h} : (C^1(B))^3 \to (C^0(B))^3$:

$$\mathbf{h}(\mathbf{\Phi}) = -\mathbf{G}(\mathbf{\Phi})^{-1}\mathbf{G}'(\mathbf{\Phi})\mathbf{\Phi}' + \mathbf{G}^{-1}(\mathbf{\Phi})\mathbf{E}^{-1}\hat{\mathbf{H}}(\mathbf{\Phi}). \tag{4.58}$$

Now, (4.56) becomes

$$-\left(\mathbf{\Phi}'_{n+1}, \mathbf{w}'\right)_B = \left(\mathbf{h}(\mathbf{\Phi}_n), \mathbf{w}\right)_B . \tag{4.59}$$

By linearity,

$$-\left(\mathbf{\Phi}'_{n+1} - \mathbf{\Phi}'_n, \mathbf{w}'\right)_B = \left(\mathbf{h}(\mathbf{\Phi}_n) - \mathbf{h}(\mathbf{\Phi}_{n-1}), \mathbf{w}\right)_B .$$

Since $\mathbf{\Phi}_{n+1} - \mathbf{\Phi}_n \in S = W$, let $\mathbf{w} = \mathbf{\Phi}_{n+1} - \mathbf{\Phi}_n$ to get

$$\left(\mathbf{\Phi}'_{n+1} - \mathbf{\Phi}'_n, \mathbf{\Phi}'_{n+1} - \mathbf{\Phi}'_n\right)_B = -\left(\mathbf{h}(\mathbf{\Phi}_n) - \mathbf{h}(\mathbf{\Phi}_{n-1}), \mathbf{\Phi}_{n+1} - \mathbf{\Phi}_n\right)_B .$$

Now,

$$\left(\mathbf{\Phi}'_{n+1} - \mathbf{\Phi}'_n, \mathbf{\Phi}'_{n+1} - \mathbf{\Phi}'_n\right)_B = \left|\mathbf{\Phi}_{n+1} - \mathbf{\Phi}_n\right|^2_{H^1} \geq \frac{1}{L^2} \left\|\mathbf{\Phi}_{n+1} - \mathbf{\Phi}_n\right\|^2_{L^2} ,$$

by Lemma 4.3.1. So now, we have

$$\frac{1}{L^2} \left\|\mathbf{\Phi}_{n+1} - \mathbf{\Phi}_n\right\|^2_{L^2} \leq \left|\left(\mathbf{h}(\mathbf{\Phi}_n) - \mathbf{h}(\mathbf{\Phi}_{n-1}), \mathbf{\Phi}_{n+1} - \mathbf{\Phi}_n\right)_B\right| .$$

By the Cauchy-Schwarz inequality,

$$\left|\left(\mathbf{h}(\mathbf{\Phi}_n) - \mathbf{h}(\mathbf{\Phi}_{n-1}), \mathbf{\Phi}_{n+1} - \mathbf{\Phi}_n\right)_B\right| \leq \left\|\mathbf{h}(\mathbf{\Phi}_n) - \mathbf{h}(\mathbf{\Phi}_{n-1})\right\|_{L^2} \left\|\mathbf{\Phi}_{n+1} - \mathbf{\Phi}_n\right\|_{L^2} ,$$

so now we have

$$\left\|\mathbf{\Phi}_{n+1} - \mathbf{\Phi}_n\right\|_{L^2} \leq L^2 \left\|\mathbf{h}(\mathbf{\Phi}_n) - \mathbf{h}(\mathbf{\Phi}_{n-1})\right\|_{L^2} .$$

By Taylor's Theorem, there exists $\mathbf{\Phi}^* \in S$ such that

$$\mathbf{h}(\mathbf{\Phi}_n) = \mathbf{h}(\mathbf{\Phi}_{n-1}) + \left(\frac{\partial}{\partial \mathbf{\Phi}}\mathbf{h}(\mathbf{\Phi}^*)\right)(\mathbf{\Phi}_n - \mathbf{\Phi}_{n-1}).$$

Therefore,

$$\|\mathbf{h}(\mathbf{\Phi}_n) - \mathbf{h}(\mathbf{\Phi}_{n-1})\|_{L^2} \leq \left\|\frac{\partial}{\partial \mathbf{\Phi}}\mathbf{h}(\mathbf{\Phi})\right\|_{L^\infty} \|\mathbf{\Phi}_n - \mathbf{\Phi}_{n-1}\|_{L^2}.$$

It can be shown that

$$\frac{EI\cos^2\theta}{|\mathbf{F}|}\left\|\frac{\partial}{\partial \mathbf{\Phi}}\mathbf{h}(\mathbf{\Phi})\right\|_{L^\infty} \leq C = \mathcal{O}(1).$$

Finally, we have

$$\|\mathbf{\Phi}_{n+1} - \mathbf{\Phi}_n\|_{L^2} \leq \frac{L^2|\mathbf{F}|C}{EI\cos^2\theta}\|\mathbf{\Phi}_n - \mathbf{\Phi}_{n-1}\|_{L^2}, \tag{4.60}$$

so, if $\frac{L^2|\mathbf{F}|C}{EI\cos^2\theta} < 1$ then we have a contraction. By the Banach fixed-point theorem, the sequence, $\{\mathbf{\Phi}_n\}$ converges.

□

Thus, we are ensured convergence using Picard iteration if the ratio of the beam force times the square of the beam length and the beam flexibility is small and the system is not near a state where $\cos\theta = 0$. Notice that these angles are also the angles that cause $\mathbf{G}$ to be singular. This method is especially unstable when θ is near such an angle.

Let the Galerkin finite element spaces $S^h \subset S$ and $W^h \subset W$ be defined using quadratic finite elements in the standard way. The element has 3 nodes with two on the element boundary and one at the element's midpoint. The

reference element is the range $[-1,1]$, and the shape functions on the reference element are

$$\mathbf{v_e^h}^T(\xi) = [v_1^h, v_2^h, v_3^h] = [\frac{1}{2}\xi(\xi-1), 1-\xi^2, \frac{1}{2}\xi(\xi+1)], \tag{4.61}$$

Let $\mathbf{\Phi}_1$, $\mathbf{\Phi}_2$ and $\mathbf{\Phi}_3$ designate the values of $\mathbf{\Phi}$ at nodes 1, 2 and 3 respectively and let $\mathbf{\Phi}_e = [\mathbf{\Phi}_1, \mathbf{\Phi}_2, \mathbf{\Phi}_3]$. $\mathbf{\Phi}_e^h = \mathbf{\Phi}_e \mathbf{v}_e^h$ and $\mathbf{\Phi^{h'}}_e = \mathbf{\Phi}_e \mathbf{v^{h'}}_e$. The Galerkin problem is to find $\mathbf{\Phi}_n^h \in S^h$ such that

$$-\left(\mathbf{\Phi}_n^{h'}, \mathbf{w^{h'}}\right)_B = \left(-\mathbf{G}^{-1}\mathbf{G'}\mathbf{\Phi}_{n-1}^{h'} + \mathbf{G}^{-1}\mathbf{E}^{-1}\hat{\mathbf{H}}, \mathbf{w^h}\right)_B \tag{4.62}$$

$\forall \mathbf{w}^h \in W^h$.

Let n be the iteration number. Let n_e be the number of beam elements and n_q be the number of quadrature points used on each element. Let $\mathbf{C}_e = [\mathbf{c}_1, \mathbf{c}_2, \mathbf{c}_3]$. Let $s_0, s_1, ..., s_{n_e}$ be the nodes on the element boundaries. Let h_e be the element diameters. Now, suppose $\mathbf{w}_e^h = \mathbf{C}_e \mathbf{v}_e^h$. Let ω_j and ζ_j for $j = 1, .., n_q$ be the quadrature weights and points for an n_q point quadrature rule. Now we have

$$\begin{aligned}
0 &= \left(\mathbf{\Phi}_n^{h'}, \mathbf{w^{h'}}\right)_B + \left(-\mathbf{G}^{-1}\mathbf{G'}\mathbf{\Phi}_{n-1}^{h'} + \mathbf{G}^{-1}\mathbf{E}^{-1}\hat{\mathbf{H}}, \mathbf{w^h}\right)_B \\
&= \sum_{i=0}^{n_e-1} \int_{s_i}^{s_{i+1}} [\left(\mathbf{\Phi}_{e,n}\mathbf{v_e^{h'}} \cdot \mathbf{C_e}\mathbf{v_e^{h'}}\right) \\
&+ \left(-\mathbf{G}^{-1}\mathbf{G'}\mathbf{\Phi}_{e,n-1}\mathbf{v_e^{h'}} + \mathbf{G}^{-1}\mathbf{E}^{-1}\hat{\mathbf{H}}\right) \cdot \mathbf{C_e}\mathbf{v_e^h}] ds \\
&\approx \sum_{i=0}^{n_e-1} \int_{s_i}^{s_{i+1}} \sum_{j=1}^{n_q} \omega_j [\frac{2}{h_e}\left(\mathbf{\Phi}_{e,n}\mathbf{v_e^{h'}} \cdot \mathbf{C_e}\mathbf{v_e^{h'}}\right) \\
&+ \frac{h_e}{2}(-\mathbf{G}^{-1}\mathbf{G'}\mathbf{\Phi}_{e,n-1}\mathbf{v_e^{h'}} + \mathbf{G}^{-1}\mathbf{E}^{-1}\hat{\mathbf{H}}) \cdot \mathbf{C_e}\mathbf{v_e^h}]|_{s=\zeta_j}.
\end{aligned} \tag{4.63}$$

This is only true for all $\mathbf{C_e}$ if for each element,

$$\begin{aligned} 0 &= \sum_{j=1}^{n_q} \omega_j [\frac{2}{h_e} \left(\mathbf{v^{h'}}_e (\mathbf{v^{h'}}_e)^T \mathbf{\Phi}_{e,n}^T \right) \\ &+ \frac{h_e}{2} (\mathbf{v}_e^h (-\mathbf{G}^{-1}\mathbf{G}'\mathbf{\Phi}_{e,n-1}\mathbf{v}_e^{h'} + \mathbf{G}^{-1}\mathbf{E}^{-1}\hat{\mathbf{H}})^T)] |_{s=\zeta_j}. \end{aligned} \tag{4.64}$$

Let

$$\mathbf{d}_e = [\mathbf{d}_1, \mathbf{d}_2, \mathbf{d}_3] = \sum_{j=1}^{n_q} \omega_j \left[-\frac{h_e}{2} (-\mathbf{v}_e^h (-\mathbf{G}^{-1}\mathbf{G}'\mathbf{\Phi}_{e,n-1}\mathbf{v}_e^{h'} + \mathbf{G}^{-1}\mathbf{E}^{-1}\hat{\mathbf{H}})^T \right] |_{s=\zeta_j} \tag{4.65}$$

and

$$\mathbf{K}_e = \sum_{j=1}^{n_q} \omega_j \left[\frac{2}{h_e} \ \mathbf{v^{h'}}_e (\mathbf{v^{h'}}_e)^T \right] |_{s=\zeta_j}. \tag{4.66}$$

$\mathbf{K}_e$ is the element stiffness matrix, and $\mathbf{d}_e$ is the matrix of element load vectors. Let $\boldsymbol{\psi}_e = [\psi_1, \psi_2, \psi_3]^T$, $\boldsymbol{\theta}_e = [\theta_1, \theta_2, \theta_3]^T$, and $\boldsymbol{\phi}_e = [\phi_1, \phi_2, \phi_3]^T$.

Now, form the global stiffness matrix $\mathbf{K}$, load vectors $\mathbf{d}_1$, $\mathbf{d}_2$, and $\mathbf{d}_3$ and solution vectors $\boldsymbol{\psi}$, $\boldsymbol{\theta}$, and $\boldsymbol{\phi}$. Impose the boundary conditions by deleting the first row and column of $\mathbf{K}$ and first entry of the load and solution vectors. This gives us the matrix problems

$$\mathbf{K}\boldsymbol{\psi} = \mathbf{d}_1, \tag{4.67}$$

$$\mathbf{K}\boldsymbol{\theta} = \mathbf{d}_2, \text{ and} \tag{4.68}$$

$$\mathbf{K}\boldsymbol{\phi} = \mathbf{d}_3. \tag{4.69}$$

Notice that these 3 problems are completely decoupled. In the full nonlinear finite element problem, the linear system we had to solve was $3n \times 3n$ where

n is the number of nodes. Here we solve 3 $n \times n$ systems, and we never have to update the stiffness matrix. While the linearized method may take more Picard iterations than the nonlinear finite element method takes Newton iterations, each iteration for the linearized method is much less expensive.

Using a 2 point Gauss quadrature rule, with $\omega_1 = \omega_2 = 1$, $\zeta_1 = -1/\sqrt{3}$ and $\zeta_2 = 1/\sqrt{3}$,

$$\mathbf{K}_e = \frac{1}{3h_e} \begin{bmatrix} 7 & -8 & 1 \\ -8 & 16 & -8 \\ 1 & -8 & 7 \end{bmatrix}, \tag{4.70}$$

4.3.3 Comparison of Methods

As shown in 4.2.1, the systems solved by the fully nonlinear method and the linearized methods presented above are equivalent. However, there are major differences with the numerical methods presented. For each iteration, the fully nonlinear method is much more expensive. The stiffness matrix $\mathbf{K}$ must be assembled for each iteration and a $3n \times 3n$, where n is the number of nodes, linear system must be solved. For the linearized method, the problem can be decoupled into 3 independent problems for each step. Also, the stiffness matrices are the same for each step, so they only need to be formed once. This is also beneficial for the linear solve, as an LU decomposition may be performed at a cost of $\sim \frac{2}{3}n^3$ floating point operations which allows the system to be solved by back substitution at a cost of $\sim n^2$ floating point operations. Therefore the total floating point operations for a Picard iteration for the linearized method is $\sim 6n^2$, where it is $\sim 18n^3$ for a Newton-Raphson iteration

for the nonlinear method. This excludes the cost of forming the stiffness matrix for the nonlinear method, which could be quite high. The approximations for counts of floating point operations for linear algebra are due to Trefethen and Bau [103]. It should be noted that for the nonlinear and linearized systems that the stiffness matrices are sparse banded matrices, for which there are many iterative methods one would use. However, we will generally be using relatively few beam elements, so our stiffness matrices will be of small dimension where dense direct solver techniques are less expensive than iterative ones. If one wanted to model beams with a large number of elements, iterative solvers would surely be a good choice; however, we generally see good results with a small number of beam elements.

Both methods have a significant problem being of unstable if $\theta = n\frac{\pi}{2}$ if $n = \pm 1, 3$. When θ has that value somewhere along the beam for the nonlinear method, the stiffness matrix $\mathbf{K}$ becomes singular. For the linearized method, it forces division by zero on the right-hand-side. Therefore, we must check to see if θ is close to one of these values before trying to solve the system. If it is close, then we add a small amount of noise to θ to avoid the instability. The Newton-Raphson and Picard iterations methods tend to be forgiving, and usually adding the noise does not hinder convergence.

A useful property of both methods is that they are designed to handle incremental loading. For large loads, if the load is applied to the system and the initial guess is not close to the stable equilibrium, the methods are very likely to diverge. However, if the load is incrementally increased and the equilibrium

state from the previous increment is used as an initial guess, then it is highly likely that the nonlinear iteration will converge. Taking incremental steps also may cause the method to converge with fewer total nonlinear steps. Each increment is likely to converge in very few steps; whereas, with no incremental loading the system may jump around for many steps before converging.

4.3.4 Beam Benchmark Problems

We test our two solution methods for large deflections of elastic cantilever beams with several benchmark problems. These problems test the ability of our methods to handle very large deflections due to end loads, uniform and variable distributed loads, and mixtures of types of loads. It is important that we verify that they provide accurate results for three-dimensional bending. We do this by testing all bending in the x-z plane, the y-z plane, and the plane 45 degrees between the two. We are also interested in convergence rates and the number of nonlinear iterations required for convergence.

It is standard for the test problems to non-dimensionalize the equations. We do that, in effect, by taking the length of the beam L to be 1 m and the flexibility EI to be 1 Nm^2 in our numerical methods. The test problems give non-dimensional end loads $\mathbf{F}$ and distributed loads $\mathbf{q}$. We take the nonlinear tolerance used to test convergence to be 1.0×10^{-4} for all cases. The initial guess for all methods will be an undeformed, straight beam.

The first benchmark problems that we look at are from Fried [27]. Their method is well-validated for large deflections and is similar to a 2D version of

the nonlinear method presented here. The first test takes $F_1 = 1.5$ and all other loads to be 0. They use 4 cubic elements, and we use 4 quadratic elements. Table 4.1 shows the end deflections for the converged system for the first 6 iterations for Fried's [27] method and our two methods. We see that after only a few iterations both of our methods are extremely close to their converged values and they match up very well with the previous results. The converged deflections are 0.4109928 m for the previous results and 0.41097726 m for both of our methods. It is important to note that this problem is a large-deflection problem and one that small-deflection methods would generally fail at solving. Using only 4 elements and a small number of nonlinear iterations, our methods are capturing the correct deflections.

	Horizontal End Deflection (m)		
Iteration num.	Fried [27]	Nonlinear	Linearized
1	0.5000000	0.46857929	0.46857929
2	0.4337216	0.41195049	0.39038892
3	0.4124599	0.41097754	0.41736212
4	0.4109994	0.41097726	0.40889655
5	0.4109928	0.41097726	0.41164489
6	0.4109928	0.41097726	0.41076195
Converged Value	0.4109928	0.41097726	0.41097726

Table 4.1: Horizontal end deflections for the first 6 iterations and the converged values for an end load of $F_1 = 1.5$. The results shown are from Fried [27] and the nonlinear finite element method and linearized method presented above.

For a similar problem Fried [27] also presents convergence data. An end load $F_1 = 5.0$ is used with the number of elements used ranging from 1 to 9. The deflection of the end of the beam is the value of interest. Table

4.2 gives the end deflection for Fried's method and our nonlinear method for each number of elements. Our linearized method failed even using incremental loading for this problem. This is not unexpected for such a large deflection. For each refinement level, our method gives a smaller relative error than the previous results. To calculate the relative error we took the true value to be 0.713791524 m which is the deflection from our nonlinear method using 100 elements. Fried's method gives a convergence rate of 3.45 and our method gives a rate of 4.13. We do not have a good explanation for our high order of convergence. Using a 7 element configuration, Fried [27] gives deflections at stable equilibria for the full length of the beam for end loads ranging from 0.5 to 9.0 in increments of 0.5. We performed the same tests, and our results can be seen in Figure 4.3. Deflection data from our nonlinear method matches exceedingly well with Figure 3 in the article by Fried [27].

We take a suite of benchmark problems for distributed loads from Dado and Al-Sadder [16]. For plant bending due to fluid resistance distributed loads are a much bigger factor than end loads, so these tests are incredibly important to verify our methods. Dado and Al-Sadder [16] approximate the center line of the beam as a high-order polynomial and formulate a method to minimize the integral of the residual error. They verify their method against results from the MSC/NASTRAN commercial finite element package. This packages divides the beam into a large number of two-dimensional beam elements. They perform tests for prismatic and non-prismatic beams, but since our interest is only for prismatic beams, we only look at those tests.

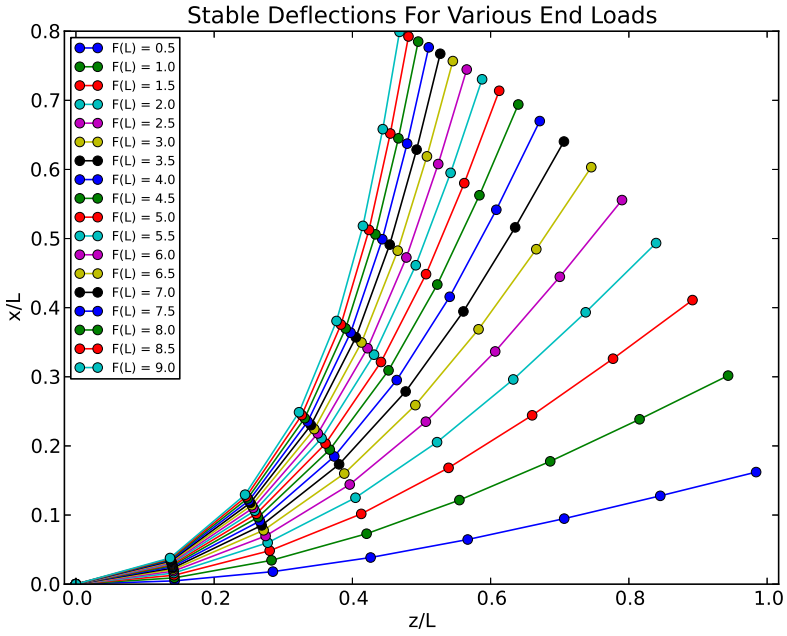

Figure 4.3: Stable deflection configurations for a cantilever beam loaded with a range of end loads.

The first test is for uniformly distributed loads in the lateral direction. The configuration for this test is shown in Figure 4.4. A range of uniform distributed loads $q = -4, -10, -20, -40, -100$ are used. Dado and Al-Sadder [16] solved for the stable equilibria using their method with a 15th order polynomial and using MSC/NASTRAN with 100 elements. MSC/NASTRAN failed due to divergence for loads of -40 and -100. Figure 4.5 shows stable deflection configurations given the designated loads using our fully nonlinear method. 10 quadratic beam elements and a nonlinear tolerance of 1.0×10^{-4} were used. Essentially, the same deflection results were attained using the nonlinear finite element method and the linearized method and they match very well with the results from Dado and Al-Sadder [16]. There was, however, significant variation in the number of nonlinear iterations required for convergence between the two methods. The number of iterations also depends greatly on the number of incremental loading steps and the plane in which the bending occurs. Table 4.3 shows the total number of Newton-Raphson iterations required for each load value using the fully nonlinear method for bending in the x-z plane, the y-z plane, and the diagonal plane. We see that using more than 1 load step the number of iterations for x-z bending and y-z bending are identical. However, for diagonal bending the method diverges for low numbers of load steps. We also see divergence for very large deflection in the y-z plane and only one step. We see for bending in each direction, that taking too many incremental loading steps can cause many unnecessary iterations to be taken. Going from 10 to 15 loading steps increases the total number of iterations for

bending in all directions. In order to avoid divergence of the method and high computational cost, between 5 and 10 loading steps are optimal.

The linearized method does not handle large deflections nearly as well as the nonlinear method. Because of this, we could only test this method for smaller loads: $q = -2, -4, -6, -8, -10$ Table 4.4 shows the total number of Picard iterations required for each load value using the linearized method. No matter how many loading steps were used, for the case $q = -10$ this method required over 1000 iterations to converge for bending in the x-z and y-z planes. It failed in all cases for $q < -4$ in the diagonal plane. This exhibits the main drawbacks of the linearized method. It works relatively well for bending in planes near the 2 main axes, but tends to fail otherwise. For very small deflections, with no loading it converges in relatively few steps and is less computationally expensive than the nonlinear method. However, it requires a prohibitive number of Picard iterations for larger loads or diverges. Incremental loading does not seem to help this method, as in each case doing incremental loading increased the overall cost. While we have seen this method work relatively well for end loads, it is not particularly successful for distributed loads.

The final beam benchmark problem from Dado and Al-Sadder is one that tests if the methods can handle truly large deflections. The configuration is shown in Figure 4.6 and includes a uniform vertical load $q_3 = -5$ and a linearly distributed horizontal load. The horizontal load q is 0 at the base of the beam and q_y at the end. We take values of q_y = -1,-5,-10,-15,-20,-

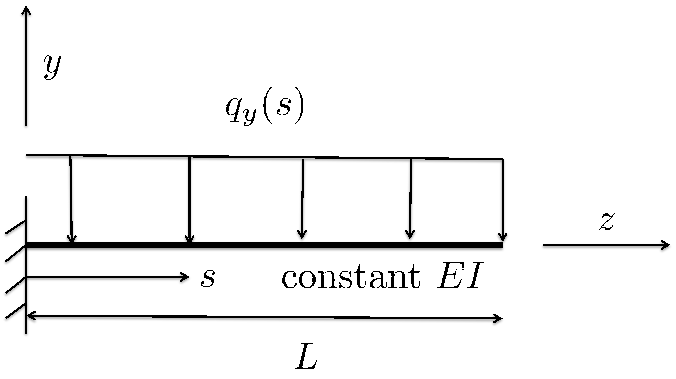

Figure 4.4: Configuration of the uniformly distrubted load test problem.

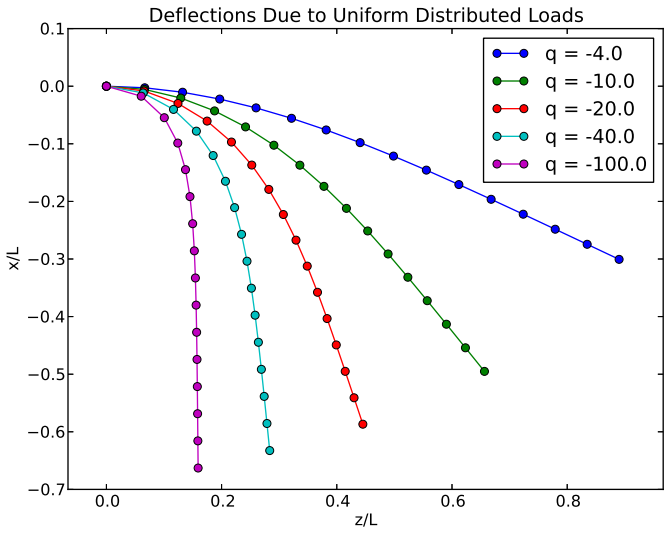

Figure 4.5: Deflections for the uniformly distrubted load test problem.

	Horizontal End Deflection (m)			
Num. of Elements	Fried [27]	Rel. Error	Nonlinear Method	Rel. Error
1	0.7669329	0.07444	0.705610	0.01146
2	0.718933	0.00720	0.713325	0.00065
3	0.7151829	0.001949	0.713712	0.00011
4	0.7143314	0.00075	0.7137673	3.4E-5
5	0.7140374	0.00034	0.713782	1.4E-5
6	0.7139174	0.00017	0.713787	6.6E-6
7	0.7138622	9.9E-5	0.713789	3.6E-6
8	0.7138340	5.9E-5	0.713790	2.1E-6
9	0.7138185	3.8E-5	0.713791	1.3E-6
Conv. Rate		$O(h^{3.45})$		$O(h^{4.13})$

Table 4.2: Convergence results for an end load $F_1 = 5.0$.

		Distributed Loads				
		-4	-10	-20	-40	-100
bending plane	num. of load steps	Total num. of iterations				
x-z plane	1	4	4	33	163	100
	5	15	15	17	16	40
	10	30	30	30	32	31
	15	42	45	45	42	43
y-z plane	1	4	4	30	47	*
	5	15	15	17	16	34
	10	30	30	30	32	31
	15	42	45	45	42	43
diagonal plane	1	4	5	*	*	*
	5	15	15	17	17	*
	10	30	30	30	32	33
	15	45	45	45	47	46

Table 4.3: Total number of Newton-Raphson iterations for the uniform distributed load benchmark problem for a range of loads in different planes using the fully nonlinear method. * denotes that the method diverged.

30,-50,-80, -100, -120. This configuration leads to extremely large deflections.

For the case $q_y = -120$ the stable equilibrium has the beam bent nearly 180

		Distributed Loads				
		-2	-4	-6	-8	-10
bending plane	num. of load steps	Total num. of iterations				
x-z plane	1	4	7	13	31	1516
	5	17	24	34	59	1483
	10	30	43	60	94	1455
	20	55	77	106	162	1497
y-z plane	1	4	7	13	31	1516
	5	17	24	34	59	1483
	10	30	43	60	94	1455
	20	55	77	106	162	1497
diagonal plane	1	8	29	*	*	*
	5	24	46	*	*	*
	10	41	71	*	*	*
	20	74	119	*	*	*

Table 4.4: Total number of Picard iterations for the uniform distributed load benchmark problem for a range of loads in different planes using the linearized. * denotes that the method diverged.

degrees from the unloaded state. Using the linearized method, these very large-deflection problems always diverged. Figure 4.7 shows the stable equilibria positions under these particular loads using our nonlinear method. These match up almost perfectly with results from Dado and Al-Sadder's polynomial method. The MSC/NASTRAN method failed to converge for $q_y < -20$, but our nonlinear results match up with those results for the smaller loads.

Table 4.5 shows the total number of Newton-Raphson iterations required for convergence for bending in different planes and with different numbers of incremental loading steps. We see identical numbers of iterations for each case in the x-z and y-z planes. It is interesting that for these cases, even

		Distributed Loads									
		-1	-5	-10	-15	-20	-30	-50	-80	-100	-120
plane	load steps	Total num. of iterations									
x-z	1	4	5	22	4*	3*	3*	3*	2*	2*	2*
	5	15	17	19	22	26	16*	14*	14*	12*	12*
	10	29	30	35	35	37	47	26*	45*	25*	23*
	25	50	69	71	75	78	81	84	78*	96*	78
	50	100	124	136	140	142	147	146	147	147	149*
	100	200	200	255	260	256	249	249	247	248	248
y-z	1	4	5	22	4*	3*	3*	3*	2*	2*	2*
	5	15	17	19	22	26	16*	14*	14*	12*	12*
	10	29	30	35	35	37	47	26*	45*	25*	23*
	25	50	69	71	75	78	81	84	78*	96*	78
	50	100	124	136	140	142	147	146	147	147	149*
	100	200	200	255	260	256	249	249	247	248	248
diag.	1	4	6	*	*	*	*	*	*	*	*
	5	15	16	21	*	*	*	*	*	*	*
	10	30	30	36	40	*	*	*	*	*	*
	25	75	75	75	83	88	102	*	*	*	*
	100	200	200	259	276	282	288	317	*	*	*
	200	400	400	400	510	547	567	591	621	*	*
	500	1000	1000	1000	1000	1000	1178	1242	1294	1314	1325

Table 4.5: Total number of Newton-Raphson iterations for mixed distributed load benchmark problem for a range of horizontal linearly distributed loads. A plain * denotes that the method diverged. A number followed by * denotes that the method converged to an unstable equilibrium in that number of iterations.

for the very large loads with a small number of load steps the method always converged. However, as seen in Table 4.5, it often converged to an unstable equilibrium. These are not states that are global minima of the beam energy functional, so they are not the correct deflections. Using a large number of incremental loads allows us to avoid this problem, though. With 100 load steps the method converged to stable equilibria even for the greatest loads. For more reasonable loads, once again between 5 and 10 load steps were computationally optimal. For bending in the diagonal plane, rather than converging to unstable equilibria, the method tended to diverge if too few incremental load steps were taken. The method also required many more total iterations to converge

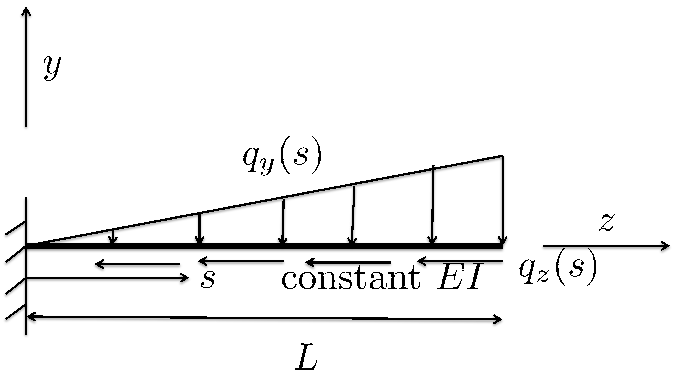

Figure 4.6: Configuration of the uniformly distrubted load test problem.

in the diagonal plane than the other planes. Still, taking 500 incremental load steps, it converged to the correct stable equilibria, even for the greatest loads.

4.3.5 Discussion and Conclusions Concerning Beam Methods

The most obvious conclusion from the benchmark problems it is that the fully nonlinear method of minimizing the energy functional of the beam using adequate incremental loading is an extremely robust, computationally inexpensive, highly accurate method for finding the stable deflected state of a cantilever beam with an end or distributed load applied to it. This method matched results from several other methods and worked even for incredibly large deflections. The deflections shown in 4.7 are much greater than we would expect for any plant interacting with a realistic fluid flow. For reasonable loads, generally 5 or 10 incremental steps were enough to ensure convergence without taking a great number of unnecessary iterations. We have also shown that

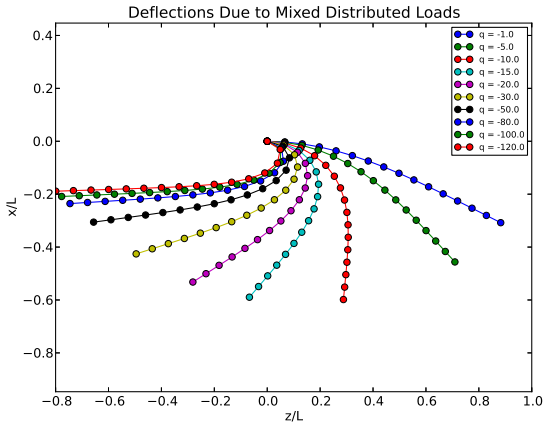

Figure 4.7: Deflections for the uniformly distrubted load test problem.

the method handles complex loads in more than one direction. The method converged with many fewer iterations if the deflection occurs close to the x-z or y-z planes. Away from those planes, taking enough incremental load steps ensures convergence. Therefore for flow coupling scenarios, it is best to align one of those planes with the primary flow direction if known. This is the direction in which most of the bending will occur, so it should cause fewer iterative steps to need to be taken.

The method converges at a very high rate, so for most cases only a small number of beam elements are necessary. For modeling flexible vegetation with this method, having at least 5 or 6 beam elements per plant and using 10 incremental loading steps is an adequate model that is robust and unlikely to diverge for a realistic load due to flow resistance. When modeling a larger scale flow, we may have thousands or millions of plants in the flow modeled

as cantilever beams. Therefore, this low computational cost and robustness is essential. Taking too many iterations and divergence issues would be a major bottleneck in a coupled flow/bending code.

The linearized method is much more problematic than the nonlinear method. We see that it handles small and moderate end loads very well without requiring a large number of iterations. It is important to note that each Picard iteration for this method is much cheaper than a Newton-Raphson iteration for the previous method. However, for even moderate distributed loads this method has a tendency to diverge even with a large number of incremental load steps taken. For small deflections of the beam the linearized method is just as accurate and much cheaper computationally than the nonlinear method. However, past a threshold load it either requires a huge number of iterations to converge or diverges. It is important to note that the "small" deflections for which this method works are still considered to be "large" deflections in beam modeling. In a scenario where the loads are expected to be quite small, the linearized method is cheaper than the nonlinear method and nearly as reliable. For most scenarios, however, the nonlinear method is much more reliable.

4.4 Coupling Flow and Flexible Vegetation Models

4.4.1 Loads and Sink Terms

The bending of the vegetation is caused by a distributed load that results from the drag force caused by the flow moving past it. The concept of drag is discussed in depth in Section 3.2. The distributed load $\mathbf{q}$ is a force

per unit length of the beam in units kg/s^2. As described by Kutija and Hong [53] the distributed load due to the drag of a fluid with density ρ and mean velocity $\mathbf{V} = [V_1, V_2, V_3]^T$ over the length of the beam is

$$q_i(s) = C_d(s)\frac{1}{2}b(s)\rho V_i(s)\sqrt{V_j(s)V_j(s)} \tag{4.71}$$

where the double index notation implies summation in the standard way, C_d is the drag coefficient for one obstacle and b is the diameter. s is the coordinate along the center-line of the beam. Hoerner [36] describes drag coefficients for commonly shaped objects over a large ranges of Reynolds numbers. For a single upright circular cylinder, $C_d \approx 1.2$ for Re between 1.0×10^2 and 3.0×10^5. Almost every flow that we want to deal with lies in this range and a circular cylinder is a good approximation of the shape of a stem.

The drag force that causes the bending of the vegetation must be considered in the flow equations as well. This is generally done by including it as a sink term in the momentum. Kutija and Hong [53] show that the correct sink term to balance the forces is

$$f_i(\mathbf{x}) = -C_d\frac{1}{2}b(\mathbf{x})\rho(\mathbf{x})V_i(\mathbf{x})\sqrt{V_j(\mathbf{x})V_j(\mathbf{x})} \tag{4.72}$$

for one stem. They propose that the force per unit unit volume for a packing of stems is

$$F_i(\mathbf{x}) = N_v f_i \tag{4.73}$$

where N_v is the number of stems per unit horizontal area (in m^{-2}) for a packing of stems. Li and Xie [54] adjust this by using drag coefficients that factor in

foliage on the plant and the shape of the bent-over plants. However, these studies overlook the concept of bulk drag as discussed in Section 4.1. We propose that the sink term for a packing of stems is

$$\tilde{F}_i(\mathbf{x}) = -\tilde{C}_d \frac{1}{2} b(\mathbf{x}) N_v \rho(\mathbf{x}) V_i(\mathbf{x}) \sqrt{V_j(\mathbf{x}) V_j(\mathbf{x})} \tag{4.74}$$

where $\tilde{C}_d$ is not necessarily equal to C_d. Note that this force is equivalent to the beam force $\mathbf{F}$ described in Section 4.2.1. We couple our fluid and structure models using these drags and momentum sinks within the framework of an immersed boundary method.

4.4.2 The Immersed Boundary Method

The immersed boundary (IB) method is a method for modeling the interaction between incompressible Newtonian fluids and elastic solids. It was developed by Peskin [77] and is mostly used for modeling biological systems, especially cardiovascular systems. Generally, fluid models are defined in Eulerian frameworks and elastic structure models are defined in Lagrangian frameworks. The IB method allows for separate Eulerian and Lagrangian domains and meshes. Using integral transforms involving the Dirac delta generalized function, the effects of the Eulerian domain are mapped to the Lagrangian domain and vice versa. This is convenient so that the most natural frameworks may be used for the fluid and structure models, and simple meshes can be used. The meshes also do not move, as they do in the other most common method of modeling fluid-structure interaction, the arbitrary Lagrangian-Eulerian (ALE) method. In ALE, the meshes move, and for large deformations, it can be

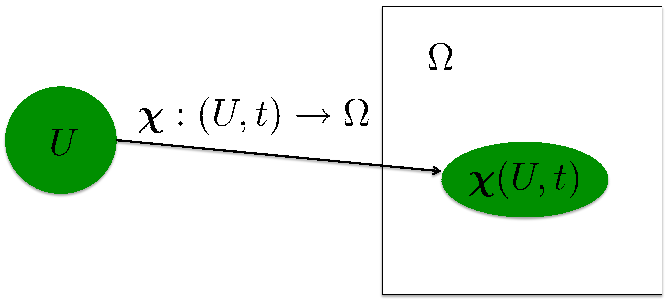

Figure 4.8: The separate Lagrangian and Eulerian domains U and Ω, respectively for the immersed boundary method. $\boldsymbol{\chi}$ maps U into Ω.

twisted. The IB method has been applied to flow around beams by Borges et al. [9]; however, it was for small-deflections.

Suppose U is the Lagrangian domain for the elastic structure and that Ω is the Eulerian fluid domain. In the Eulerian sense, U changes in time. Let

$$\boldsymbol{\chi} : (U,t) \rightarrow \Omega \tag{4.75}$$

be a mapping of the structure domain at time t into the fluid domain, such that $\boldsymbol{\chi}(s,t)$ is the location of the structure at coordinate s and time t in the fluid domain Ω. $\Omega \setminus \boldsymbol{\chi}(U,t)$ is the physical region occupied by the fluid and $\boldsymbol{\chi}(U,t)$ is the physical region occupied by the structure at time t. Formulations for the IB method for standard linear and nonlinear elasticity problems are described thoroughly by Peskin [77] and Griffith and Luo [34].

The fundamental principle behind the IB method is that one may use

integral transforms involving the Dirac delta to map between the Eulerian and Lagrangian frameworks. Notice that (4.71) and (4.72) involve values that are naturally functions of $\mathbf{x}$ and s. When modeling flow with many resolved stems the sink term (4.72) should not be imposed everywhere in the flow. It must only be imposed where there is a stem. Here we are assuming that the stem is a 1D manifold; although, the 3D nature of it is taken into consideration by the stem diameter and drag coefficient terms in (4.71) and (4.72). We suppose that the 1D beam domain is immersed in the 3D fluid domain. Using the IB method, we can calculate the distributed load on each beam and momentum sink per unit volume on the fluid by

$$q_i(s) = C_d \frac{1}{2} b(s) \int_\Omega \rho(\mathbf{x}) v_i(\mathbf{x}) \sqrt{v_j(\mathbf{x}) v_j(\mathbf{x})} \delta(\mathbf{x} - \boldsymbol{\chi}(s)) d\mathbf{x} \tag{4.76}$$

and

$$F_i(\mathbf{x}) = -C_d \frac{1}{2} \rho(\mathbf{x}) v_i(\mathbf{x}) \sqrt{v_j(\mathbf{x}) v_j(\mathbf{x})} \int_U b(s) \delta(\mathbf{x} - \boldsymbol{\chi}(s)) ds \tag{4.77}$$

where U is the 1D center-line of the the beam and Ω is the 3D fluid domain. Note that these formulas involve the variable velocity $\mathbf{v}$, not $\mathbf{V}$, the mean over the length of the beam. By integrating over the length of the beam the mean effect is captured. $\boldsymbol{\chi}$ maps the beam location in terms of the arc length coordinate s to the location in the fluid domain Ω. $\boldsymbol{\chi}(s)$ is equivalent to $\mathbf{r}(s)$ introduced in Section 4.2 and defined as solutions to first order ordinary differential equations in terms of Euler angles in (4.29) - (4.31). These simple ODEs may easily be solved by numerical integration using quadrature. Therefore,

when the beam system is solved for the Euler angles given a certain load, $\boldsymbol{\chi}$ can easily be calculated.

The above formulation ensures that the momentum for the coupled beam/fluid system is conserved. The exact force that goes into bending the beam is lost from the fluid in the source term. We see this by integrating the distributed load $\mathbf{q}$ over the beam and integrating the sink $\mathbf{F}$ over the fluid domain:

$$\begin{aligned}
& \int_U q_i ds + \int_\Omega F_i d\mathbf{x} \\
= & \int_U C_d \frac{1}{2} b(s) \int_\Omega \rho(\mathbf{x}) v_i(\mathbf{x}) \sqrt{v_j(\mathbf{x}) v_j(\mathbf{x})} \delta(\mathbf{x} - \boldsymbol{\chi}(s)) d\mathbf{x} ds \\
+ & \int_\Omega -C_d \frac{1}{2} \rho(\mathbf{x}) v_i(\mathbf{x}) \sqrt{v_j(\mathbf{x}) v_j(\mathbf{x})} \int_U b(s) \delta(\mathbf{x} - \boldsymbol{\chi}(s)) ds d\mathbf{x} \\
= & \int_U \int_\Omega C_d \frac{1}{2} b(s) \rho(\mathbf{x}) v_i(\mathbf{x}) \sqrt{v_j(\mathbf{x}) v_j(\mathbf{x})} \delta(\mathbf{x} - \boldsymbol{\chi}(s)) d\mathbf{x} ds \\
+ & \int_\Omega \int_U -C_d \frac{1}{2} \rho(\mathbf{x}) v_i(\mathbf{x}) \sqrt{v_j(\mathbf{x}) v_j(\mathbf{x})} b(s) \delta(\mathbf{x} - \boldsymbol{\chi}(s)) ds d\mathbf{x} \\
= & \ 0. \qquad (4.78)
\end{aligned}$$

In a coupled physical fluid/beam system there is an additional load on the beams due to weight and buoyancy. Let ρ_f be the density of the fluid and ρ_s be the density of the structure. Assuming a beam with a cross sectional area A, the load on the beam due to gravity and buoyancy is

$$\hat{q}_3 = (\rho_f - \rho_s) A. \qquad (4.79)$$

In the beam solving step $\hat{q}_3$, must be added to q_3; however, it is not included in the above force balance because momentum is not being taken away from the fluid because of buoyancy.

4.4.3 Numerical Concerns for Immersed Boundary Method

In practice, we cannot use the Dirac delta generalized function because we integrate using quadrature and do not want to have to make changes to the meshes. The quadrature points for the beams and the fluid would have to match up for us to be able to use δ, which would be quite difficult to implement for a moving immersed structure. Instead we use an approximation to the Dirac delta δ_h. It is essential that this approximation is bounded, continuous, and has compact support. We use an approximation designed for the immersed boundary method by Peskin [77]:

$$\delta_h(\mathbf{x}) = \frac{1}{h^3}\phi(\frac{x_1}{h})\phi(\frac{x_2}{h})\phi(\frac{x_3}{h}), \tag{4.80}$$

where h is the beam element size and

$$\phi(r) = \begin{cases} 0, & r \leq -2 \\ \frac{1}{8}(5 + 2r - \sqrt{-7 - 12r - 4r^2}), & -2 \leq r \leq -1 \\ \frac{1}{8}(3 + 2r + \sqrt{1 - 4r - 4r^2}), & -1 \leq r \leq 0 \\ \frac{1}{8}(3 - 2r + \sqrt{1 + 4r - 4r^2}), & 0 \leq r \leq 1 \\ \frac{1}{8}(5 - 2r - \sqrt{-7 + 12r - 4r^2}), & 1 \leq r \leq 2 \\ 0, & 2 \leq r. \end{cases} \tag{4.81}$$

The function ϕ is shown in Figure 4.9. For this formulation of δ_h, we see that $\delta_h \to \delta$ as $h \to 0$. Also, note that the momentum balance (4.78) still holds replacing δ with δ_h and integrating over both B and Ω using quadrature. Using δ_h rather than δ leads to the "smearing" of the effects of the Lagrangian mesh on the Eulerian mesh and vice versa. Since we are interested in mean flow characteristics, this is not a problem, since momentum is conserved, as long as the meshes are properly refined.

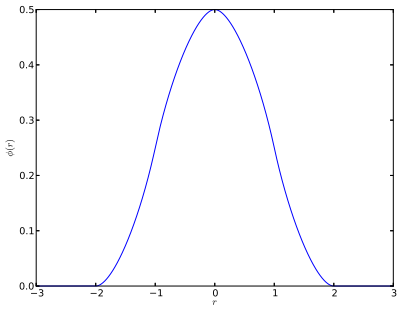

Figure 4.9: The function ϕ used for calculating δ_h.

We see that using approximation to δ_h has a support of 2 beam element lengths in any direction. It is essential that the mesh spacing is chosen in such away that δ_h is a good approximation to δ for integration over this small region. Griffith and Luo [34] investigate mesh spacing for integration using Gaussian quadrature. If h is the mesh spacing for the Lagrangian mesh and h_f is the average mesh spacing for the Eulerian mesh, they experimented with $h/h_f = 1$, $h/h_f = 2$, and $h/h_f = 4$, and found that $h/h_f = 2$ gave optimal results. In fact, it is standard practice in fluid-structure interaction problems to use a Lagrangian mesh twice as coarse as the Eulerian mesh. Therefore, we choose this refinement ratio for all simulations.

We verify that our use of δ_h leads to proper calculations of loads and sinks. First we assume the fluid has a uniform velocity profile $v_1 = 1$ m/s, $v_2 = v_3 = 0$. We use the three point Gaussian quadrature rule for the beam and four point, second order Gaussian quadrature rule for the 3D fluid mesh. The fluid mesh consists of unstructured tetrahedra with a maximum element

diameter half that of the uniform element size of the 1D beams. The beam length was taken to be 0.5 m, the beam radius was taken to be 0.01 m, $C_d = 1.2$, and $\rho = 998.0$ kg/m^3. Calculating $\mathbf{q}$ using (4.76) with the true δ and then integrating over the beam should give a total drag force of 5.9889 kgm/s^2. We also experimented with a linear velocity profile $v_1 = z$ with all other parameters the same. For this case the total drag force analytically is 0.4990 kgm/s^2. Table 4.6 shows calculated total drag values and the relative error for fluid mesh sizes ranging from 0.1 m to 0.0015625 m for both uniform and linear velocity profiles. We see close to linear convergence rates for both cases. For mesh refinements of 0.025 for the uniform case and 0.05 for the linear case, we see error less than 5% which is quite reasonable considering the complexity of the model.

	$v_1 = 1$		$v_1 = z$	
h_f	Total Drag	Relative Error	Total Drag	Relative Error
0.1	5.0334	0.159418	0.5358	0.07374
0.05	5.5497	0.073196	0.5201	0.04228
0.025	5.7751	0.035554	0.5059	0.01382
0.0125	5.8854	0.017134	0.5012	0.00441
0.00625	5.9397	0.008066	0.4999	0.001803
0.003125	5.9665	0.003591	0.4995	0.001002
0.0015625	5.9799	0.001353	0.4995	0.001002
Analytical	5.988		0.4990	

Table 4.6: Total drag force values calculated using immersed boundary formulation for uniform and linear velocity profiles.

4.4.4 Steady-State Problem

We can formulate a steady fluid-structure interaction problem using the IB formulation. Rather than just a single beam, we can have many beams, say n_{beam}. Call the Lagrangian domain for each beam B_k and let b_k be the diameter function and $\boldsymbol{\chi}_k$ be the mapping into Ω of beam k. The bulk sink due to all of the beams is

$$\tilde{F}_i(\mathbf{x}) = \sum_{k=1}^{n_{beam}} F_i^k(\mathbf{x}) \tag{4.82}$$

where

$$F_i^k(\mathbf{x}) = -C_d \frac{1}{2} \rho(\mathbf{x}) v_i(\mathbf{x}) \sqrt{v_j(\mathbf{x}) v_j(\mathbf{x})} \int_{B_k} b_k(s) \delta_h(\mathbf{x} - \boldsymbol{\chi}_k(s)) ds. \tag{4.83}$$

The corresponding distributed load on beam k is

$$q_i^k(s) = C_d \frac{1}{2} b_k(s) \int_{\Omega} \rho(\mathbf{x}) v_i(\mathbf{x}) \sqrt{v_j(\mathbf{x}) v_j(\mathbf{x})} \delta_h(\mathbf{x} - \boldsymbol{\chi}_k(s)) d\mathbf{x}. \tag{4.84}$$

The steady flow system is

$$\begin{aligned} \nabla \cdot \mathbf{v} &= 0 \\ \nabla \cdot (\mathbf{v} \otimes \mathbf{v} - \nu(\nabla \mathbf{v} + \nabla \mathbf{v}^T)) &= -\frac{1}{\rho} \nabla p + \mathbf{g} + \frac{1}{\rho} \tilde{\mathbf{F}} \end{aligned} \tag{4.85}$$

with the sink term above included. We can develop an iterative method to solve for a steady-state solution for the fluid-structure interaction problem:

- Initialize fluid system.
- Calculate loads on beams using (4.84).

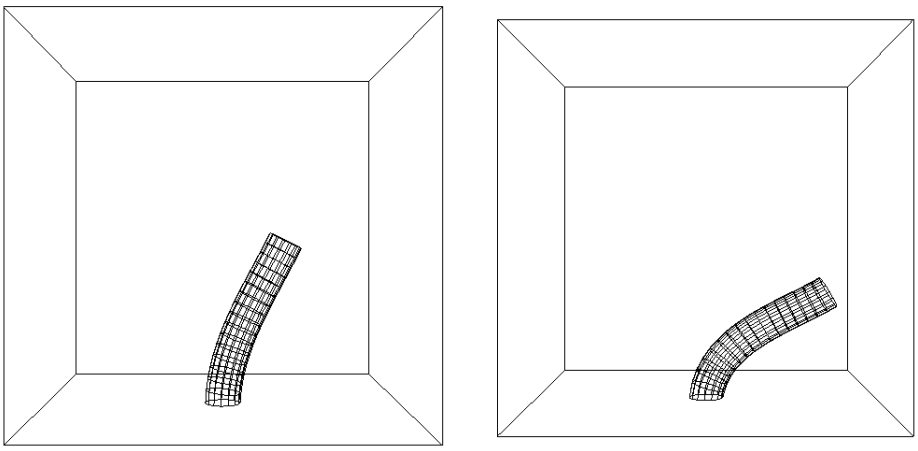

Figure 4.10: Cantilever beams bent to steady-state positions due to uniform velocities of 0.01 m/s and 0.1 m/s with flexural rigidity $EI = 3 \times 10^{-8}$ kgm^3/s^2 solved using the immersed boundary method.

- Solve beam systems using the previous step as initial steps for iterative method. Integrate to find $\boldsymbol{\chi}_k$.
- Calculate sink terms using (4.82).
- Solve fluid system (4.85) using the previous step as initial condition for iterative method.
- Repeat until both fluid and beam models converge within given tolerance from step to step.

This gives a steady-state solution to the coupled beam and fluid model. Figure 4.10 shows steady-state bent beam profiles caused by initial uniform velocity fields of 0.01 m/s and 0.1 m/s.

4.4.5 Dynamic Problem

For the dynamic fluid-structure interaction problem, we utilize a quasi-static model for the beams and a dynamic Navier-Stokes model as discussed in Chapter 2. Assume that we have time steps t_n. Now, $\boldsymbol{\chi}_k$, $\mathbf{q}^k$, and $\tilde{\mathbf{F}}$ are functions of time as well. They dynamic flow system is

$$\begin{aligned} \nabla \cdot \mathbf{v} &= 0 \\ \frac{\partial \mathbf{v}}{\partial t} + \nabla \cdot (\mathbf{v} \otimes \mathbf{v} - \nu(\nabla \mathbf{v} + \nabla \mathbf{v}^T)) &= -\frac{1}{\rho}\nabla p + \mathbf{g} + \frac{1}{\rho}\tilde{\mathbf{F}}. \end{aligned} \tag{4.86}$$

The dynamic fluid-structure interaction method at time step t_n is:

- Calculate loads on beams (4.84) and momentum sinks (4.82) using velocity at t_{n-1}.
- Solve beam systems using the previous step as initial steps for iterative method. Integrate to find $\boldsymbol{\chi}_k(t_n)$.
- Solve fluid system (4.86) using time integration to time t_n.

4.5 Model Problems

We execute the immersed structure approach for two types of model problems: channel flow problems and wave tank problems. These two types of problems were chosen for a variety of reasons. Vegetated channels are extremely common in nature. A vegetated coastal region is very similar to a

vegetated channel with an extremely large horizontal length. Also, there have been a great deal of experimental studies for flow through vegetated channels containing rigid and flexible vegetation. We can reproduce the geometry of these channels exactly on a computational domain and thus, can compare our computational results to experimental results for the exact same setup. We compare our computational results to experimental studies of vegetated channels by Dunn et al. [23] and Nepf [73] as discussed in Section 4.1.2. Also in that section, we discuss the connection between wave attenuation and bulk drag. The existence of vegetation has a major effect on wave attenuation in near-shore environments. We create computational "wave tanks" that generate linear planar gravity waves using a two-phase flow method and measure the mean drag as they travel through a bed of vegetation. We reproduce the geometry from experiments by Wu et al. [115] and compare calculated bulk drag coefficients over large ranges of Reynolds numbers. It is important to note that the bulk drag coefficient $\tilde{C}_d$ is dependent on the type of flow. For a channel flow, the flow travels mostly in one horizontal direction, passing through the bed of vegetation as it flows. For a wave-dominated flow, the fluid moves in large eddies with a mean velocity in a horizontal direction, but passing through more vegetation as it rotates. Therefore, we expect the bulk drag coefficient to be higher for a wave tank than for channel flow.

As in these experimental studies, we arrange the vegetative obstacles in a staggered configuration as shown in Figure 4.11. The distance between each stem's center and the center of its closest neighbor is λ. The corresponding

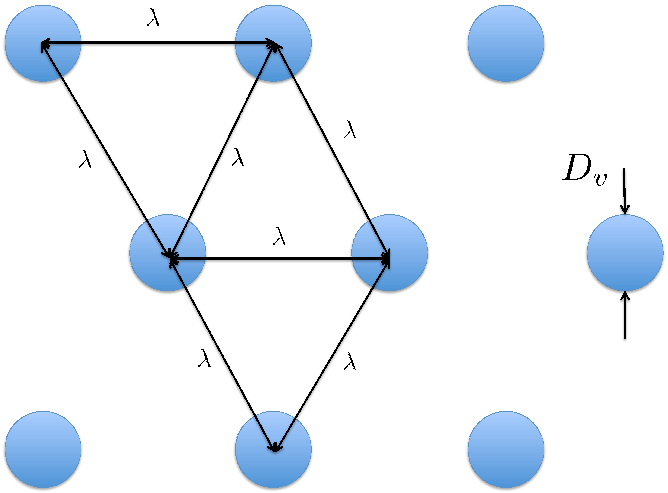

Figure 4.11: Horizontal spacing of vegetative obstacles for channel and wave tank setups.

population density N_v is then calculated by

$$N_v = \frac{2}{\sqrt{3}}\lambda^{-2}. \tag{4.87}$$

We assume that the domains have smooth bottoms, so that there is no bottom friction. To model rigid vegetation, we use a variation of the immersed structure approach discussed in the previous section. Since the structures will not be moving, we do not need to calculate the loads on them or recalculate the mapping $\boldsymbol{\chi}_k$ into the fluid domain. We just need to initialize $\boldsymbol{\chi}_k$ for each beam and use it to calculate the sink term at each fluid quadrature point in the fluid model at each time step. For flexible vegetation we use the full dynamic immersed boundary fluid-structure interaction method presented in the previous section. Beam elasticities, radii, and lengths are chosen to match the

materials used in the experiments.

Suppose that $\tilde{\Omega}$ is the vegetated region of the domain in which we are interested. The net drag force per unit volume is then

$$F_{drag} = \frac{\int_{\tilde{\Omega}} |\tilde{\mathbf{F}}| d\mathbf{x}}{\int_{\tilde{\Omega}} \mathbf{dx}}, \tag{4.88}$$

where $\tilde{\mathbf{F}}$ is as defined in (4.1). To calculate the bulk drag coefficient we want the mean drag force, so we time average:

$$\bar{F}_{drag} = \frac{1}{t_f - t_i} \int_{t_i}^{t_f} F_{drag} dt, \tag{4.89}$$

where t_i is a time when the flow is first developed and t_f is the terminal time. For channel flow, F_{drag} tends to not vary a great deal in time, so this arbitrary time range makes little difference. We calculate the corresponding bulk drag coefficient by using the bulk drag equation (4.1):

$$\tilde{C}_d = \frac{2\bar{F}_{drag}}{\rho N_v b \bar{u}^2}. \tag{4.90}$$

4.5.1 Channel Flow Problem

4.5.1.1 Problem Setup

Our model channel is a 3D rectangular domain 4 m long, 0.4 m wide, and 0.368 m tall. We drive the flow by imposing an inflow velocity Dirichlet boundary condition on the inflow boundary. The inflow velocity is positive in the x-direction and zero for the y and z-directions. For velocity, we impose a no-slip condition on the channel bottom, a free surface condition on the top of

the channel, an outflow condition on the outflow boundary, and a no-flux condition on the front and back boundaries. For pressure, we impose a hydrostatic pressure condition on the outflow boundary. A standard acceleration due to gravity $g = 9.8$ m/s^2 is used. The water density used is $\rho = 998.2$ kg/m^3 and the kinematic viscosity is $\nu = 1.004 \times 10^{-6}$ m^2/s The slope of the domain is 0. We initialize the system with zero velocity and hydrostatic pressure everywhere and slowly ramp up the inflow velocity to the desired value $\bar{u}$. We then run the model out in time using second order backward differentiation formula (BDF) time integration and small time steps.

The model vegetation begins 1 m from the inflow boundary of the domain, so that the flow is able to fully develop before entering the vegetated area. The vegetation continues to the outflow boundary. To avoid boundary effects we calculate the net drag only in the center of the channel, the region $\tilde{\Omega}$ where

$$\tilde{\Omega} = [1.0, 4.0] \times [0.1, 0.3] \times [0, 0.368]. \tag{4.91}$$

4.5.1.2 Experimental Studies

Dunn et al. [23] conducted their experiments in a 19.5 m long, 0.91 m wide, 0.61 m deep slanted flume. The slope of the flume could be set between 0 and 10 percent. Water was introduced into the flume from a constant head tank to ensure a constant discharge, up to a maximum of around 180 L/s. The water flowed through a pattern of model vegetation in a pattern similar to that in Figure 4.11 and exited the flume into a large sump where it was

recirculated into the flume. For the experiments that we are comparing to the channel slope was set between 0.0036 and 0.0161. Rigid vegetation was simulated using 1/4 inch diameter wooden dowels 6 inches in length. Flexible vegetation was simulated by 1/4 inch diameter, 7 3/4 inch long plastic drinking straws. When placed onto a false floor the average height of the rigid dowels was 11.8 $\pm$ 1.67 cm and 16.9 $\pm$ 1.61 cm for the flexible straws. They tested the effect on the bulk drag coefficient with respect to several non-dimensional parameters: Reynolds number, Froude number, slope, ratio of stem diameter to height, and ratio of stem diameter to stem spacing. They did these studies for both rigid and flexible vegetation.

Nepf [73] conducted experiments in a 24 m long and 0.38 m wide glass-walled flume. The flow depth $H = 0.15$ m was always used. Vegetation was modeled by using 0.064 m diameter wooden dowels. The densities of the dowels varied between 200 to 2000 stems/m^2. This is the range of actual stem densities observed in nature by saltwater environments by Gambi et al. [29] and in freshwater environments by Kadlec [43]. The dowels were mounted to Plexiglass boards and randomly placed throughout the flume. The bulk drag coefficient was calculated over for various population densities in the the given range.

4.5.1.3 Results

We organized our channel flow computational experiments to mimic the geometry of the experiments by Dunn et al. [23]. For rigid and flexible

experiments, the beam length is 0.1968 m, the beam radius is 0.003175 m, the beam flexibility is $EI = 3.0 \times 10^{-4}$ Nm^2 for flexible vegetation, and the population density N_v is 172 stems/m^2. The standard mean horizontal velocity used is $U = 0.57$ m/s. The parameters listed here are the standard parameters. We ran several simulations holding all parameters but one constant and varying one to study the effects of that parameter on the bulk drag coefficient.

We see how the bulk drag coefficient varies with respect to four dimensionless quantities introduced by Dunn et al. [23]. The first quantity is the Reynolds number Re defined with the channel height H as the length parameter: $Re = UH/\nu$. This is a dimensionless measure of velocity. The second quantity is D_v/H where D_v is the stem diameter. Here we keep H constant and vary D_v. This is a dimensionless measure of obstacle thickness. The third quantity is HD_v/λ^2. We keep H and D_v constant and vary the spacing λ. This is a dimensionless measure of population density. The final quantity is h_v/H where we keep H constant and vary h_v. This is a non-dimensional measure of stem height.

Dunn et al. [23] introduce 2 versions of the bulk drag coefficient. The two versions differ depending on the vertical length over which the bulk drag coefficient is calculated. For $\tilde{C}_{dH}$ the vertical scale used in $\tilde{\Omega}$ is H the channel depth. For $\tilde{C}_{dh_v}$ the vertical scale used in $\tilde{\Omega}$ is h_v the stem height. Normally, we are interested mostly in $\tilde{C}_{dh_v}$, but to compare to their results we calculate both.

Figure 4.12 shows how the the four dimensionless parameters effect

the bulk drag coefficients for rigid and flexible vegetation. The bulk drag coefficients calculated by Dunn et al. [23] are much more scattered than ours. This difference is most likely due to error caused by them having to measure velocity information experimentally and calculate the drag coefficient with a model, whereas with our model, we can calculate the net drag force directly. While our results are not as scattered as theirs, the bulk drag coefficients are in the same ranges and have similar tendencies. The experimental results show $\tilde{C}_{dh_v}$ varying between 0.8 and 1.5 in all cases and usually being near 1.0. We see our calculations of $\tilde{C}_{dh_v}$ almost always being between 0.9 and 1.0. This matches up extremely well. The experimental calculations of $\tilde{C}_{dH}$ vary between 0.05 and 0.6, mostly being between 0.1 and 0.4. Our calculations are mostly near 0.5. Our method tends to calculate only slightly higher values of $\tilde{C}_{dH}$ than the experimental results.

The most noticeable pattern is that in all cases, the flexible vegetation resulted in slightly lower bulk drag coefficients. The experimental results also show this basic tendency. Also, the bulk drag coefficients tend to decrease slightly with increasing Reynolds number. Bent stem profiles for a range of Reynolds numbers are displayed in Figure 4.13. Our results also show the bulk drag coefficient being mostly constant with respect to changing obstacle diameter and height. Dunn et al. [23] also came to that conclusion. The steep slope of $\tilde{C}_{dH}$ due to changing length is due to how we calculate this value, and it does not indicate an increase in drag due to increased stem length. Finally, we see a general tendency for the bulk drag coefficient to decrease

as the population density is increased. Dunn et al. [23] also came to the conclusion that the bulk drag coefficient decreases with density. They found a slightly more pronounced relationship than our results show.

These results show that our immersed structure method for modeling flow through vegetated regions does a reasonable job at calculating bulk drag coefficients. Quantitatively, we see that we calculate $\tilde{C}_{dh_v}$ in a range that matches up extremely well with experimental results. Our calculations of $\tilde{C}_{dH}$ are only slightly higher than those from experiments. Qualitatively, our method predicts tendencies of the bulk drag coefficient to vary with respect to different parameters that was also seen by experiments. We show that the drag coefficients tend to decrease with increased velocity and with increased population density. Rigid obstacles tend to have higher bulk drag coefficients than flexible ones. Stem thickness and length do not have major impacts on the bulk drag coefficient. That our model captures these tendencies that have been observed in experimental settings serves to vindicate this model.

Nepf [73] only studies the relationship between population density and the bulk drag coefficient scaled with the vegetation height, $\tilde{C}_{h_v}$. As with the previous experiments, we reproduce the geometry of the staggered array of rigid dowels. We ran computational experiments with stem population densities ranging from 200 to 2000 stems/m^2, the range seen in nature, as mentioned before. The dimensionless quantity for population used for these experiments is $\frac{D_s^2}{\lambda^2}$, as in Nepf. Varying this dimensionless quantity from 0.003 to 0.3, we chose 10 values on a logarithmic scale. A mean inflow velocity of $U =$

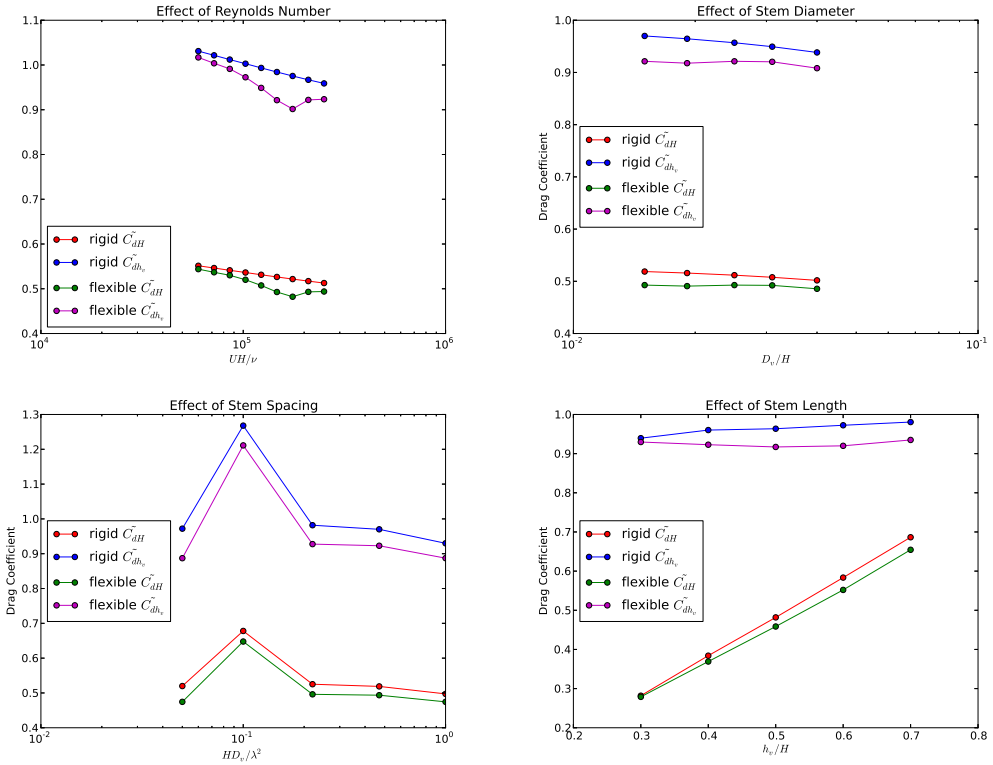

Figure 4.12: The effect of dimensionless values representing velocity, stem diameter, stem spacing, and stem length on the bulk drag coefficient for channel flow.

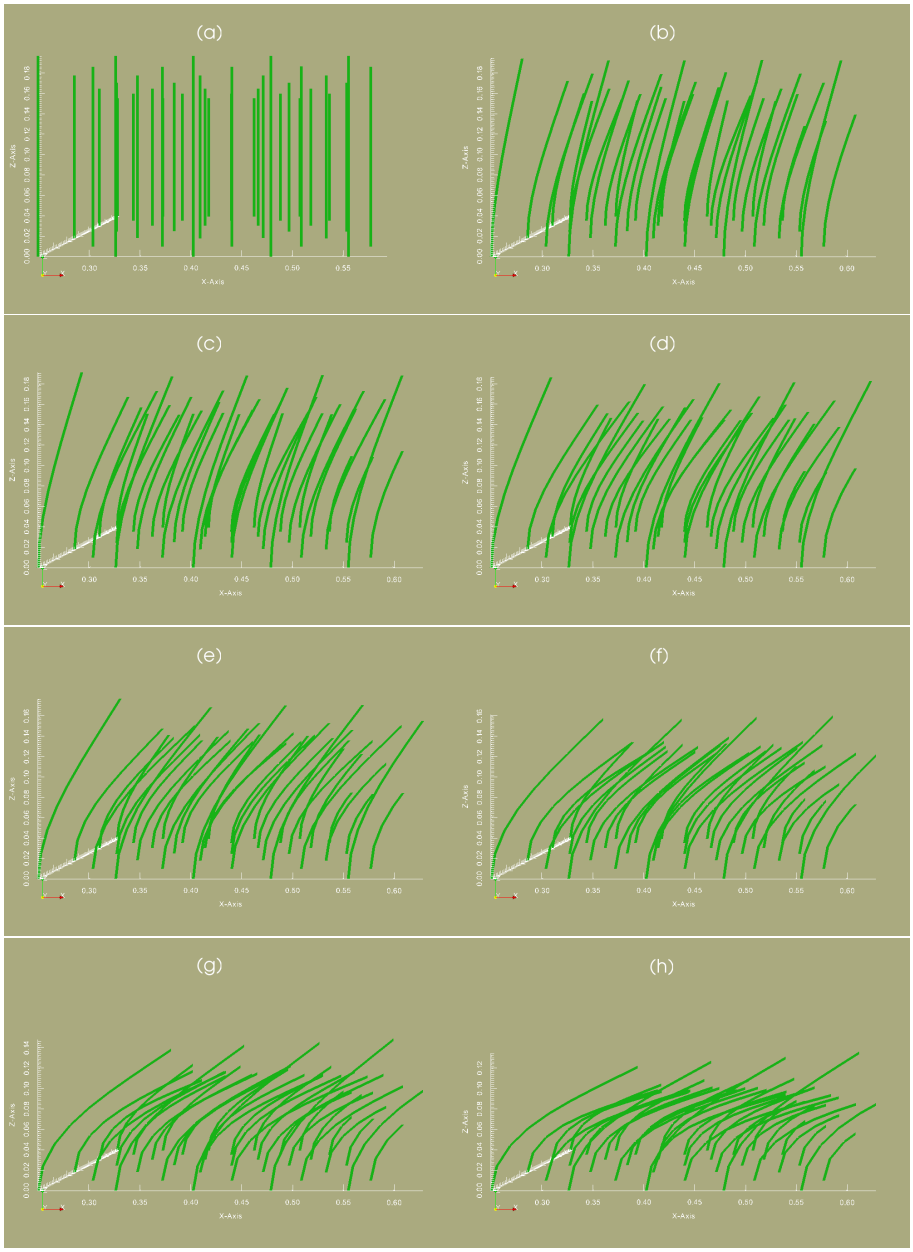

Figure 4.13: Bent vegetation profiles for channel flow of Reynolds numbers (a) 0, (b) 6.00×10^4, (c) 7.17×10^4, (d) 8.58×10^4, (e) 1.03×10^5, (f) 1.23×10^5, (g) 1.47×10^5, and (h) 1.75×10^5 respectively.

0.57 m/s was used in all cases. Figure 4.14 shows the relationship calculated between dimensionless population density and the bulk drag coefficient. These results match up exceptionally well with the experimental results. The range of population densities simulated here is much larger than those done when reproducing the experiments of Dunn et al. [23]. The decrease of the bulk drag coefficient with increased population density is much more pronounced over this range. As with the results from Nepf, for dimensionless population density, between 0.003 and 0.02 the bulk drag coefficient calculated is nearly constant near a value of 1.0. Higher than this population density, $\tilde{C}_{h_v}$ drops in a gradual arc with a shape very similar to the one from the experiments. For the highest population densities, $\tilde{C}_{h_v}$ reaches a value near 0.5. Nepf [73] saw a slightly lower value, closer to 0.4. The experimental results due to Nepf are highly cited and very well-respected. The results from that study are compared to and match up well with experimental results due to Seginer et al. [94], Kays and London [45], Petryk [79], and Zdravkovich [117]. The fact that the curve of bulk drag coefficient versus population density using our immersed structure method matches the curve from experimental results extremely closely does a great deal to verify our model. It shows that the immersed structure method captures the fact that the bulk effect of a dense packing of N vegetative obstacles is not equivalent to N times the effect of one vegetative obstacle. The more densely the stems are packed past a certain threshold, each stem has less of a drag effect on the flow.

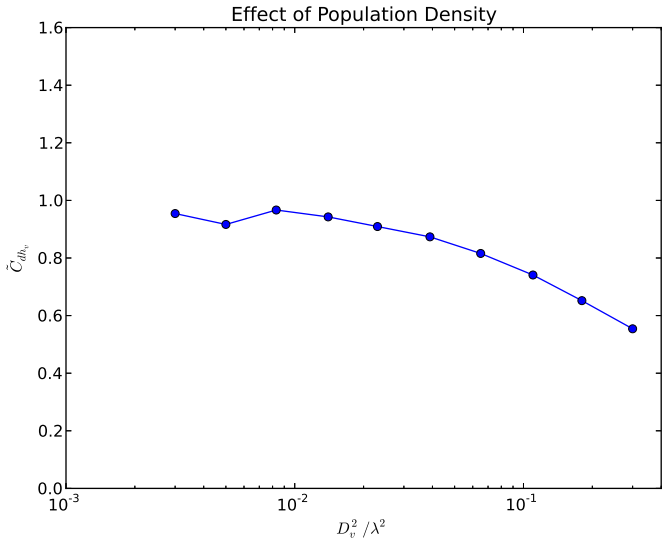

Figure 4.14: The relationship between population density of stems and the bulk drag coefficient.

4.5.2 Wave Tank Problem

4.5.2.1 Two-Phase Flow Method

To implement a wave tank problem, we used a two-phase flow method. We use a conservative level set method presented by Kees et al. [46]. This method is designed for free-surface flow computations with complex phenomena like waves. It uses standard level set methods with additional discrete conservation properties. The flow model is the same LES model as discussed in Section 2; however, now instead of one incompressible fluid with density ρ and kinematic viscosity ν, we have a water phase with density ρ_w and viscosity ν_w and an air phase with density ρ_a and ν_a. We take $\rho_a = 1.205$ kg/m^3 and $\nu_a = 1.5 \times 10^{-5}m^2/s$. The water parameters are the same as in the channel

problem. The boundary between the air and water phase, Γ is represented by the zero level set of a function ϕ, i.e.

$$\Gamma = \{\mathbf{x}|\phi(\mathbf{x} = 0\}. \tag{4.92}$$

As with standard level set methods, the interface evolution is described by the level set equation:

$$\frac{\partial \phi}{\partial t} + \mathbf{v} \cdot \nabla \phi = 0, \tag{4.93}$$

where $\mathbf{v}$ is the fluid velocity. The water lies in the region

$$\Omega_w = \{\mathbf{x}|\phi(\mathbf{x}) < 0\}, \tag{4.94}$$

and the air lies in the region

$$\Omega_a = \{\mathbf{x}|\phi(\mathbf{x}) \geq 0\}. \tag{4.95}$$

Using the method formulated by Kees et al. [46], (4.93) is coupled with a volume fraction equation, a redistancing equation, and a level set mass conservation equation creating a conservative method. The resdistancing step solves an eikonal equation which makes ϕ be a signed distance function. The density and viscosity near the interface are made continuous by using a regularized Heaviside function

$$H_\epsilon(\phi) = \begin{cases} 0 & \phi \leq -\epsilon \\ \frac{1}{2}\left(1 + \frac{\phi}{\epsilon} + \frac{1}{\pi}\sin\frac{\phi\pi}{\epsilon}\right) & |\phi| < \epsilon \\ 1 & \phi \geq \epsilon \end{cases} \tag{4.96}$$

where ϵ is a small parameter. We take ϵ to be 1.5 times the fluid element diameter. Thus, ρ and ν are defined by

$$\rho = \rho_w H_\epsilon(\phi) + \rho_a(1 - H_\epsilon(\phi)), \tag{4.97}$$

and

$$\nu = \nu_w H_\epsilon(\phi) + \nu_a(1 - H_\epsilon(\phi)). \tag{4.98}$$

It is important to note that ρ as defined above is the one used in the drag calculations.

4.5.2.2 Linear Plane Wave Theory

The wave tank experiments by Wu et al. [115] that we reproduce computationally use a paddle wavemaker. Let S be the stroke of the paddle, T be the period of the wave being generated, L be the wavelength of the wave generated, and $k = 2\pi/L$ be the wavenumber. Suppose the height of the undisturbed wave tank is h and the z coordinate is zero at this height. Suppose the wave amplitude is A. For progressive waves, the wavemaker frequency σ is defined by

$$\sigma^2 = -gk \tan kh \tag{4.99}$$

where $g = -9.8$ m/s^2 is the gravitational constant. The wave period is $T = 2\pi/\sigma$. Let η be the wave height as a function of position and time and $\boldsymbol{\xi}$ be the velocity function. The governing equation for a linear plane gravity wave in the x-z plane is the Laplace equation

$$\frac{\partial^2 \psi}{\partial x^2} + \frac{\partial^2 \psi}{\partial z^2} = 0, \tag{4.100}$$

where ψ is the velocity potential. The dynamic and kinematic free surface boundary conditions are

$$\eta = \frac{1}{g}\frac{\partial \psi}{\partial t} \quad z = 0, \tag{4.101}$$

$$-\frac{\partial \psi}{\partial z} = \frac{\partial \eta}{\partial t} \quad z = 0, \tag{4.102}$$

respectively. The bottom boundary condition is a no-flow condition:

$$-\frac{\partial \psi}{\partial z} = 0 \quad z = -h. \tag{4.103}$$

The linearized lateral boundary condition is

$$\xi_1(0, z, t) = \frac{S(z)}{2}\sigma \cos \sigma t. \tag{4.104}$$

Using standard plane wavemaker theory as presented by Dean and Dalrymple [20], the analytical solution to the Laplace equation with the given boundary conditions gives

$$\eta(x, t) = A \cos(kx - \sigma t), \tag{4.105}$$

$$\xi_1(x, z, t) = \frac{-gkA}{\sigma}\frac{\cosh(k(z + h))}{\cosh(kh)} \sin(\sigma t - kx), \tag{4.106}$$

$$\xi_2(x, z, t) = 0, \tag{4.107}$$

$$\xi_3(x, z, t) = \frac{-gkA}{\sigma}\frac{\cosh(k(z + h))}{\cosh(kh)} \cos(\sigma t - kx). \tag{4.108}$$

4.5.2.3 Model Setup

We use the above plane wave theory to set the initial conditions and boundary conditions for our two-phase flow method. The wave tank domain that we use is shown in Figure 4.15. The tank consists of a rectangular section with a wedge section on the end. Let the rectangular section have the dimensions $L_1 \times L_2 \times L_3$. The wedge section is an absorbing region that completely dampens out the wave to prevent reflections off the right boundary. Given a

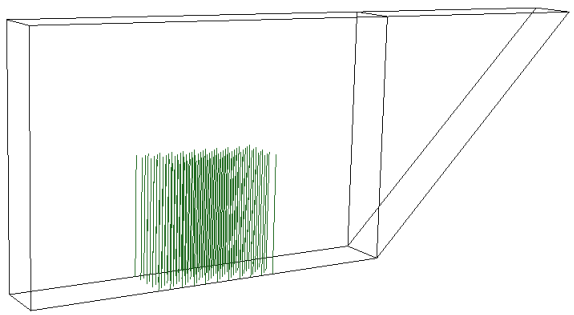

Figure 4.15: Domain for the wave tank problem.

wave amplitude A, wavelength L, and initial mean flow height h, the level set function ϕ has the initial condition

$$\phi_0(x, y, z) = z - h + \eta(x, 0) \tag{4.109}$$

the velocity initial conditions are set by

$$\mathbf{v}_0(x, y, z) = \boldsymbol{\xi}(x, z - h, 0)(1 - H_\epsilon(\phi)), \tag{4.110}$$

and the pressure initial condition is hydrostatic:

$$p_0(x, y, z) = \rho g z. \tag{4.111}$$

The continued propagation of this plane gravity wave is forced by a Dirichlet boundary condition on the left inflow boundary of the wave tank domain. This condition is

$$\mathbf{v}(0, y, z, t) = \boldsymbol{\xi}(x, z - h, t)(1 - H_\epsilon(\phi)). \tag{4.112}$$

A hydrostatic pressure Dirichlet condition is imposed at the top of the domain. A no-flux condition is imposed on all other boundaries. In the wedge on the far right of the wave tank domain, a large momentum sink term is imposed. This term is large enough to almost completely dampen out the wave before hitting the right boundary. This minimized the reflection of the waves back through the tank. This is designed to mimic the wave absorbers used at the end of the tanks used by Wu et al. [115].

The wave tank domain used for simulations had length $L_1 = 4.5$ m, width $L_2 = 0.69$ m, and height $L_3 = 1$ m. The vegetated area began at

$x = 0.5$ m, and the wave absorbing wedge began at $x = 3.5$ m. The area between these lengths is filled with vegetative obstacles. All wave simulations were done holding the wavelength $L = 2.0$ m constant. The experiments done by Wu et al. [115], use variable wavelengths, but the values they used are all close to this. We ran many simulations with each type of vegetation for different wave amplitudes and several mean heights. In order to get an accurate mean bulk drag force calculation, we run several waves through the vegetated bed. When calculating $\bar{F}_{drag}$ with (4.89), it is essential that t_f and t_i occur at the same place in the wave period, i.e. $\frac{t_f - t_i}{T}$ is an integer.

4.5.2.4 Experimental Setup

As mentioned numerous times, our computational wave tank setup is designed to model an experimental study by Wu et al. [115]. Their experimental setup included a 20.6 m long, 0.69 m wide, 1.22 m tall wave flume. A paddle wave generator created regular and irregular gravity waves on one end, and a porous, parabolic wave absorber was placed on the opposite end to minimize reflections. They performed studies with flat and slanted bottoms. We are only concerned with the flat-bottom experiments for now. Between the lengths of 12.9 m and 16.56 m arrays of model vegetation were arranged in a pattern exactly like that in Figure 4.11. They utilized several types of model "vegetation" of which we focus on four. The first is a rigid vegetation type using wooden dowels similar to the channel flow studies by Dunn et al. [23] and Nepf [73]. These dowels have a diameter of 9.4 mm and are 0.48 m

tall. They are spaced with $\lambda = 57.4$ mm, with the corresponding population density $N_v = 350$ stems/m^2. Second, their flexible "vegetation" consists of Ethylene propylene diene monomer (EPDM) foam rubber cylinders, also with a diameter of 9.4 mm and height of 0.48 m. The spacing and density are the same as the rigid model as well. These foam hoses have a density of 368 kg/m^3 and Young's modulus $E = 4$ MPa.

The last two types of model vegetation are real beds of *Spartina alterniflora*, an extremely common type of coastal marsh grass. One of the beds of grass is dormant and one is green. The plants were grown in an outdoor nursery and transported to the experimental facility. The stem density was determined to be $N_v = 545$ stems/m^2 for the dormant grass and $N_v = 405$ stems/m^2 for the live grass.

We model the rigid vegetation in the same manner as in the channel flow, using the immersed structure method without allowing bending. The foam rubber hose is modeled as flexible cantilever beams with the fully non-linear beam solving method. Young's modulus, E, is known and the second moment of area is that of a circular cylinder $I = \frac{\pi}{2}r^4 = 7.66 \times 10^{-10}\ m^4$. We space the stems in the same manner as with the channel flow, using the value of λ shown in Figure 4.11.

To model the real vegetation, we also model each plant as a flexible cantilever beam. For the parameters describing the stem we use experimental data from Wu et al. [115]. They found that for dormant and green grass, a

good approximation for the modulus of elasticity is

$$E = 183204 \left(\frac{h_v}{D_v} \right)^{1.773}, \tag{4.113}$$

where D_v is the vegetation diameter, h_v is the vegetation height, and the units for E are N/m^2. Different values were found by Hessini et al. [35]. Wu et al. [115] also measured other parameters. Samples of *Spartina alterniflora* were taken from field locations in Louisiana and Mississippi, and stem height, length, density, and plant volume were measured for each stem. They give mean values and standard deviations for stem diameter and height. We calculate a truncated normal distribution based on the mean, standard deviation, maximum, and minimum values. We chose a truncated normal distribution rather than a normal distribution because the outliers of the normal distribution were physically unrealistic. Figure 4.16 shows the probability density functions for stem length and radius for dormant *Spartina alterniflora*, and Figure 4.17 gives the same information for green *Spartina alterniflora*. The mass density for all *Spartina alterniflora* was close to 610 kg/m^3 so that value was chosen for all stems.

Using (4.87), and the known population densities N_v for the real vegetation, we calculate the spacing λ. We arrange the plants in our standard array pattern with this spacing. For each stem in the array, we choose a radius and length from the probability distributions presented above. We use the radius to calculate the second moment of area I. Hence, this provides us with a bed of vegetation that is somewhat representative of a real bed of *Spartina alterniflora*.

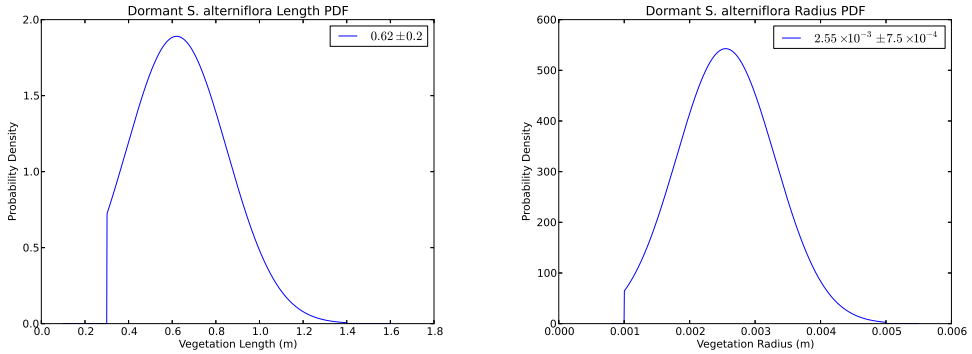

Figure 4.16: Length and radius probability density functions for dormant *Spartina alterniflora*.

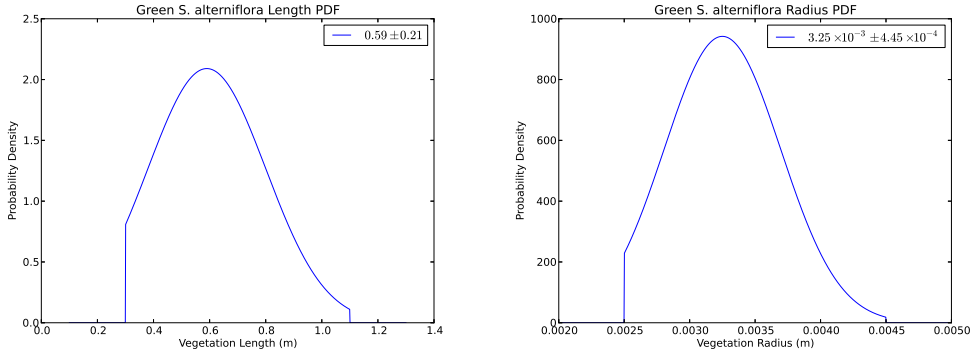

Figure 4.17: Length and radius probability density functions for green *Spartina alterniflora*.

4.5.2.5 Results

As with the channel flow problems we only calculate the drag force F_{drag} over the center of the domain to avoid boundary effects. We used a highly-refined unstructured tetrahedral mesh. The maximum element diameter allowed is 0.025 m. The resulting meshes contain approximately 2 million elements. We run at least 5 waves through the vegetated part of the domain and time average to calculate the mean drag force $\bar{F}_{drag}$ and then the bulk drag coefficient $\tilde{C}_d$. For these simulations, the vertical length scale for the region over which the calculation of the bulk drag is performed is the mean undeflected vegetation height h_v. Therefore it is similar to $\tilde{C}_{dh_v}$ presented in the channel flow section.

The average velocity $\bar{u}$ used in calculating the bulk drag coefficient with (4.1) is the time-averaged, depth-averaged, magnitude of the horizontal velocity. This is calculated analytically as

$$\bar{u} = \frac{1}{4} A \frac{\sqrt{-g}}{h}, \tag{4.114}$$

where A is the wave amplitude and h is the mean water depth. The Reynolds number Re is defined using the mean stem diameter D_v as a length scale and the maximal horizontal velocity just before the vegetation zone at mid-height of the plants

$$u_c = A\sigma \frac{\cosh(ka^* h)}{\sinh(ka^* h)}, \tag{4.115}$$

where a^* is h_v/h for submerged vegetation and unity for emergent vegetation.

Therefore,

$$Re = \frac{u_c D_v}{\nu_w}. \tag{4.116}$$

For each type of model vegetation, simulations were run for three different mean water depths. For the rigid and model flexible vegetation, these depths were 0.4 m, 0.5 m, and 0.6 m. This includes one emergent vegetation example, one submerged vegetation example, and one example where the water depth is nearly the unbent vegetation height. For the cases modeling real vegetation depths of 0.5 m, 0.6 m, and 0.7 m were used, also giving one emergent vegetation example, one submerged vegetation example, and one example where the water depth is nearly the unbent vegetation height. We plot calculated bulk drag coefficients using our immersed structure method for specific Reynolds numbers for the 3 different depths and a curve fit for the results due to Wu et al. [115].

Figure 4.18 shows the results for the rigid vegetation model. The curve fit to the SERRI data was calculated in the report as

$$\tilde{C}_d = 2.557 + (565/Re)^{3.284}.$$

We see that for very low Reynolds numbers, we underestimate $\tilde{C}_d$. This is most likely because we are using $C_d = 1.2$ for the drag coefficient of a single beam in the immersed structure model. For Reynolds numbers this low, this is probably a smaller value of C_d than what is realistic in nature, causing our method to result in a lower value for the drag coefficient. Around a Reynolds number of 500 and higher, our results match up very closely to the experimental results.

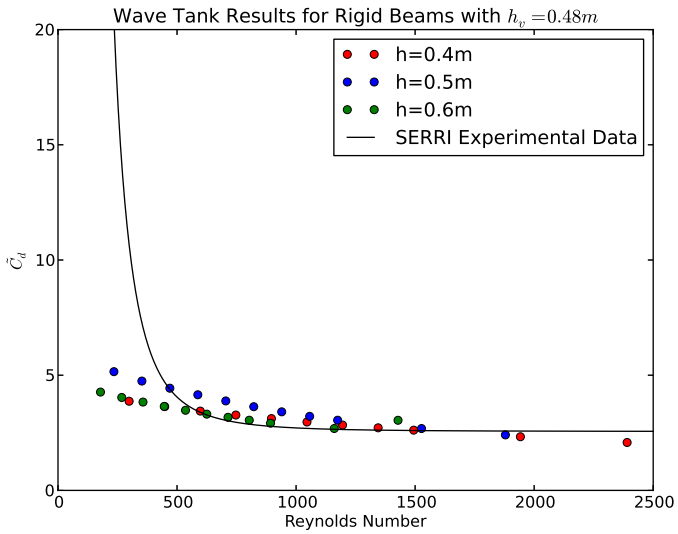

Figure 4.18: Bulk drag coefficient values for rigid vegetation setup compared to Wu [115] results.

We capture the gradual decrease with respect to Re that they observed, with a similarly shaped dip. As with the the experimental results, we see $\tilde{C}_d$ begin to level off near Reynolds number 1500. Past that we calculate slightly lower values than them; although, their is a large spread to their data in that range. It appears that from these results that mean flow depth does not have a major impact on the bulk drag coefficient.

Figure 4.19 shows a time series of a wave traveling through a bed of model flexible vegetation. Notice how our immersed structure method captures the complex bending back and forth that occurs as a water wave travels through the domain. Figure 4.20 shows the bulk drag coefficient results for the foam rubber model flexible vegetation model. The curve fit to the SERRI

data was calculated in the report as

$$\tilde{C}_d = (4020/Re)^{0.851}.$$

As with the rigid model, we underestimate the bulk drag coefficient greatly for very small Reynolds numbers. The explanation for this is probably the same as for the rigid vegetation. Around a Reynolds number of 400, our calculations begin to match up exceedingly well with the experimental results. We capture the decreasing slope with increasing Reynolds number. Our data points stay almost exactly on the best fit curve for the experimental results up until a Reynolds number of nearly 2500. That our calculations match up so closely to experimental results for such a complicated problem is incredibly exciting. This does much to verify our proposed method of modeling flexible vegetation for calculating the bulk drag coefficient. Once again, it appears that from these results that mean flow depth does not have a major impact on the bulk drag coefficient for flexible vegetation.

Our results for the models approximating real *Spartina alterniflora* stems were not nearly as good as those for the rigid and flexible model vegetation. For both the model dormant and green grass, we greatly underestimated $\tilde{C}_d$ for low Reynolds numbers as with the other models. The model dormant *Spartina alterniflora* data matches the experimental data relatively well starting near a Reynolds number of 500. The curve fit to the SERRI data was calculated in the report as

$$\tilde{C}_d = (2623/Re)^{1.013}.$$

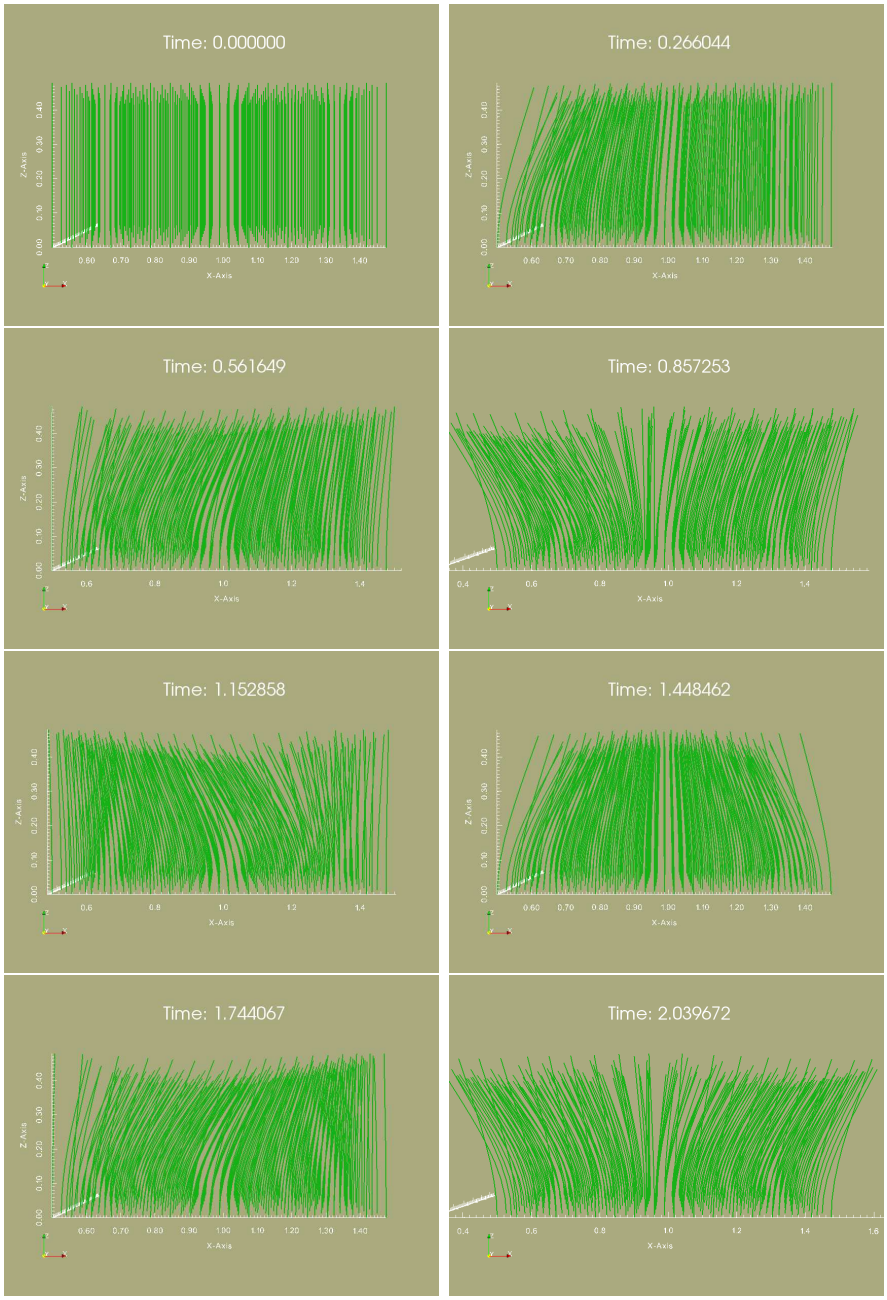

Figure 4.19: A wave traveling through a bed of model flexible vegetation.

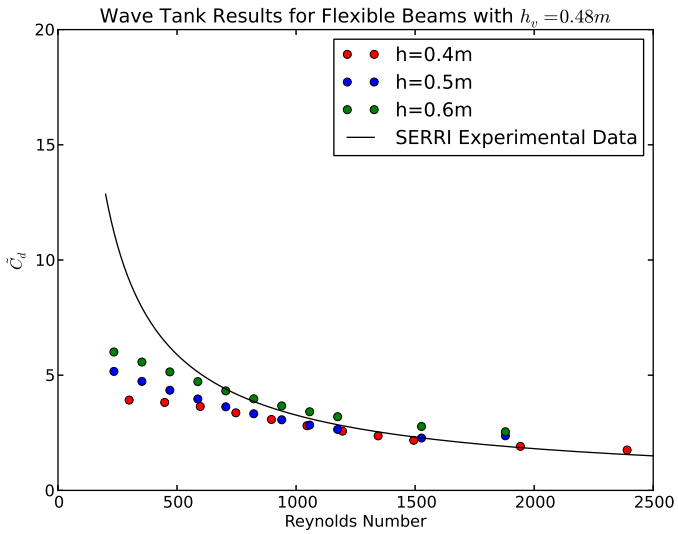

Figure 4.20: Bulk drag coefficient values for flexible vegetation setup compared to Wu [115] results.

From our data, we see $\tilde{C}_d$ leveling off here and becoming almost constant. The experimental data shows $\tilde{C}_d$ continuing to decrease slightly for higher Reynolds numbers. Still, considering how much the experimental results vary over this range, our data is not a terrible fit. Our model is a reasonable approximation of dormant *Spartina alterniflora* above a Reynolds number of 450 or 500. The flow depth appeared to have more of an effect here than in the other simulations.

Our model did not do a particularly good job of capturing the drag effects of live, green *Spartina alterniflora*. While we capture the slight decrease in $\tilde{C}_d$ with increasing Reynolds number, we greatly underestimate its value over the entire range. The curve fit to the SERRI data was calculated in the report

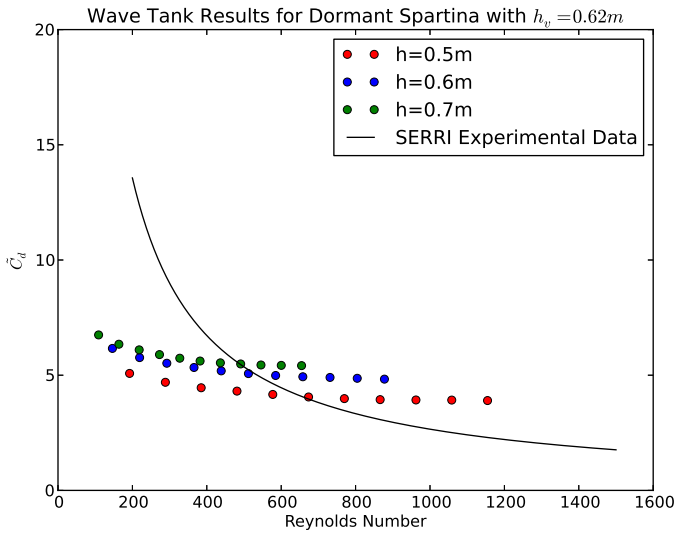

Figure 4.21: Bulk drag coefficient values for dormant *Spartina alterniflora* vegetation setup compared to Wu [115] results.

as

$$\tilde{C}_d = (6067/Re)^{1.3}.$$

In the report explaining the experimental data, the drag coefficients are much higher for green *Spartina alterniflora* than for any other type of model vegetation, and we were unable to capture this.

It is not surprising that our model did not perfectly capture the drag effects of tightly packed real vegetation. Our model beds of vegetation are imperfect and do not capture the geometry perfectly. Also, there are a great deal of parameters that go into the bending model, and these all had to be estimated from empirical relationships. Still, we were able to model the bulk drag coefficient for dormant *Spartina alterniflora* relatively well given these

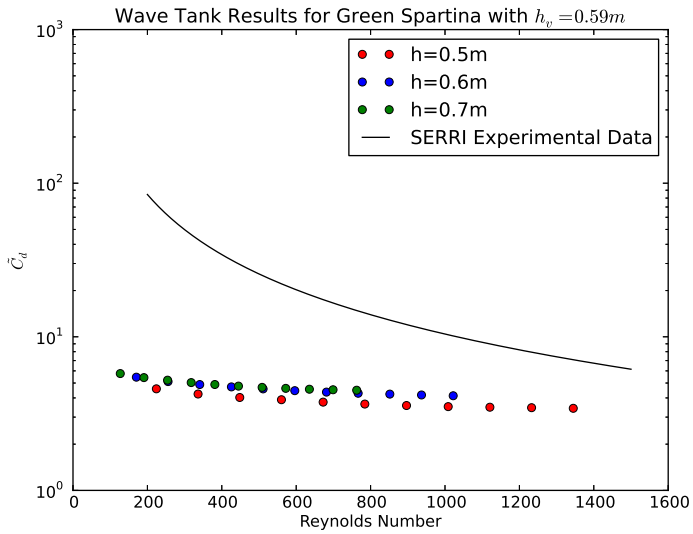

Figure 4.22: Bulk drag coefficient values for green *Spartina alterniflora* vegetation setup compared to Wu [115] results.

imperfect modeling techniques.

For the types of model vegetation where we could capture the geometry and parameters exactly, the rigid vegetation and foam rubber flexible vegetation, we did an exceptional job at calculating the bulk drag coefficients at Reynolds numbers above around 600. If a different drag coefficient for a single beam was used for low Reynolds numbers, perhaps, the immersed structure method presented here could capture the drag effects for lower Reynolds numbers as well. The motion of flexible structures in a wave tank is incredibly complex, and our method has done a good job at capturing the motion and its effect on drag.

Chapter 5

Conclusions and Discussion

5.1 Conclusions

In the previous chapters we have presented two methods for modeling incompressible flow through vegetated domains. The first method requires one to completely resolve the geometry of the vegetation on one finite element mesh. A high-resolution locally conservative stabilized finite element method is utilized to calculate the flow field through the domain due to a specified hydraulic gradient. The drag due to the form of the vegetative obstacles is imposed on the flow by imposing the standard no-slip condition on the boundary with the obstacle. The corresponding drag coefficient for a periodic cell filled with vegetative obstacles is calculated by solving an LES cell problem and using a volume averaging technique. The drag coefficient of the vegetated periodic cell is highly dependent on the cell geometry and the flow velocity. We notice that the vegetated domain is a porous medium, similar to those that are commonly studied in the modeling of subsurface flow. We parametrize the drag coefficient of the periodic vegetated cell for a large range of Reynolds numbers using Darcy and non-Darcy upscaling laws. Non-Darcy laws are used to upscale high-velocity inertial flows through the porous domain. We find that using our upscaling technique that the common quadratic

Darcy-Forchheimer law and a general power law are good upscaled models for matching highly-resolved LES simulations. However, the non-Darcy parameters in these upscaling laws are highly sensitive to the range of flows over which they are calculated. If one is to use these laws to parametrize the cell drag coefficient, they must make sure that the range of Reynolds numbers over which they expect their flow to reach is included in the high-resolution LES simulations that are performed to calculate the non-Darcy parameters.

The second method that we present for modeling flow through vegetated regions is designed to handle larger-scale and much more complicated domains. The fully-resolved method above requires stem-scale resolution of the flow domain. This extremely high resolution greatly limits the scale of domain of interest to one that only contains a few pieces of vegetation. It also requires the vegetative obstacles to be rigid which is an unrealistic assumption for many common types of coastal vegetation. Allowing flexibility in that model would introduce a level of computational complexity that would be extremely difficult to handle, even at the small scale.

The immersed structure approach presented here works for larger-scale, more complicated vegetated domains. While the first method works on the scale of a few plants, this method can be applied to thousands and probably millions of plants. Rather than fully resolving the vegetative obstacles on one fluid finite element mesh and imposing a no-slip condition to induce the drag, an immersed boundary approach is used. Separate fluid and structure meshes are used in their natural Eulerian and Lagrangian frameworks, respectively.

The vegetative obstacles are modeled as long, thin inextensible flexible cantilever beams. Classical Euler-Bernoulli beam is used in the beam model. Two numerical methods are developed for solving the beam model. One is a fully nonlinear finite element method that finds stable minima of the beam energy functional using Newton's method. The global minima of this functional is the correct static state for the beam system. The second method is a linearized finite element method that uses Picard iterations to solve the Euler-Lagrange equations of the beam energy functional. These equations are exactly the equations for the balance of moments and forces in an elastic beam. We found that combined with incremental loading that the fully nonlinear method is incredibly robust for finding stable equilibria for beam systems under loads that cause large deflections. Using between 5 and 10 incremental loading steps required the fewest total iterations. The linearized method is much cheaper computationally than the nonlinear method per iteration. For loads causing relatively small deflections, especially end loads, it provided results just as accurate as the nonlinear method but for a lower computational cost. However, for loads causing moderate and large deflections, the linearized method has a tendency to take an extremely large number of iterations to converge and also to diverge or converge to unstable extrema. Therefore, we found for most cases the fully nonlinear beam solver to be the best method to use.

We couple the fluid-structure system using an immersed boundary approach. Our main objective was to calculate and parametrize the bulk drag of many immersed structures on a fluid region. The standard drag equation

is used to calculate the drag force on the fluid by the immersed structures. As is the standard with immersed boundary methods, integral transforms involving approximations to the Dirac delta are used to map between the fluid and structure domains. In a method that conserves momentum, the momentum loss due to this drag force enters the fluid model as a local sink term. The corresponding distributed load on the structure due to the drag is applied to the beam model. A fully coupled steady-state fluid-structure interaction method is formulated. A dynamic method which will be our main tool is also developed. This involves a fully dynamic LES fluid model and a quasi-static beam model.

The dynamic fluid-structure interaction model was used to model two complex flow scenarios. The first is channel flow containing many rigid or flexible vegetative obstacles. We calculated bulk drag coefficients for these flows that were in the same range as those calculated from laboratory experiments. We also captured trends that were noticed from experimental results. These trends are that the bulk drag coefficient tends to decrease with increased Reynolds number and with increased population density. Flexible vegetative obstacles cause less bulk drag than rigid vegetative obstacles of the same dimension. Also, we found that the obstacle thickness and length have no major effect on the bulk drag coefficient which was also found by experiments. These findings match those from well-respected experimental data.

The second flow scenario was that of a wave tank. The drag due to vegetation has a large impact on wave attenuation in coastal regions. Using

a two-phase flow method with a conservative level set method used to track the water-air interface, we computationally modeled a wavemaker that makes linear plane waves and allows them to propagate through a flume. Inside the flume, we placed rigid vegetation, model flexible vegetation made of foam rubber with known parameters, and approximations of real vegetation. By averaging over several wave periods and using several wave amplitudes and water heights, we calculated bulk drag coefficients for the wave tank setup for large ranges of Reynolds numbers. For the rigid vegetation and model flexible vegetation, our calculated bulk drag coefficients match up exceedingly well with experimental data. For the approximations of real vegetation, we captured the main trend of the bulk drag coefficient to decease with increasing Reynolds number, but were slightly off in magnitude. This discrepancy is most likely due to the inaccuracy of our method at approximating a real bed of vegetation and error in the measurements that we used to make this approximation.

5.2 Moving To Larger Scale

We have developed two methods for simulating flow through vegetated regions at the small-scale and the meso-scale. Both of these methods provide drag coefficients that capture the drag effects of a larger vegetated region. The largest length scales where the methods presented here could be used to model flow through vegetation directly is tens of meters. The expense of resolving each stem individually, even with the immersed structure method, becomes too high at scales larger than that. However,the parametrizations of the drag

coefficient of flows through these smaller regions can be applied to larger scale simulations.

The first method, which requires resolving all of the geometry of the vegetation provides cell drag coefficients for each vegetated cell. This drag coefficient is a function of the vegetation geometry and Reynolds number and can accurately be parameterized over a range of Reynolds number using non-Darcy laws. In a large-scale simulation the calculated drag coefficient tensors $\mathbf{C}_d$ can be used to add a momentum sink term to the large scale flow equations modeling the momentum loss to drag. The sink term would be of the form

$$\mathbf{F} = -\frac{1}{2}\rho A|\mathbf{v}|\mathbf{C}_d(\mathbf{v})\mathbf{v}. \tag{5.1}$$

The sink term would be applied to the large-scale momentum equations in the region containing the geometry of the cell for which $\mathbf{C}_d$ was calculated. The results could be verified by comparing to experimental results by Tsujimoto et al. [104].

The bulk drag coefficient calculated using the immersed structure method can easily be applied to larger scale problems. It is important to note that the bulk drag coefficient is highly dependent on the flow velocity, the population density of the vegetation, and the type of flow. We have seen that the bulk drag coefficients for channel flow are much smaller than those for wave tank flows. We have also presented two different scalings for the bulk drag coefficient, $\tilde{C}_{dH}$ and $\tilde{C}_{dh_v}$, scaled by the flow depth and the average vegetation height respectively. For 3D large-scale problems, the drag force per unit

volume could enter as a sink term of the form

$$\mathbf{f} = \frac{1}{2}\tilde{C}_{dH}\rho b N_v \mathbf{v}|\mathbf{v}| \tag{5.2}$$

everywhere in the horizontal domain containing the vegetation that corresponds to $\tilde{C}_{dH}$. In a perhaps better model, the drag due to vegetation would only be applied below the vegetation height:

$$\mathbf{f} = \begin{cases} \frac{1}{2}\tilde{C}_{dh_v}\rho b N_v \mathbf{v}|\mathbf{v}| & z \leq h_v \\ 0 & z > h_v. \end{cases} \tag{5.3}$$

Most commonly, for large-scale simulations, 2D depth-averaged flow models are used. One way that the drag due to vegetation could be modeled in this scenario is with a depth integrated version of (5.2) where $\mathbf{v}$ is replaced by the depth-averaged velocity. As discussed by Westerink et al. [109], generally for these large-scale 2D models, the drag due to vegetation is incorporated into the bottom friction term

$$\tau_* = C_f[(U^2 + V^2)^{1/2}/H] \tag{5.4}$$

where τ_* is the bottom friction , C_f is the nonlinear bottom friction coefficient, H is the water depth, and U and V are the depth averaged horizontal velocities. C_f is commonly defined using Manning's n:

$$C_f = g\frac{n^2}{H^{\frac{1}{3}}}. \tag{5.5}$$

This idea was proposed by Ree and Palmer [87]. Usually the value of Manning's n is based on extremely general land use descriptions and it incorporates both

bottom friction and the form drag due to vegetation. Manning's equation is the proper model for bottom friction, but it is not the proper model for form drag. However, since it often provides good results for large-scale flow simulation the effect of form drag due to vegetation is often incorporated in this method of ramping up the bottom friction parameter to incorporate the form drag. This is discussed in depth by Wamsley et al. [108].

Recently a method has been developed by Wu [114] to directly incorporate the bulk drag coefficient due to vegetation that we have discussed in this dissertation into Manning's n. Where n_b is the bottom roughness the model is

$$n^2 = n_b^2 + \frac{1}{2g(1-c_{v0})}\tilde{C}_d N_v A_v \eta_v^2 \min(\frac{h_v}{h}, 1.0) R_s^{1/2}, \tag{5.6}$$

where c_{v0} is a known parameter, η_v is a coefficient of about 1.0 introduced by Stone and Shen [100], A_v is the frontal area of the vegetation, and R_s is the hydraulic gradient. (5.6) builds off of a model originally proposed by Petryk and Bosmajian [79] where they modeled flow through mangroves by increasing Manning's n based on stem population densities and thicknesses. Other work using these types of Manning's n models incorporating the bulk drag effects with mangroves has been done by Wolanski et al. [113], Mazda et al. [66], and Furukawa et al. [28]. Drag coefficients calculated using the methods presented here could be incorporated into a Manning's n model of this type relatively easily allowing it to be used for large-scale 2D simulations like those done using the Advanced Circulation (ADCIRC) model [63].

5.3 Further Work

There is a great deal of future work to be done in the modeling of flow through vegetative regions. Incorporating the drag coefficient calculations presented in this dissertation into large-scale 2D and 3D simulations as discussed in the previous section is an obvious direction for future work. These large-scale methods can be used to model important flows in riverine and coastal regions. These areas are of utmost importance for a variety of environmental, industrial, economic, and defense applications. In these areas, small-scale effects, including the effect of drag due to vegetation play a large role in determining large-scale flow characteristics. If the methods for quantifying vegetative drag presented here, which we have shown to be accurate, can improve larger-scale models it would be an important contribution to the field of hydrology.

In this dissertation, we have mostly discussed vegetation interacting with incompressible flows through drag effects. Drag surely is the effect that has the greatest effect on mean flow; however, vegetation also greatly impacts other flow processes including wave attenuation, turbulence, diffusion, and transport. We have already discussed the effect of vegetation on the attenuation of waves, but only with simple linear waves. There is a great deal of possible work to be done studying the effect of vegetation on breaking waves and other more complicated wave phenomena. Most work in this area has been theoretical or experimental, but we have shown that computational methods can be used to model complex physical processes such as these.

The existence of vegetation in a high-velocity flow greatly increases the production of turbulence. We have utilized a large eddy simulation flow model in our calculations in order to capture some of the effects due to this wake production. Nepf et al. [74] and Burke and Stolzenbach [11], show that even for sparsely populated vegetation, turbulence production due to vegetation is greater than that due to bed shear. Assuming that the energy leaving the mean flow due to drag becomes turbulent kinetic energy, then the production of turbulent kinetic energy is

$$P = \frac{1}{2}\tilde{C}_d N_v D_v U^3. \tag{5.7}$$

According to Tennekes and Lumley [101], the corresponding dissipation of turbulent kinetic energy scales like

$$\epsilon \sim k^{3/2}/D_v, \tag{5.8}$$

where k is the turbulent kinetic energy. Using these observations, our calculations of $\tilde{C}_d$ could be highly useful in modeling turbulence due to vegetation. It could also be seen if using our resolved pore-scale and immersed structure methods are successful in capturing turbulent stress profiles in the flow. These types of studies have been done in flume experiments by Nepf and Ghisalberti [72], Wilson et al. [110], Dunn et al. [23], and Järvelä [41] and computational experiments by Li and Xie [54] and Erduran and Kutija [25].

Within a flow through a vegetated domain, diffusion can be separated into turbulent diffusion and mechanical diffusion. Turbulent diffusion is diffusion caused by turbulence. As discussed previously, vegetation in a flow

greatly increases the production of turbulence, so it also greatly affects turbulent diffusion. Mechanical diffusion is commonly studied with respect to flow through porous media. According to Nepf [73], it concerns the dispersal of fluid particles because of the complex flow paths due to the porous nature of the domain. As we have shown, a vegetated region is a type of porous structure, so mechanical diffusion is a concern in these regions. Our models could likely be applied to study these diffusion processes.

When studying flow processes it is ubiquitous to also study transport phenomena that occur within that flow. Transport through a vegetated region is an extremely complex process the study of is one for which there is room for a great deal of new research. Models for transport through vegetated regions could be used to model contaminants, nutrients, fish eggs, and several other things of environmental, ecological, and industrial importance. Besides vegetated coastal regions, the numerical modeling of flow and transport through obstructed flows may be applicable to several other engineering concerns including flow and transport through urban environments, forests, fields of crops, biofilm reactors, and porous media.

Bibliography

[1] S. Al-Sadder and R.A.O. Al-Rawi. Finite difference scheme for large-deflection analysis of non-prismatic cantilever beams subjected to different types of continuous and discontinuous loadings. *Archive of Applied Mechanics*, 75(8):459–473, 2006.

[2] M. Balhoff, A. Mikelić, and M.F. Wheeler. Polynomial filtration laws for low reynolds number flows through porous media. *Transport in Porous Media*, 81(1):35–60, 2010.

[3] M. Balhoff and M. Wheeler. A predictive pore-scale model for non-darcy flow in porous media. *SPE Journal*, 14(4):579–587, 2009.

[4] M. J. Batist, V. Babovic, J. Rodríguez Uthurburu, M. Keijzer, R. E. Uittenbogaard, A. Mynett, and A. Verwey. On inducing equations for vegetation resistance. *Journal of Hydraulic Research*, 45(4):435–450, 2007.

[5] J. Bear. *Dynamics of fluids in porous media*. Dover Publications, 1988.

[6] K.E. Bisshopp and D.C. Drucker. Large deflection of cantilever beams. *Appl. Math*, 3, 1945.

[7] R.D. Blevins. Flow-induced vibration. 1990.

[8] A. Bokaian and F. Geoola. Wake-induced galloping of two interfering circular cylinders. *Journal of Fluid Mechanics*, 146(1):383–415, 1984.

[9] A.S. Borgesa, J.M. Vedovotob, F.P. Marianob, and A. da Silveira. Fluid-structure interaction of cylinders by combining the cosserat beams theory and immersed boundary methodology. *Mecánica Computacional*, XXIX(32):3237–3255, 2010.

[10] C.L. Bretschneider and R.O. Reid. Modification of wave height due to bottom friction, percolation, and refraction. Technical report, DTIC Document, 1954.

[11] R. Burke and K. Stolzenbach. Free surface flows through salt marsh grass. *Massachusetts Institute of Technology, Sea Grant College Program. Publication No. MITSG*, pages 83–16, 1983.

[12] K. Chaudhary, M.B. Cardenas, W. Deng, and P.C. Bennett. The role of eddies inside pores in the transition from darcy to forchheimer flows. *Geophysical Research Letters*, 38(24):L24405, 2011.

[13] B.A. Christensen. Open channel and sheet flow over flexible roughness. In *21 st IAHR Congress, Melbourne, Australia*, pages 19–23, 1985.

[14] O. Coulaud, P. Morel, and J.P. Caltagirone. Numerical modelling of nonlinear effects in laminar flow through a porous medium. *Journal of Fluid Mechanics*, 190:393–407, 1988.

[15] J. Cui and V.S. Neary. Large eddy simulation (LES) of fully developed flow through vegetation. In *Hydroinformatics 2002: Proceedings of the 5th International Conference on Hydroinformatics*, 2002.

[16] M. Dado and S. Al-Sadder. A new technique for large deflection analysis of non-prismatic cantilever beams. *Mechanics Research Communications*, 32(6):692–703, 2005.

[17] R.A. Dalrymple, J.T. Kirby, and P.A. Hwang. Wave diffraction due to areas of energy dissipation. *Journal of waterway, port, coastal, and ocean engineering*, 110(1):67–79, 1984.

[18] S.E. Darby. Effect of riparian vegetation on flow resistance and flood potential. *Journal of Hydraulic Engineering*, 125(5):443–454, 1999.

[19] F.H. Dawson and F.G. Charlton. Bibliography on the hydraulic resistance or roughness of vegetated watercourses. *Freshwater Biological Association, Occasional Publication*, 25:1944–1948, 1988.

[20] R.G. Dean and R.A. Dalrymple. Water wave mechanics for engineers and scientists. 1991.

[21] A. Defina and A.C. Bixio. Mean flow and turbulence in vegetated open channel flow. *Water Resources Research*, 41(7):W07006, 2005.

[22] G. Den Hartog and R.H. Shaw. A field study of atmospheric exchange processes within a vegetative canopy. *Heat and Mass Transfer in the Biosphere, Scripta Books, Washington, DC*, pages 299–309, 1975.

[23] C.J. Dunn, F. López, and M.H. García. *Mean flow and turbulence in a laboratory channel with simulated vegetation.* Hydrosystems Laboratory, Department of Civil Engineering, University of Illinois at Urbana-Champaign, 1996.

[24] M.J. Dwyer, E.G. Patton, and R.H. Shaw. Turbulent kinetic energy budgets from a large-eddy simulation of airflow above and within a forest canopy. *Boundary-Layer Meteorology*, 84(1):23–43, 1997.

[25] K.S. Erduran and V. Kutija. Quasi-three-dimensional numerical model for flow through flexible, rigid, submerged and non-submerged vegetation. *Journal of Hydroinformatics*, 5(3):189–202, 2003.

[26] P. Forchheimer. Wasserbewegung durch boden. *Z. Ver. Deutsch. Ing*, 45:1782–1788, 1901.

[27] I. Fried. Stability and equilibrium of the straight and curved elastica-finite element computation. *Computer Methods in Applied Mechanics and Engineering*, 28:49–61, 1981.

[28] K. Furukawa, E. Wolanski, and H. Mueller. Currents and sediment transport in mangrove forests. *Estuarine, Coastal and Shelf Science*, 44(3):301–310, 1997.

[29] M.C. Gambi, A.R.M. Nowell, and P.A. Jumars. Flume observations on flow dynamics in zostera marina(eelgrass) beds. *Marine ecology progress series. Oldendorf*, 61(1):159–169, 1990.

[30] C.R. Garibotti and M. Peszyńska. Upscaling Non-Darcy Flow. *Transport in Porous Media*, 80(3):401–430, 2009.

[31] M. Germano, U. Piomelli, P. Moin, and W.H. Cabot. A dynamic subgrid-scale eddy viscosity model. *Physics of Fluids A: Fluid Dynamics*, 3:1760, 1991.

[32] M.R. Gourlay. Flow retardance in vegetated channels. *Journal of the Irrigation and Drainage Division, ASCE*, 96:351–357, 1970.

[33] W.H. Graf and S.C. Ko. Tests on cylinders in turbulent flow. *Journal of the Hydraulics Division*, 97(8):1265–1267, 1971.

[34] B.E. Griffith and X. Luo. Immersed boundary method with finite element elasticity. *Submitted, preprint available*, 2011.

[35] K. Hessini, J.P. Martínez, M. Gandour, A. Albouchi, A. Soltani, and C. Abdelly. Effect of water stress on growth, osmotic adjustment, cell wall elasticity and water-use efficiency in¡ i¿ spartina alterniflora¡/i¿. *Environmental and Experimental Botany*, 67(2):312–319, 2009.

[36] S.F. Hoerner. *Fluid-dynamic drag: practical information on aerodynamic drag and hydrodynamic resistance.* Hoerner Fluid Dynamics, 1965.

[37] U. Hornung. Introduction. In *Homogenization and porous media*, volume 6 of *Interdiscip. Appl. Math.*, pages 1–25, 259–275. Springer, New York, 1997.

[38] W. Huai, J. Han, Y. Zeng, X. An, and Z. Qian. Velocity distribution of flow with submerged flexible vegetations based on mixing-length approach. *Applied Mathematics and Mechanics*, 30(3):343–351, 2009.

[39] T.J.R. Hughes. Multiscale phenomena: Green's functions, the Dirichlet-to-Neumann formulation, subgrid scale models, bubbles and the origins of stabilized methods. *Computer methods in applied mechanics and engineering*, 127(1):387–401, 1995.

[40] S. Ikeda, T. Yamada, and Y. Toda. Numerical study on turbulent flow and honami in and above flexible plant canopy. *International journal of heat and fluid flow*, 22(3):252–258, 2001.

[41] J. Järvelä. Effect of submerged flexible vegetation on flow structure and resistance. *Journal of hydrology*, 307(1):233–241, 2005.

[42] R. Juanes and T.W. Patzek. Multiscale-stabilized solutions to one-dimensional systems of conservation laws. *Computer methods in Applied Mechanics and engineering*, 194(25):2781–2805, 2005.

[43] R.H. Kadlec. Overland flow in wetlands: vegetation resistance. *Journal of Hydraulic Engineering*, 116:691, 1990.

[44] M. Kanda and M. Hino. Organized structures in developing turbulent flow within and above a plant canopy, using a large eddy simulation. *Boundary-Layer Meteorology*, 68(3):237–257, 1994.

[45] W.M. Kays and A.L. London. *Compact heat exchangers: a summary of basic heat transfer and flow friction design data*. National Press, 1955.

[46] C.E. Kees, I. Akkerman, M.W. Farthing, and Y. Bazilevs. A conservative level set method suitable for variable-order approximations and unstructured meshes. *Journal of Computational Physics*, 230(12):4536–4558, 2011.

[47] C.E. Kees, M.W. Farthing, and M.T. Fong. Locally conservative, stabilized finite element methods for a class of variable coefficient Navier-Stokes equations. Technical Report TR-09-12, U.S. Army Engineer Research and Development Center, Coastal and Hydraulics Laboratory, 2009.

[48] G.J. Klaassen and J.J. Van der Zwaard. Roughness coefficients of vegetated flood plains. *Journal of Hydraulic Research*, 12(1):43–63, 1974.

[49] N. Kobayashi, A.W. Raichle, and T. Asano. Wave attenuation by vegetation. *Journal of waterway, port, coastal, and ocean engineering*, 119(1):30–48, 1993.

[50] D.L. Koch and A.J.C. Ladd. Moderate Reynolds number flows through periodic and random arrays of aligned cylinders. *Journal of Fluid Mechanics*, 349:31–66, 1997.

[51] N. Kouwen and T.E. Unny. Flexible roughness in open channels. *Journal of the Hydraulics Division*, 99(5):713–728, 1973.

[52] E. Kubrak, J. Kubrak, and P.M. Rowiński. Influence of a method of evaluation of the curvature of flexible vegetation elements on vertical distributions of flow velocities. *Acta Geophysica*, pages 1–22, 2011.

[53] V. Kutija and H. Thi Minh Hong. A numerical model for assessing the additional resistance to flow introduced by flexible vegetation. *Journal of Hydraulic Research*, 34(1):99–114, 1996.

[54] C.W. Li and J.F. Xie. Numerical modeling of free surface flow over submerged and highly flexible vegetation. *Advances in Water Resources*, 34(4):468–477, 2011.

[55] C.W. Li and C. Zeng. 3D Numerical modelling of flow divisions at open channel junctions with or without vegetation. *Advances in Water Resources*, 32(1):49–60, 2009.

[56] R. Li and H.W. Shen. Effect of tall vegetations on flow and sediment. *Journal of the Hydraulics Division*, 99(5):793–814, 1973.

[57] A.F. Lightbody and H.M. Nepf. Prediction of velocity profiles and longitudinal dispersion in emergent salt marsh vegetation. *Limnology and Oceanography*, 51(1):218–228, 2006.

[58] J.L. Lions. *Some methods in the mathematical analysis of systems and their control*. Routledge, 1981.

[59] D. Liu, P. Diplas, J.D. Fairbanks, and C.C. Hodges. An experimental study of flow through rigid vegetation. *Journal of Geophysical Research*, 113(F4):F04015, 2008.

[60] F. López and M. Garcia. Open-channel flow through simulated vegetation: Turbulence modeling and sediment transport. Technical Report WPR-CP 10, US Army Engineer Waterways Experiment Station, August 1997.

[61] F. López and M.H. García. Mean flow and turbulence structure of open-channel flow through non-emergent vegetation. *Journal of Hydraulic Engineering*, 127:392, 2001.

[62] A.E.H. Love. *A treatise on the mathematical theory of elasticity*. at the University Press, 1920.

[63] R.A. Luettich Jr, J.J. Westerink, and N.W. Scheffner. ADCIRC: An advanced three-dimensional circulation model for shelves, coasts, and estuaries. report 1. theory and methodology of adcirc-2ddi and adcirc-3dl. Technical report, DTIC Document, 1992.

[64] S.C. Luo, T.L. Gan, and Y.T. Chew. Uniform flow past one (or two in tandem) finite length circular cylinder (s). *Journal of wind engineering and industrial aerodynamics*, 59(1):69–93, 1996.

[65] S.A. Mattis, C.N. Dawson, C.E. Kees, and M.W. Farthing. Numerical modeling of drag for flow through vegetated domains and porous

structures. *Advances in Water Resources*, 39:44–59, April 2012.

[66] Y. Mazda, N. Kanazawa, and E. dan Wolanski. Tidal asymmetry in mangrove creeks. *Hydrobiologia*, 295:51–58, 1995.

[67] C.C. Mei and J.L. Auriault. The effect of weak inertia on flow through a porous medium. *Journal of Fluid Mechanics*, 222:647–663, 1991.

[68] F.J. Mendez and I.J Losada. An empirical model to estimate the propagation of random breaking and nonbreaking waves over vegetation fields. *Coastal Engineering*, 51(2):103–118, 2004.

[69] C. Meneveau and T.S. Lund. The dynamic Smagorinsky model and scale-dependent coefficients in the viscous range of turbulence. *Physics of Fluids*, 9:3932, 1997.

[70] A. Mikelić. Homogenization theory and applications to filtration through porous media. *Filtration in porous media and industrial application*, pages 127–214, 2000.

[71] C.H. Moeng. A large-eddy-simulation model for the study of planetary boundary-layer turbulence. *Journal of the Atmospheric Sciences*, 41(13):2052–2062, 1984.

[72] H. Nepf and M. Ghisalberti. Flow and transport in channels with submerged vegetation. *Acta Geophysica*, 56(3):753–777, 2008.

[73] H.M. Nepf. Drag, turbulence, and diffusion in flow through emergent vegetation. *Water Resources Research*, 35(2):479–489, 1999.

[74] H.M. Nepf, J.A. Sullivan, and R.A. Zavistoski. A model for diffusion within emergent vegetation. *Limnology and Oceanography*, 42:1735–1745, 1997.

[75] H.M. Nepf and E.R. Vivoni. Flow structure in depth-limited, vegetated flow. *Journal of Geophysical Research*, 105(C12):28547–28557, 2000.

[76] G.P. Palau, T. Stoesser, A. Rummel, and W. Rodi. Turbulent shallow flow through emergent vegetation. In *ICEH: International Conference on Eco-hydraulics. Tempe, Arizona*, 2007.

[77] C.S. Peskin. The immersed boundary method. *Acta numerica*, 11(1):479–517, 2002.

[78] M. Peszyńska, A. Trykozko, and K. Augustson. Computational Upscaling of Inertia Effects from Porescale to Mesoscale. *Computational Science–ICCS 2009*, pages 695–704, 2009.

[79] S. Petryk and G. Bosmajian. Analysis of flow through vegetation. *Journal of the Hydraulics Division*, 101(7):871–884, 1975.

[80] S.B. Pope. *Turbulent flows*. Cambridge Univ Pr, 2000.

[81] J.A. Putnam and J.W. Johson. The dissipation of wave energy by bottom friction. *Transactions, American Geophysical Union*, 30:67–74, 1949.

[82] D. Raboud, M.G. Faulkner, and A.W. Lipsett. A segmental approach for large three-dimensional rod deformations. *International journal of solids and structures*, 33(8):1137–1156, 1996.

[83] M. Rasoloarijaona and J.L. Auriault. Nonlinear seepage flow through a rigid porous medium. *European Journal of Mechanics. B, Fluids*, 13(2):177–195, 1994.

[84] M.R. Raupach. Drag and drag partition on rough surfaces. *Boundary-layer meteorology*, 60(4):375–395, 1992.

[85] M.R. Raupach, P.A. Coppin, and B.J. Legg. Experiments on scalar dispersion within a model plant canopy part I: The turbulence structure. *Boundary-Layer Meteorology*, 35(1):21–52, 1986.

[86] M.R. Raupach and R.H. Shaw. Averaging procedures for flow within vegetation canopies. *Boundary-Layer Meteorology*, 22(1):79–90, 1982.

[87] W.O. Ree and V.J. Palmer. *Flow of water in channels protected by vegetative linings*. US Dept. of Agriculture, 1949.

[88] R.O. Reid and R.E. Whitaker. Wind-driven flow of water influenced by a canopy. *Journal of the Waterways Harbors and Coastal Engineering Division*, 102(1):61–77, 1976.

[89] S. Rojas and J. Koplik. Nonlinear flow in porous media. *Physical Review E*, 58(4):4776–4782, 1998.

[90] H. Rouse. *Fluid Mechanics for Hydrualic Engineers.* McGraw-Hill Book Company, Inc., 1938.

[91] E. Sanchez-Palencia. Non-homogeneous media and vibration theory. In *Non-Homogeneous Media and Vibration Theory*, volume 127, 1980.

[92] C. Saowapon and N. Kouwen. Physically based model for determining flow resistance and velocity profiles in vegetated channels. 1989.

[93] A.E. Scheidegger. The physics of flow through porous media. *Soil Science*, 86(6):355, 1958.

[94] I. Seginer, P.J. Mulhearn, E.F. Bradley, and J.J. Finnigan. Turbulent flow in a model plant canopy. *Boundary-Layer Meteorology*, 10(4):423–453, 1976.

[95] R.H. Shaw and U. Schumann. Large-eddy simulation of turbulent flow above and within a forest. *Boundary-Layer Meteorology*, 61(1):47–64, 1992.

[96] J.F.A. Sleath. Sea bed mechanics. 1984.

[97] D.J. Steigmann and M.G. Faulkner. Variational theory for spatial rods. *Journal of elasticity*, 33(1):1–26, 1993.

[98] T. Stoesser, C. Liang, W. Rodi, and G.H. Jirka. Large eddy simulation of fully-developed turbulent flow through submerged vegetation.

In *International Conference on Fluvial Hydraulics, SEP06-08. Lisbon, Portugal*, volume 1, pages 227–234, 2006.

[99] T. Stoesser, G.P. Salvador, W. Rodi, and P. Diplas. Large eddy simulation of turbulent flow through submerged vegetation. *Transport in porous media*, 78(3):347–365, 2009.

[100] B.M. Stone and H.T. Shen. Hydraulic resistance of flow in channels with cylindrical roughness. *Journal of Hydraulic Engineering*, 128(5):500–506, 2002.

[101] H. Tennekes and J.L. Lumley. *A first course in turbulence*. The MIT press, 1972.

[102] S. Timoshenko. *Strength of Materials: Advanced theory and problems*. D. Van Nostrand Company, 1956.

[103] L.N. Trefethen and D. Bau III. *Numerical linear algebra*. Number 50. SIAM, 1997.

[104] T. Tsujimoto, Y. Shimizu, T. Kitamura, and T. Okada. Turbulent open-channel flow over bed covered by rigid vegetation. *Journal of Hydroscience and Hydraulic Engineering*, 10(2):13–25, 1992.

[105] A.K. Turner and N. Chanmeesri. Shallow flow of water through non-submerged vegetation. *Agricultural Water Management*, 8(4):375–385, 1984.

[106] D. Velasco, A. Bateman, and V. Medina. A new integrated, hydro-mechanical model applied to flexible vegetation in riverbeds. *Journal of Hydraulic Research*, 46(5):579–597, 2008.

[107] P.R. Voke. Subgrid-scale modelling at low mesh reynolds number. *Theoretical and computational fluid dynamics*, 8(2):131–143, 1996.

[108] T.V. Wamsley, M.A. Cialone, J.M. Smith, J.H. Atkinson, and J.D. Rosati. The potential of wetlands in reducing storm surge. *Ocean Engineering*, 37(1):59–68, 2010.

[109] J.J. Westerink, R.A. Luettich, J.C. Feyen, J.H. Atkinson, C. Dawson, H.J. Roberts, M.D. Powell, J.P. Dunion, E.J. Kubatko, and H. Pourtaheri. A basin-to channel-scale unstructured grid hurricane storm surge model applied to southern louisiana. *Monthly Weather Review*, 136(3):833–864, 2008.

[110] C. Wilson, T. Stoesser, P.D. Bates, and A.B. Pinzen. Open channel flow through different forms of submerged flexible vegetation. *Journal of Hydraulic Engineering*, 129:847, 2003.

[111] N.R. Wilson and R.H. Shaw. A higher order closure model for canopy flow. *Journal of Applied Meteorology*, 16:1197–1205, 1977.

[112] J.C. Wodie and T. Levy. Correction non linéaire de la loi de darcy. *Comptes rendus de l'Académie des sciences. Série 2, Mécanique, Physique,*

Chimie, Sciences de l'univers, Sciences de la Terre, 312(3):157–161, 1991.

[113] E. Wolanski, M. Jones, and J.S. Bunt. Hydrodynamics of a tidal creek-mangrove swamp system. *Marine and Freshwater Research*, 31(4):431–450, 1980.

[114] W. Wu. *Computational river dynamics*. CRC Press, 2007.

[115] W. Wu, Y. Ozeren, D. Wren, Q. Chen, G. Zhang, M. Holland, Y. Ding, S.N. Kuiry, M. Zhang, Jadhav R., et al. Investigation of surge and wave reduction by vegetation. *Phase I Report for SERRI Project No. 80037*, page 315, 2011.

[116] M.M. Zdravkovich. Review of flow interference between two circular cylinders in various arrangements. *ASME Transactions Journal of Fluids Engineering*, 99:618–633, 1977.

[117] M.M. Zdravkovich. Interstitial flow field and fluid forces. *Technology for the 90s. ASME*, pages 595–658, 1993.

[118] M.M. Zdravkovich and D.L. Pridden. Interference between two circular cylinders; series of unexpected discontinuities. *Journal of Wind Engineering and Industrial Aerodynamics*, 2(3):255–270, 1977.

[119] A. Zukausras. Heat transfer from tubes in crossfiow. *Advances in heat transfer*, 8:93, 1973.